UNIVERSITÉ DE STRASBOURG

ÉCOLE DOCTORALE ED-182

Institut de Physique et Chimie des Matériaux de Strasbourg

THÈSE présentée par:

Rubén Soria Martínez

soutenue le : **30 septembre 2020**

pour obtenir le grade de: **Docteur de l'université de Strasbourg**

Discipline/ Spécialité: Physique de la matière condensée

Modeling of local excitation processes in molecular nanojunctions

THÈSE dirigée par :
M. BULOU Hervé Charge de recherche, IPCMS /CNRS/Université de Strasbourg

RAPPORTEURS :
Mme. GAUDRY Emilie Professeur, Institut Jean Lamour/CNRS/Université de Nancy
M. JOLY Yves Directeur de recherche, Institut Néel/CNRS/Université de Grenoble

---

AUTRES MEMBRES DU JURY :
Mme. POLONI Roberta Chargée de recherche, SIMaP/CNRS/Université de Grenoble
M. HERVIEUX Paul-Antoine Professeur, IPCMS/CNRS/Université de Strasbourg

"*El recuerdo que deja un libro*
es más importante que el libro mismo."
Gustavo Adolfo Bécquer

Acknowledgements

First, I would like to thank my advisor Hervé for giving me the opportunity to work in this project. Second, I would like to thank the member of the scanning tunneling microscopy, specially to Benjamin Doppagne for the discussions between experiment and theory. Also, for the eternal discussions about the best *cuisine* between the French and Spanish food. I am very thankful as well to Guillaume Schull, it always is a pleasure have a science (and not science) discussion with him. I also thank to Jayash Panigrahi from DON group for the work live and also for the talks trying to fix the world, and of course, always smoking a cigarette. Many thanks to the people of the nanomaterials group, Nathaly, Yuvna and Othmane but I have to thank specially to Walid. It was a pleasure to share the office all this time with you. Many thanks to encourage me in the last period of my PhD when I was very stressed. Last but not least to my friends in Spain, Adrian, Laura, Dani, Maria y Jose Luis. And of course to my all my family. I have to use a Feynman's quote to describe my parents support, *Although my mother didn't know anything about science, she had a great influence on me as well. In particular, she had a wonderful sense of humor, and I learned from her that the highest form of understanding we can achieve are laughter and human compassion.* To my brother Ivan, my sister in law Mirari and my godson Iker. You are 3 months old and I cannot see the moment to hug you. Mariana you know that I am a few words man when I write and I prefer to express myself with a talk... Pero sabes que mi vida esta llena de casualidades y tú eres la mejor de todas. Muito obrigado cariño por darme lo más valioso que un hombre puede recibir en esta vida. Y, por supuesto, a tí Iago, mi pequeño diamante. Llegaste sín previo aviso y trastocando las vidas de tus padres. Me has hecho luchar contra mis miedos, pero como me dijo siempre tu abuela, ya sabrás lo que duelen los hijos. ¡¡Quién me iba a decir a mí que cruzaría el charco en un pájaro de hierro!!

Contents

List of Figures

List of abbreviations

STM Scanning tunnel microscopy. 1
DFT Density functional theory. 7
KS Kohn-Sham .8
LDA Local Density approximation. 9
GGA Generalized Gradient approximation. 10
meta-GGA meta- Generalized Gradient approximation. 10
TDDFT Time Dependent Density Functional Theory (TD-DFT). 11
(LR)-TDDFT Linear response time dependent density functional theory. 16
(RT)-TDDFT Real time time dependent density functional theory. 18
H_2Pc Free-based phthalocyanine. 30
ZnPc Zinc metallo-phthalocyanine. 31
PdPc Palladium metallo-phthalocyanine. 32
STM-F STM-induced fluorescence. 41

Resumé

Le travail de thèse présenté dans ce manuscrit s'inscrit dans le cadre général des travaux visant à décrire et à modeliser les phénomènes impliqués dans les microscopies à sonde locale, et plus spécifiquement la microscopie à effet tunnel. L'effet tunnel est un phénomène quantique connu depuis la fin des années 1920 [1–8]. Plusieurs étapes marquantes jalonnent le développement des techniques de microscopie reposant sur cet effet. Au début des années 80, ce fût l'exploitation de l'effet tunnel pour cartographier le courant passant entre une surface et la pointe d'un microscope afin de caractériser structuralement la surface des matériaux à l'échelle du nanomètre [9]. Puis fin des années 80/début des années 90, ce fût la manipulation d'atomes et de molécules au moyen de la pointe du microscope[10–14].

Enfin, une étape importante fût franchie fin des années 90, lorsque les premières expériences utilisant le microscope à effet tunnel (STM) pour mesurer les propriétés de transport électronique à travers des nanojonctions moléculaires furent publiées[15, 16]. Cette étape est considérée par certains scientifiques comme le point de départ de la nanoélectroniques moléculaire. De nombreux progrès ont été réalisés depuis cette période, et à l'heure actuelle, le degré de maîtrise est tel qu'il est possible non seulement d'assembler des atomes[17, 18] de mesurer les propiétés électriques et magnétiques de ces assemblages à l'echelle nanométrique[19–23], d'en manipuler les propriétés de transport électronique [24, 25] mais également d'exciter ces dispositifs afin de les faire transiter d'un état vers un autre, ouvrant la voie au développement de nouvelles méthodes de spectroscopie optique ayant une résolution spatiale sub-nanométrique[26–40].

L'observation des spectres d'émission de lumière par des nanostructures moléculaires excitées au moyen de la pointe d'un microsope à effet tunnel indique qu'outre les transitions habituelles observées avec des sources d'excitation non locales telles que des lasers par exemple, on observe des pics supplémentaires dont l'origine est encore aujourd'hui debattue. Enfin, récemment, l'équipe de G.Schull à l'IPCMS a démontré expérimentalement que le spectre de la lumière émise par la molécule lors de sa désexcitaion variait selon la position de la pointe au dessus de la molécule, laissant en-

trevoir la possibilité de cartographier les molécules dans leurs états excités avec une résolution subnanometrique[41].

Cette thèse vise à développer un modèle rendant compte des principales caractéristiques de l'émission de lumière par des nanojonctions moléculaires excitées par un courant tunnel. Il s'agissait dans un premier temps d'identifier les principaux phénomènes impliqués dans l'émission de lumière er d'en quantifier l'importance. Puis dans un second temps il s'agissait d'étudier l'impact de la nature locale de l'excitation de la molécule par le courant tunnel circulant entre la pointe du microscope et le substrat supportant les molécules.

Description de la démarche suivie.

Pour réaliser ces travaux, une démarche reposant sur la confrontation directe des résultats de simulations numériques aux mesures expérimentales est développé, mesures expérimentales réalisées pour certaines au sein de l'IPCMS par l'equipe de G. Schull[42]. L'intérêt de cette démarche réside dans le fait que les simulations numériques offrent un contrôle total a la fois sur le positionnement des atomes dans le nanojonctions moléculaires et sur les phénomènes physiques impliqués dans l'évolution des système via le paramétrage des hamiltoniens utilisés dans les modèles. L'analyse comparative des résultats des simulation numériques aux résultats expérimentaux (spectre, cartographie) apparaît ainsi comme un outil efficace pour identifier les phénomènes physiques impliqués. La nécessité de la comparaison à l'expérience impose toutefois des contraintes importantes.

Tout d'abord, bien que les nanojonctions moléculaires soient des systèmes de taille nanométrique, le nombre d'atomes à prendre en considération pour décrire le plus fidèlement possible la physique des systèmes considérés expérimentalement est de l'ordre de quelques centaines à un millier d'atomes (molécule, pointe et substrat). Devoir considérer un grand nombre d'atomes en physique numérique n'est pas un problème en soit. Toutefois, en raison de la nature des phénomènes impliqués (effet tunnel entre la pointe et le substrat, excitation de la molécule), il est nécessaire d'avoir recours à des méthodes de la physique quantique, coûteuses en terme de mémoire et de temps de calcul lorsqu'il s'agit de réaliser des simulations numériques. En effet, l'émission de la lumière par un matériau résulte d'une réorganisation de la distribution des électrons dans le matériau permettant d'en abaisser son énergie.

Aussi une part importante du travail présenté dans ce document a consisté à determiner les distributions électroniques dans le nanojonctions moléculaires

dans leur état fondamental et dans certains de leurs états excités, les spectres d'emission étant ensuite calculés à partir des probabilités de transitions entre ces différentes distributions électroniques.

Aussi, je me suis placé dans le cadre de la théorie de la fonctionelle de densité (DFT) pour réaliser ces travaux. La DFT est probablement la méthode la plus efficace à l'heure actuelle pour calculer la distribution des électrons dans systènes proches de ceux considérés expérimentalement. En effet les avancées technologiques en électronique et en microélectronique ces dernières années permettent aujourd'hui de disposer d'ordinateurs ayant de grandes quantités de mémoires vives. On peut ainsi manipuler des matrices de très grande taille, et ainsi considérer des systèmes composés d'un grand nombre d'électrons dans les simulations. Conjointement à ces évolutions techniques, des progrès importants ont été réalisés dans le domaine des méthodes numériques. Le concept de pseudopotentiel[43–47] en réduisant le nombre d'électrons à prendre en compte dans le calculs, les techniques de développement multipolaires en permettant d'accélérer les calculs des intégrales multiples[48–50], ou bien des méthodes itératives de diagonalisation de matrices[51–55] ont également contribué à étendre la taille des systèmes étudiés.

Toutes ces avancées permettent dorénavant la confrontation directe des dispositifs étudiés expérimentalement aux modélisations théoriques. Il s'agit d'un atout considérable pour l'étude des nano-dispositifs, l'accès direct à des informations telles que la répartition des niveaux d'énergie ou la distribution des électrons, également accessibles expérimentalement, fournissant des éléments clefs à la compréhension de la physique régissant le comportement de ces objets. L'excitation des molécules a été traitée dans le cadre de la DFT dépendante du temps (TD-DFT)[56–58]. Le principe est de suivre l'évolution de la distribution de charge dans la nanojonction moléculaire suite à la perturbation due à l'excitation.

J'ai utilisé deux approches afin de réaliser ces simulations selon la nature de l'information recherchée. La première consiste à traiter l'excitation dans le cadre de la théorie des perturbations dépendantes du temps. Il s'agit donc des cas où l'excitation est faible. Dans cette approche, la réponse linéaire du système réel, $\delta\rho(r,\omega)$, à un potentiel perturbatif (tel qu'un champ électrique oscillant), peut être calculée comme la réponse d'un système sans interaction à un potentiel effectif, $\delta V^{eff}(r,\omega)$, dépendant de la perturbation[59]:

$$\delta\rho(r,\omega) = \int dr' \chi_{KS}(r,r';\omega)\delta V^{eff}(r,\omega)$$

.

La fonction de réponse $\chi_{KS}(r,r';\omega)$ peut être calculée à partir des orbitales de Kohn-Sham occupées et virtuelles prises dans l'état fondamental du système[60] et calculées au préalable pour le système pris dans son état fondamental :

$$\chi_{KS}(r,r';\omega) = \sum_{n,m}(f_m - f_n)\frac{\psi_n^*(r)\psi_m(r)\psi_m^*(r')\psi_n(r')}{(\epsilon_m - \epsilon_n) - \omega + i\nu}$$

,

où f_i est le nombre d'occupation de l'orbitale de Kohn-Sham i. Du point de vue numérique, j'ai utilisé la formulation de Casida[161] afin de ramener le problème à la résolution d'un système aux valeurs propres. N'étant intéressé que par les transitions de plus basses énergies, seuls les états de Kohn-Sham aux alentours du niveau de Fermi contribuent de manière significative aux changements de distribution électroniques induits par la perturbation. J'ai ainsi déterminé qu'en général, une centaine d'états de Kohn-Sham occupés et virtuels suffisent pour décrire le système dans son état excité.

Toutefois la suceptibilité étant donnée par la somme de produit d'orbitales de Kohn-Sham qui elles-mêmes sont des combinaisons linéaires de fonctions de bases, les matrices à diagonaliser sont de très grande taille ce qui nécessite d'avoir beaucoup de mémoire à disposition. A titre d'illustration, le calcul des propriétés optiques dans le cadre de la réponse linéaire nécessite 114 Go de mémoire pour une molécule de terthiophène (23 atomes) et 670 Go pour une molécule d'oligothiophene (86 atomes). Aussi tous les résultats présentés dans cette étude ont été obtenus grâce aux centres de calcul nationaux (IDRIS, CINES). Nous avons utilisé l'algorithme itératif de Davidson-Liu[50] pour procéder à la diagonalisation de la matrice de Casida. D'un point de vue numérique, un aspect intéressant de la réponse linéaire est qu'elle est rapide aussi c'est cette méthode que j'ai utilisée pour déterminer les énergies des pics d'absorption de lumière. Par ailleurs, étant une méthode perturbative, elle permet d'avoir accès assez facilement à la composition des transitions optiques en fonction des états de Kohn-Sham des molécules dans leur état fondamental ce qui facilite grandement l'interprétation physique des résultats. En revanche la réponse linéaire ne permet pas d'avoir accès à l'évolution temporelle de la perturbation à travers la molécule. Il s'agit d'un aspect important du travail de thèse car il est raisonnable de penser

que si le localisation de l'excitation locale a un impact important sur la probabilité d'excitation de la molécule, il en est de même sur la manière dont cette excitation locale va ensuite se propager à l'ensemble de la molécule. Aussi, pour étudier la propagation de l'excitation locale de la perturbation à travers la molécule, nous avons eu recours à une seconde approche de la TD-DFT, dite "en temps réel", qui repose sur la résolution des équations de Kohn-Sham dépendantes du temps[61]:

$$\left(-\frac{1}{2}\nabla^2 + V_{KS}(r) + V_{ext}(r,t)\right)\psi(r,t) = i\frac{\partial}{\partial t}\psi_{KS}(r,t)$$

.

Le principe est de propager au cours du temps les orbitales de Kohn-Sham d'un système, initialement dans son état fondamental, soumis à une perturbation V_{ext}(r, t), telle que par exemple un champ électrique oscillant. Les propriétés optiques sont déterminées partir de la transformée de Fourier du moment dipolaire induit par la perturbation. La résolution des énergies de transition déterminées selon cette méthode est d'autant plus fine que l'intervalle de temps simulé est grand. Il s'agit d'un point important à avoir à l'esprit. En effet, un fort couplage vibronique fait partie des hypothèses envisagées pour expliquer la présence de pics supplémentaires dans les spectres d'emission de lumière par des molécules excitées au moyen de la pointe d'un microscope à effet tunnel.

Les niveaux vibrationnels dans les molécules que j'ai considéréesnous étant espacés d'une cinquantaine de meV, j'ai établi qu'une résolution en énergie des spectres optiques meilleure que 5 meV, soit un intervalle de simulation supérieur à 50 fs, est nécessaire afin d'avoir des données suffisamment précises pour être confrontées aux mesures expérimentales. Jai déterminé que le pas typique d'intégration temporelle doit être de l'ordre de l'attosecondes, soit 50 000 pas d'intégration pour un intervalle de 50 fs. Un pas d'intégration nécessitant environ 10 s de temps machine pour un système d'une centaine d'atomes, de très longs intervalles de simulation, d'environ 150 heures/coeur, ont été nécessaires pour réaliser ce type de calculs.

Organisation du manuscrit

Le manuscrit est organisé en cinq chapîtres. Le premier est consacré à la présentation du contexte scientifique dans lequel se situe le travail. Le deuxième chapître est consacré à la présentation des théories, des méthodes

numériques et des codes utilisés pour réaliser ce travail. Les trois derniers chapîtres présentent les résultats obtenus. Chacun de ces trois chapîtres est dédié à examiner une hypothèse spécifique à l'origine des pics supplémentaires dans les spectres d'électroluminescence des nanostructures moléculaires excitées par le courant tunnel :

- L'effet de contrainte dans la molécule dans le troisième chapître,
- L'effect de la nature locale de l'excitation dans the quatrième chapître,
- La nature électronique de la source d'excitation locale dans le cinquième chapître.

Le chapître III débute par une présentation de résultats concernant des molécules à base de phthalocyanine, H_2Pc, PdPc et ZnPc isolées. Chacune des molécules a été optimisée structuralement par DFT et leurs spectres optiques calculés par TD-DFT en réponse linéaire. Une analyse comparative de la structure des trois molécules est présentée et les liens entre structure et spectre optique sont discutés. L'intérêt de cette partie du travail est de fournir un ensemble de structures et de spectres de référence qui sont utilisés par la suite pour l'analyse des résultats concernant les structures plus complexes modélisant les objets étudiés expérimentalement. La seconde partie du chapître III concerne les molécules adsorbées sur des substrats. Expérimentalement, les mesures sont en générale déposées sur des substrats de NaCl. Ces substrats permettent d'empécher l'exciton créé dans la molécule par l'excitation tunnelle d'être "évacué" via le substrat métallique, et ils favorisent ainsi la fluorescence de la nanojonction moléculaire. Deux types de nanojonctions ont été considérés dans les simulations : Un substrat de 2 monocouches de NaCl et un substrat d'une monocouche de NaCl reposant sur trois monocouches d'or.

Le fait que les molécules considérées reposent à plat sur les substrats implique de devoir considérer des substrats de surface d'au minimum 10 x 10 atomes, ce qui correspond à 200 atomes pour le substrat de NaCl et 400 atomes pour le substrat de NaCl/Au. Il a été choisi de faire des simulations principalement avec le substrat de NaCl, plus petit, et donc moins coûteux en ressources de calcul. Toutefois j'ai décidé de considérer quelques situations avec le substrat NaCl/Au afin d'une part de détecter un potentiel effet de contrainte induit par l'or sur la couche de NaCl sur le spectre optique de la molécule de phthalocyanine et d'autre part de quantifier l'impact de l'interface métal/NaCl sur l'excitation de la molécule.

Je présente également la construction de la couche de NaCl sur l'or dans cette partie du manuscrit. En raison de la nature biatomique du substrat de NaCl et de la symétrie de la molécule, j'ai considéré plusieurs configurations

selon le positionnement du centre de la molécule par rapport au substrat et selon l'angle entre les axes principaux de la molécule et ceux du substrat. Le troisième chapître se poursuit par une présentation des spectres optiques associés à quelques unes de ces configurations. Le chapître se termine par une analyse comparative de ces spectres optiques et une discussion au sujet des liens entre contraintes et déformations dans la molécule et spectres d'émission.

Dans le chapître IV, je considère l'impact de la nature locale de l'excitation. J'ai ainsi réalisé une série de simulations de la propagation d'une excitation à travers la molécule. L'idée est de perturber localement la molécule au moyen d'un champ électrique dont on contrôle la fréquence et l'extension spatiale, puis de suivre l'évolution temporelle de la perturbation dans la molécule. L'intérêt d'utiliser un champ électrique est qu'il est possible de sonder plusieurs directions d'excitation via la polarisation. Le début du quatrième chapître est consacré à la présentation du protocole utilisé ainsi qu'aux résultats obtenus les plus marquants. Chaque molécule a été excitée localement, puis l'évolution temporelle des moments dipolaires de transition a été calculée selon les axes principaux des molécules. Je présente ensuite plusieurs analyses de résultats dont une concernant l'existence de couplages entre les axes principaux de la molécule. Un exemple de ce type de couplage est présenté. La dernière partie du chapître est consacrée au transfert d'énergie entre un système à deux molécules.

Le dernier chapître est le plus exploratoire. Je présente le modèle que j'ai développé afin de rendre compte des phénomènes impliqués lors du passage d'un courant d'électrons tunnels à travers une molécule située entre la pointe du microscope et une surface, et plus spécifiquement les excitations induites dans la molécule par le passage de l'électron tunnel. Afin de modéliser la source d'excitation, j'ai développé, dans le cadre théorique de la fonctionnelle de densité dépendante du temps, une approche non perturbative qui consiste à propager un paquet d'onde électronique, représentant l'électron tunnel, à travers la jonction en résolvant les équations de Kohn-Sham dépendantes du temps en temps reél. Les opérateurs laplacien impliqués dans le système (équations de Kohn-Sham pour les orbitales de Kohn-Sham, équation de Poisson pour le potentiel électrostatique associé à la distribution de charges dans le système) sont approximés dans le cadre de la méthode des différences finies à trois dimensions.

Les résultats présentés dans cette partie du manuscrit ont été obtenus avec un pas de discrétisation spatiale de 0.15Å déduit de l'étude en convergence de l'énergie totale. La résolution de l'équation aux valeurs propres issues des équations de Kohn-Sham a été faite au moyen de l'algorithme de Davidson et la résolution de l'équation de Poisson au moyen de l'algorithme du gradient

conjugué. La fonctionnelle d'échange et corrélation a été décrite dans le cadre de l'approximation de la densité locale, avec la paramétrisation de Perdew et Zunger pour la corrélation[62].

L'évolution temporelle du système a été calculée dans le cadre de la méthode de Crank et Nicolson[63] avec un pas d'intégration temporelle d'une attoseconde. Afin d'empécher toute réflexion de l'électron tunnel à la surface du substrat, un potentiel complexe a été utilisé pour absorber le paquet d'onde une fois le substrat atteint. J'ai considéré une situation de départ construite de telle sorte à ce qu'il n'y ait aucune interaction initiale entre le paquet d'onde représentant l'électron tunnel et la molécule. J'ai ensuite réalisé plusieurs séries de propagations pour différentes vitesses de propagation du paquet d'onde, correspondant à différentes tensions pointe/échantillon. J'ai porté une attention particulière au développement d'un protocol permettant de limiter au maximum la dispersion du paquet d'onde au cours de la propagation. C'est un point délicat sur lequel j'ai passé du temps car à la différence des photons, la relation de dispersion parabolique des électrons tunnels dans la jonction entraine que leurs vitesses de phase et de groupe sont différentes se traduisant par une déformation du paquet d'onde au cours de la propagation.

A l'heure actuelle, j'ai partiellement résolu le problème en introduisant un potentiel harmonique 2D dans le plan du front d'onde électronique de sorte à avoir une dispersion linéaire. J'ai vérifié que l'impact de ce potentiel sur la molécule est négligeable. En revanche, concernant la dispersion longitudinale, je n'ai pas encore trouvé de solution satisfaisante, permettant à la fois de garder un paquet d'onde non déformé et sans impact sur la molécule. La meilleure solution que j'ai trouvée pour l'instant est de considérer un chemin de propagation le plus court possible compatible avec les exigences du système. Les résultats indiquent qu'à mesure que l'électron tunnel se propage dans la jonction, on observe l'apparition progressive d'une interaction entre l'électron tunnel et la molécule se traduisant par une perturbation de la distribution des électrons les plus externes de la molécule. J'ai identifié deux régimes dans le comportements du nuage électronique de la molécule à l'approche du paquet d'onde. Une forte répulsion du nuage électronique aux premiers temps de la propagation que j'attribue à l'interaction Coulombienne "classique" entre la charge de l'électron tunnel et le nuage électronique des électrons de la molécule.

Puis une atténuation de la répulsion que j'attribue à l'interaction d'échange qui apparaît en raison de l'indiscernabilité de l'électron tunnel avec les électrons de la molécule lorsque le paquet d'onde est proche de la molécule. J'ai ensuite étudié le comportement de ces deux régimes en fonction de la

position de la pointe sur la molécule. J'ai identifié plusieurs comportements différents qui semblent être liés à une modification des poids relatifs des interactions d'échange et Coulombienne en fonction de l'environnement locale où le paquet d'onde penètre dans la molécule.

Chapter 1

General introduction.

The project below describes the excitation phenomena observed on scanning tunnel microscopy (STM). The tunnel effect is a quantum phenomena known since late 1920's [1–8]. Several milestones were reached on the development of the microscopy techniques based on this effect. On early 80's the tunnel effect was used to map the current between a surface and the tip of the microscope in order to characterize the material surfaces in nanometre scale[9]. In 1990's the first experiments using the scanning tunnel microscopy were devoted on the study of the electronic transport properties through the molecular nanojunctions [15, 16] and are considered as the starting point of the molecular nanoelectronic. Nowadays, it is possible to assemble atoms and molecules using the tip of the STM[17, 18], measure the electromagnetic properties of this assembles at nanoscale[19–23], the electronic transport properties [24, 25] and the excitation of these devices from one state to another, leading to the development of new optical spectroscopy methods in a sub-nanometric spatial resolution [26–40]. Nevertheless, regarding the optical spectra of molecular nanostructures excited by the tip of the STM, we observe that there are additional transition peaks, whose origin is still debated today due to the action non-local sources of excitation. Recently, G. Schull's team has demonstrated experimentally that the spectrum of the light emitted by the molecule during its excitation varied according to the position of the tip above the molecule, suggesting the possibility of mapping molecules in their excited states with subnanometric resolution[41].

This manuscript is devoted to the development of a model to report the main characteristics of the light emission by molecular nanojunctions excited by a tunnel current. The first step is to identify the main phenomena involved in the light emission and to quantify its importance. Secondly, the study of the impact of the nature of a local excitation by the tunnel current flowing between the tip and the substrate. A comparative analysis between theory and experiment is an effective tool for identify and describe the

physical phenomena involved. However, this comparison with experiments imposes significant constraints. The molecular nanojunctions are described in a nanoscale, the number of atoms to take in consideration to describe as faithfully as possible the physics of the system is in the order of hundred to a thousands atoms (molecule, tip and substrate). The lack of simulations respect to experiments is the computational limitations in terms of resources as computing time or memory needed to perform the simulation.

The emission of light by a molecule is the result of a reorganisation of the electron distribution in it. The determination of the electronic distribution of the ground state and excited state of a system is the fundamental key to understand the excitation (absorption) mechanism. Also, the emission spectra can be calculate from the probabilities of transitions between these different electronic distributions. In terms of methods used to this task, Density functional theory is, probably, the most efficient method to study the electronic structure of a system. The exponential grow in the last 30 decades of this method gives an idea of the popularity and versatility of this technique due to the relatively low computational cost in comparison with traditional methods as Hartree-Fock or Möller-Plesset. However, there is still some limitation of this technique, such as, the description of intermolecular interactions as van der Waals forces (dispersion). The consequence of this limitation is the accuracy of the functional used in this approach and to solve it there is a continuous development of functional trying to include terms on them in order to improve their accuracy. The recent technological advances in electronics allow computers with large amounts of RAM making possible the manipulation of very large matrices, and thus consider systems with a large number of electrons in the simulations.

Time Dependent Density Functional Theory method is commonly used to investigate the properties and dynamics of a system in presence of a time-dependent potential, such as electric or magnetic fields. The principle of this approach is to follow the evolution of the charge distribution and extract features like excitation energies, frequency-dependent response properties and photoabsorption spectra. This method is an extension of the DFT in which the time dependence is included. Moreover, the linear-response theory and the real-time propagation theory are two complementary techniques inside the TD-DFT approach. From the numerical point of view, linear response theory approach reduce the problem to a eigenvalue system. On the other hand, with the linear-response theory is not possible to track the evolution of a perturbation through the molecule. To study the propagation of perturbation the real-time time-dependent theory is a good choice. The basis of this theory is the propagation (in time) of the ground state Kohn-Sham orbitals due to the interaction with a perturbation. The optical properties obtained with this

approach are determined from the Fourier transform of the dipolar moment induced by the perturbation. The manuscript is divided in four chapters. The first chapter is devoted to the introduction of the ab-*initio* approaches used in the research. A review of the density functional theory and time dependent density functional theory is given. The last three chapters are devoted to the discussion of the results obtained in this project. Each of these chapters are dedicated to study a specific hypothesis at the origin of the additional peaks in the spectra of electroluminescence of molecules excited by the tunnel current:

- Constraint effect on the molecule chapter three.
- Local excitation effect in chapter four.
- The electronic nature of the local source in chapter five.

Chapter 3 is focused on the optical properties of the phthalocyanine and metal-phthalocyanine molecules. The first step of all simulations is the geometry optimization of the molecules by using DFT and the parametrization of the optical spectra computed in the framework of the linear response theory. The aim of this study is to provide a set of reference spectra used to the analysis of the structures used on the STM experiment. The second part of the chapter is devoted to the study of the molecules adsorbed on a surface of NaCl used on the experiments. The NaCl avoid the quenching deactivation of the molecules with the metallic surface in which the NaCl is supported. Two types of NaCl substrate were consider on the study, one layer of NaCl supported on three layers of gold and a NaCl bilayer.

Chapter 4 is devoted to the study of the impact of the nature of the excitation. To do this task, the real-time time-dependent theory was used. This method allows the user the study of the change in the dipolar moment due to the action of a perturbation. Several hypothesis were carried out, the first step is the study of the action of a global perturbation acting on the studied molecules. Secondly, in order to understand the action of a local perturbation mediated by the tip in the STM experiment, we developed a model describing the local action of the perturbation. This model was possible to achieve due to the fact that the software used for this proposal allows the user define a scalar potential. In this way, the treatment of this scalar potential as a Gaussian function was employed in the local perturbation analysis. The last section is devoted to the study of the energy transfer phenomena between chromophores and it was focused on the understanding of the excitation mechanism of a molecule induced by the action of a perturbation onto a second one by a dipolar-dipolar interaction.

Chapter 5 is devoted to the development of a model describing the specific action of the tunnel current. The model postulated on this chapter takes into account the phenomena involved of a tunnel current between the molecule located between the tip of the STM and the surface. The development takes into account the real nature of the tunnel current treating it as a source of electrons instead to consider it as a photon. To do this task, a wavepacket is propagated through the junction behind the framework of a non perturbative real-time time-dependent density functional theory approach. The Laplacian operators involved in the system were discretized in terms of the finite difference method.

Chapter 2

DFT and Time-dependent DFT.

The fundamental equation to describe the electronic structure of a system was postulated by Erwin Schrödinger in 1926 [64] elucidating the temporal evolution of a particle.

$$i\hbar\frac{\partial}{\partial t}|\Psi(r,t)\rangle = \hat{H}|\Psi(r,t)\rangle \tag{2.1}$$

Where i is the imaginary unit, $\hbar$ is the reduced Planck constant ($\hbar = \frac{h}{2\pi}$), Ψ the wave function of the quantum system, t the time and $\hat{H}$ is the non-relativistic Hamiltonian operator. Who is defined as:

$$\hat{H} = \left[\frac{-\hbar^2}{2m}\nabla^2 + V(r,t)\right], \tag{2.2}$$

when a single particle is subjected to a potential, $V(r,t)$, such an electric field and where ∇^2 is the Laplacian operator and m is the mass of the particle. The time-dependent Schrödinger equation described above can be described as a stationary states (no dependence on time). Stationary states are described also by a simple form of the Schrödinger equation called the time independent Schrödinger equation:

$$\hat{H}\Psi(r) = E\Psi(r), \tag{2.3}$$

where E is the eigenvalue of the Hamiltonian and is the energy level of the system.

$$\left[\frac{-\hbar^2}{2m}\nabla^2 + V(r)\right]\Psi(r) = E\Psi(r) \tag{2.4}$$

The form of the total Hamiltonian for a many-body system can be written as:

$$\hat{H} = \hat{T}_n + \hat{T}_e + \hat{V}_{nn} + \hat{V}_{ee} + \hat{V}_{en} \tag{2.5}$$

The two first terms are the kinetic energy operators for nuclei and electrons, respectively. The third and fourth terms are the repulsive electrostatic potential for nuclei-nuclei and electron-electron interactions respectively. The last term of the equation is the attractive electrostatic potential between nuclei-electron. The Hamiltonian can be fully described as:

$$\begin{aligned}\hat{H} = &-\sum_{\alpha}^{N_p}\frac{1}{2}\nabla_\alpha^2 - \sum_{i}^{n_e}\frac{1}{2}\nabla_i^2 + \frac{1}{2}\sum_{\alpha}^{N_p}\sum_{\beta\neq\alpha}^{N_p}\frac{Z_\alpha Z_\beta}{|\vec{R}_\alpha - \vec{R}_\beta|} \\ &+\frac{1}{2}\sum_{i}^{n_e}\sum_{j\neq i}^{n_e}\frac{1}{|\vec{r}_i - \vec{r}_j|} - \sum_{i}^{n_e}\sum_{\alpha}^{N_p}\frac{Z_\alpha}{|\vec{r}_i - \vec{R}_\alpha|}\end{aligned} \tag{2.6}$$

In practice, only the Hydrogen atom can be solved exactly and it is a consequence of a many body particle system. For all other cases approximations are required. The first approximation is the Born-Oppenheimer approximation.

2.1 Born-Oppenheimer approximation.

The Born-Oppenheimer approximation was postulated in 1927 [65] and consists on the splitting of the nuclear and electron wavefunction taking into account the difference of mass between them. This mass difference make the nuclei have a moment of inertia greater than the electrons (approx. 1836 times more). As a consequence, we can assume that the electrons evolve in a potential created by the nuclei which have a fix configuration. In other words, the nuclear kinetic energy can be neglected and its potential is constant. So, the total Hamiltonian in equation 2.6 can be expressed as a sum of the electronic and nuclear Hamiltonian, and also, the total wavefunction can be expressed as a product of both, electronic and nuclear wavefunctions:

$$\begin{aligned} \hat{H}_T &= \hat{H}_e + \hat{H}_N \\ \Psi_T(\vec{r},\vec{R}) &= \Psi_e(\vec{r};\vec{R})\Psi_n(\vec{R}) \end{aligned} \tag{2.7}$$

The eigenvalue system for electrons can be, now described as:

$$\begin{aligned} \hat{H}_e(\vec{r};\vec{R}) = \Psi_e(\vec{r};\vec{R}) = U(\vec{R})\Psi_e(\vec{r};\vec{R}) \\ \hat{H}_e = \hat{T}_e + \hat{V}_{ee} + \hat{V}_{eN} \end{aligned} \tag{2.8}$$

Both, electronic wavefunction ($\Psi_e(\vec{r};\vec{R})$) and the total electronic energy ($U(\vec{R})$) have a parametric dependence with respect to the nuclear coordinates. It means, that a change in the nuclear coordinates change the result of solving the electronic Schrödinger equation, but the nuclear coordinates are not involved as a variable in the resolution of Eq. 2.8.

For a given nuclear configuration, the term $\hat{V}_{nn}$ is a constant, the presence or the absence of this term in Eq. 2.8 does not have any effect on the electronic wavefunction. Although, it affects on the electronic energy. The eigenvalue $U(\vec{R})$ is called as total electronic energy (and also as nuclear potential) because it is the sum of the pure electronic energy ($E_e(\vec{R})$) and the electrostatic nuclear repulsive potential ($\hat{V}_{nn}$). Consequently, the nuclear Schrödinger equation can be written as:

$$[\hat{T}_n + U(\vec{R})]\Psi_n(\vec{R}) = E_T\Psi_n(\vec{R}) \tag{2.9}$$

Where E_T is the total energy of the system and the total wavefunction is given by Eq. 2.7. To obtain the total energy of the system, first the electronic equation has to be solved to obtain the total electronic energy $U(\vec{R})$ and the second step, with the calculated value, consist to solve the nuclear Schrödinger equation 2.9 (in this case, $U(\vec{R})$ acts as a potential energy function).

2.2 Density Functional Theory

Density Functional Theory is one of the most successful approach to calculate the electronic structure of atoms, molecules and solids. It was in 1964 that Hohenberg and Kohn [66] described a theory where the main variable was

the density of the system. Also they discovered that to fully describe a stationary electronic state, it was sufficient to know its ground state density. The density is a very convenient variable because it is a physical variable with a intuitive interpretation. It can be measured by X-Ray scattering [67] and high-energy electrons [68, 69].

The fundamental principle of the DFT is that any property of the system of many interacting particles can be expressed as a functional of the ground state density. Hohenberg and Kohn establish a variational principle in terms of the density showing that the total energy can be written as a functional of the density which minimum, the exact ground state of the system, is reached at the exact density. With this postulate they were able to finish the previous work done by Thomas [70], Fermi [71, 72] and others authors that had been trying, a mathematical definition of the total Energy as a explicit functional of the density of the system,

$$E_0 = E[\rho_0(\vec{r})]. \tag{2.10}$$

The Hohenberg and Kohn theory is based on three postulates:

- The electronic density of an interacting system of electrons uniquely determines the external potential $V(\vec{r})$ and all observables of the system.
- The ground state energy of the system can be obtained by minimizing the total energy in terms of the density.
- There exists a universal functional $F[\rho]$, who is the same for all systems with the same particle-particle interaction, such that the total energy can be written in the form:

$$E[\rho] = F[\rho] + \int dr^3 \rho(r) V(r) \tag{2.11}$$

2.2.1 Kohn-Sham equations

In 1965, Kohn-Sham [73] used an auxiliary non-interacting system to evaluate the density of the interacting system. This approach reduce the problem in a system of N-monoelectronic equations. In other words, the electrons obey a one-particle Schrödinger equation with an effective external potential V_{KS} which is a functional of the electronic density.

The monoelectronic Kohn-Sham operator can be defined as the sum of the kinetic energy operator and the effective external potential for non-interacting system:

$$\hat{H}_{KS} = -\frac{1}{2}\nabla_i^2 + \hat{V}_{eff}(\vec{r}). \tag{2.12}$$

The ground state density can be calculated as a sum over the N lowest occupied Kohn-Sham states,

$$\rho(\vec{r}) = \sum_i^N |\psi_i(\vec{r})|^2, \tag{2.13}$$

Where N is the total number of electrons and the external effective potential can be describes as:

$$V_{eff}(\vec{r}) = \hat{V}_{ext}(\vec{r}) + \hat{V}_H(\vec{r}) + \hat{V}_{xc}(\vec{r}). \tag{2.14}$$

$$\begin{aligned} V_{ext}(\vec{r}) &= -\sum_i^N \frac{Z_i}{|\vec{r} - \vec{R}_i|}, \\ V_H(\vec{r}) &= \int d\vec{r} \frac{\rho(\vec{r})}{|\vec{r} - \vec{r}'|}, \\ V_{xc} &= \frac{\partial E_{xc}[\rho(\vec{r})]}{\partial \rho(\vec{r})}. \end{aligned} \tag{2.15}$$

The first term is the external potential, which in general is the Coulomb interaction between electrons and nuclei. The second term is the Hartree term which is the classical part of the electron-electron interaction and the last term is the exchange-correlation potential. Kohn and Sham also proposed a simple approximation to V_{xc} using the local density approximation (LDA).

Using the Eq. 2.11 it is possible to define the exchange and correlation energy:

$$F[\rho] = \hat{T}[\rho] + E_H + E_{xc}[\rho]. \tag{2.16}$$

The total energy of the system in atomic units can be written as the contribution of the different terms as:

$$E_T[\rho] = T[\rho] + E_H[\rho] + E_{ext}[\rho] + E_{xc}[\rho], \tag{2.17}$$

Where $T[\rho]$ is the energy associated to the kinetic operator, $E_H[\rho]$ is the Hartree interaction, $E_{ext}[\rho]$ is the energy associated to the external potential and the last term is the exchange-correlation energy. At this point, all terms related to the total energy can be evaluated except the exchange-correlation term. In the next section, a method to compute this energy will be described using different approaches.

2.2.2 Exchange-Correlation functionals

The E_{xc} term contains the exchange term which is a result of the antisymmetric property of the wavefunction, the Coulombian electronic repulsive correlation term and the self-interaction correction term due to the indistinguishable principle for electrons. However, this term is unknown and needs to be approximated at some point to be computed. If this term could be computed without any approximation, we could have a exact functional making able the exact computation of the electronic structure. The scientific community has been focused in the development of an accurate exchange-correlation functional. For this task, different methods had been developed, the local density approximation (LDA), the generalized gradient approximations and the meta-GGA functional.

Local Density approximation

It was the first approximation developed by Kohn and Sham in 1965, and it describes the energy per particle of the homogeneous electron gas with a constant density ρ ($\epsilon_{xc}(\rho)$):

$$E_{xc}^{LDA} = \int d^3r \rho(\vec{r}) \epsilon_{xc}(\rho(\vec{r})). \tag{2.18}$$

The LDA functional as the PZ [74] or PW [75] are local, the potential energy at the point $\boldsymbol{r}$ only depends on the density at the same point. Considering this approximation one would expect good results only for systems with

slowly variation on the density, but, in fact, it yields remarkably good results even for highly inhomogeneous systems like atoms or small molecules. This type of functional does not allow to correct the effects of self interaction and describes in a wrong way certain properties such as the insulator and semiconductors gaps, the intramolecular bond energies which are overestimated, the bond distances and the cohesion of solids are underestimated.

Generalized Gradient approximation and meta-GGA

The general gradient approximation (GGA) is more complex than LDA. The general form of a GGA is:

$$E_{xc}^{GGA} = \int d^3r f(\rho(\vec{r}, \nabla\rho(\vec{r}))). \tag{2.19}$$

Besides the local density dependency, the function $\boldsymbol{f}$ also depends on the density gradient. Thus, it is possible to referred to the GGA as a semi-local approximation. In contrast with LDA where $\epsilon_{xc}(\rho)$ is unique and known to very good accuracy, the function f is uniquely defined in the limit where the dimensionless density gradient approaches to zero for a inhomogeneous gas. In this limit, f can be expressed as a response function of an uniform electron gas.

In practice, the GGA functional treat separately the exchange and correlation terms. This formulation can be based in a semi-empirical procedure, giving good results for small molecules but less good results for the systems where the electrons are delocalized as metals. The most common used functional can be the BLYP [76, 77], PW91 [78] and PBE [79] among others.

Recently, a new class of functional called meta-GGA [80] has been proposed. The difference of this functional respect to the normal GGA is the addition of a new variable, the kinetic energy density:

$$\tau(\vec{r}) = \frac{1}{2}\sum_{i}^{occ} |\nabla\phi_i(\vec{r})|^2, \tag{2.20}$$

and the energy functional expression can be written as:

$$E_{xc}^{MGGA} = \int d^3\vec{r} g(\rho(\vec{r}), \nabla\rho(\vec{r}), \tau(\vec{r})). \tag{2.21}$$

This new function g is determined in the same way as in the GGA. τ allows to improve the results obtained using the traditional GGAs functional and has a dependence on the Kohn-Sham orbitals. By virtue of the Hohenberg-Kohn theorem, a functional of the density which proves that E_{xc}^{MGGA} is still a density functional, although its functional dependence on the density is implicit. Some meta-GGA functional are TPSS [81] and M06-L [82] among others.

Hybrid functional

Hybrid functional are the result to mix the non-local Hartree-Fock exchange with LDA or GGA exchange. The first method was proposed by Becke [83]. A hybrid exchange-correlation functional is usually build up as a linear combination of the exact HF exchange functional. One of the most used hybrid functional is the B3LYP [84, 85]:

$$\begin{aligned} E_{xc}^{B3LYP} = E_x^{LDA} + a_0(E_x^{HF} - E_x^{LDA}) + a_x(E_x^{GGA} - E_x^{LDA}) \\ + E_c^{LDA} + a_c(E_c^{GGA} - E_c^{LDA}) \end{aligned} \tag{2.22}$$

Where a_0=0.20, a_x=0.72 and a_c=0.81.

E_x^{GGA} and The E_c^{GGA} are the generalized gradient approximations for the Becke88 exchange functional [76] and the correlation functional of Lee, Yang and Parr [77] for B3LYP, and the E_c^{LDA} is the VWN LDA to the correlation functional [86]. The B3LYP functional uses three fitted parameters which control the contribution of the different components. The hybrid functional are more accurate than the LDA and GGA functional.

2.3 Time-Dependent Density functional Theory.

The DFT is very useful to deal with systems where a static external potential interact with the system and is described by the *time-independent* Schrödinger equation. Nevertheless, when we want to study the interaction between an external electromagnetic field (e.g. laser field) and a solid or a molecule, it falls out of this theory. This systems should be described using the *time-dependent* Schrödinger equation using the Time-Dependent Density Functional Theory which is an extension of the ground-state DFT.

In 1984 Runge and Gross [56] proved the Hohenberg-Kohn theorem and a Kohn-Sham scheme for the time-dependent case. First of all, it is useful to describe the time-dependent Hamiltonian operator before to go beyond the Runge and Gross theorem. We start from the time dependent Schrödinger equation:

$$i\hbar\frac{\partial}{\partial t}\Psi(\vec{r},t) = \hat{H}(\vec{r},t)\Psi(\vec{r},t). \tag{2.23}$$

$\hat{H}$ is the Hamiltonian operator for a system of N-electrons interacting with a time-dependent potential and $\vec{r}$=$(r_1,....,r_n)$ are the spatial coordinates of the N electrons. The Hamiltonian, as in the independent-time case, can be decomposed into:

$$\hat{H}(\vec{r},t) = \hat{T}(\vec{r}) + \hat{V}_{ext}(\vec{r},t) + \hat{U}(\vec{r},t) \tag{2.24}$$

$$\hat{T}(\vec{r}) = -\sum_i \frac{\nabla_i^2}{2} \tag{2.25}$$

$$\hat{V}_{ext}(\vec{r},t) = \sum_i v_{ext}(\vec{r}_i,t) \tag{2.26}$$

$$\hat{U}(\vec{r}) = \sum_{i<j} \frac{1}{|r_i - r_j|} \tag{2.27}$$

The first term of Eq. 2.24 is the kinetic energy of the electrons, while $\hat{V}_{ext}$ is the time-dependent external potential under the electrons evolve, assumed constant for $t < t_0$, and the last term is the electron-electron interaction.

The expression for the external potential is written as a sum of one body term. In the case where the electromagnetic field applied is a laser beam, within the dipole approximation, the electrons feel the potential:

$$v_{ext}(\vec{r},t) = \mathcal{E} f(t) sin(\omega t)\vec{r}_\alpha, \tag{2.28}$$

Where α, ω and $\mathcal{E}$ are the polarization, the frequency and the amplitude of the laser respectively. The envelope function f(t) describes the temporal shape of the laser pulse. The probability to find at time t an electron at $\vec{r}$ is:

$$\rho(\vec{r},t) = \sum_{i}^{n} |\phi_i(\vec{r},t)|^2. \tag{2.29}$$

The density is normalized at all times to the total number of electrons N.

2.4 The Runge-Gross theorem

The Runge-Gross theorem proves that there is a one-to-one correspondence between the time-dependent external potential, $V_{ext}(\vec{r},t)$ and the electron density, $\rho(\vec{r},t)$ for a many body system evolving from an initial state which is, in general, the ground state of the system. If we know the electronic density of the system (e.g. the ground state electronic density), it is possible to get the external potential of the system. This potential can be introduced in the time-dependent Schrödinger equation and it can be solved obtaining the time-dependent many-body wavefunction. This non-trivial statement implies that if the only available information of the system is the electron density, it is possible to obtain the external potential produced by this density. From this statement, the electronic density determines all the properties of the quantum system.

The proof of the one-to-one correspondence is based on considering the quantum-mechanical equation of motion for the current-density. This proof requires the potentials $V_{ext}(\vec{r},t)$ to be time-analytical around the initial time. In this way being able to expand it in a Taylor-series in t around t=0, for a finite time interval:

$$V_{ext}(\vec{r},t) = \sum_{k=0}^{\infty} \frac{1}{k!} v_{ext,k}(\vec{r}) t^k. \tag{2.30}$$

The densities $\rho(\vec{r},t)$ and $\rho'(\vec{r},t)$ evolving from a common initial state under the influence of the $V_{ext}(\vec{r},t)$ and $V'_{ext}(\vec{r},t)$ potentials are different if the potentials differ in more than a purely time-dependent function.

$$V_{ext}(\vec{r},t) \neq V'_{ext}(\vec{r},t) + c(t). \tag{2.31}$$

Such time-dependent constant c(t) does not change the physic, if that potentials differs only in the c(t) constant, then the resulting wavefunctions differ only by a time-dependent phase factor giving the same density. At time $t = t_0$:

$$|\Psi(t_0)\rangle = |\Psi'(t_0)\rangle \equiv |\Psi_0\rangle\,, \tag{2.32}$$

$$\rho(\vec{r},t_0) = \rho'(\vec{r},t_0) \equiv \rho_0(\vec{r}), \tag{2.33}$$

$$j(\vec{r},t_0) = j'(\vec{r},t_0) \equiv j\rho_0(\vec{r}). \tag{2.34}$$

Making use of the motion equations for the density-current, it can be demonstrated that this current-densities only differ if the potentials V_{ext} and V'_{ext} differ in more than a time-dependent constant.

$$j(\vec{r},t) = \langle\Psi(t)|\,\hat{j}(\vec{r})\,|\Psi(t)\rangle\,, \tag{2.35}$$

$$j'(\vec{r},t) = \langle\Psi'(t)|\,\hat{j}(\vec{r})\,|\Psi'(t)\rangle\,, \tag{2.36}$$

$$\hat{j}(\vec{r}) = \frac{1}{2i}\sum_i^N [\nabla_i\delta(\vec{r}-\vec{r}_i) + \delta(\vec{r}-\vec{r}_i)\nabla_i]. \tag{2.37}$$

Since Ψ and Ψ' evolve from the same initial state:

$$\Psi(t=0) = \Psi'(t=0) = \Psi_0, \tag{2.38}$$

and

$$\begin{aligned}\frac{\partial}{\partial t}\left[\hat{j}(\vec{r},t) - \hat{j}'(\vec{r},t)\right]\Big|_{t=0} &= -i\,\langle\Psi_0|\left[\hat{j}(\vec{r}), \hat{H}(0) - \hat{H}'(0)\right]|\Psi_0\rangle \\ &= \rho_0(\vec{r})\nabla\left[V_{ext}(\vec{r},0) - V'_{ext}(\vec{r},0)\right].\end{aligned} \tag{2.39}$$

It can be concluded by saying that at an infinitesimal time of the initial time:

$$j(\vec{r},t) \neq j'(\vec{r},t). \tag{2.40}$$

The second proof of the theorem consists in verifying the previous theorem using the continuity equation. The potentials is expanded in a Taylor-series for $t = t_0$ around the initial time t_0 [87, 88]

$$\frac{\partial \rho(\vec{r},t)}{\partial t} = -\nabla j(\vec{r},t). \tag{2.41}$$

Considering this results, the time-dependent densities determine the potential up to a purely time-dependent constant. Therefore, the wavefunction is determined up to a purely time-dependent phase:

$$\Psi(t) = e^{-i\alpha(t)}\Psi[\rho,\Psi_0](t). \tag{2.42}$$

The expected value of any Hermitian operator $\hat{A}$(t) is uniquely a functional of the density and the initial state analogous to the time-independent case.

$$A[\rho,\Psi_0](t) = \langle \Psi[\rho,\Psi_0](t)|\,\hat{A}(t)\,|\Psi[\rho,\Psi_0](t)\rangle \tag{2.43}$$

In the time-independent case, we cannot used directly a variational principle as in the time-independent case but the problem can be solved using the quantum-mechanical action to convert the solution of the Schrödinger equation into a variational problem:

$$A[\Psi] = \int_{t_0}^{t_1} \langle \Psi(t)|\, i\frac{\partial}{\partial t} - \hat{H}(t)\,|\Psi(t)\rangle\,. \tag{2.44}$$

The true time-dependent density is the one which makes the action stationary

$$\frac{\delta A[\Psi]}{\delta \langle \Psi(t)|} = 0. \tag{2.45}$$

Runge and Gross, to prove their theorem, started with the action of Eq. 2.43 but they found that the response functions obtained are not casual [89, 90]

and to derive the variational equation two independent boundary conditions must be imposed $\delta\Psi(t_0)$=$\delta\Psi(t_1)$=0. In TD-DFT this two conditions are not independent because the value of the density at t_1 is determined by the value at t_0 [91]. In 1998, van Leeuwen [92] solved this problems using the Keldysh [93] formalism for the causality problem and the second was solved by introducing a new action functional that does not contain explicitly the time derivative $\partial/\partial t$:

$$A[\rho] = -iln\left\langle \Psi(t_0|\hat{U}(\tau_f,\tau_i)\left|\Psi(t_0\right\rangle + \int_{\tau_0}^{\tau_1} d\tau \frac{dt}{d\tau}\int d^3r\rho(\vec{r},\tau)v_{ext}(\vec{r},\tau). \quad (2.46)$$

Where τ is the Keldysh pseudo-time and $\hat{U}$ is the evolution operator of the system

$$\hat{U}(\tau_f,\tau_i) = \hat{T}_c exp\left[-i\int_C^{\tau_i\to\tau_f} dt\hat{H}(\tau)\right]. \quad (2.47)$$

$\hat{T}_c$ denotes ordering in τ. The causality problem is solved, the response functions calculated are symmetric in Keldysh pseudo-time and casual when converted in real time.

2.5 Time dependent Kohn-Sham equations.

The extension of the Kohn-Sham equation into the time-dependent density functional theory is a trivial task after the development of the Runge and Gross theorem explained in the previous section. The first step is to build the auxiliary system of non-interacting electrons. The Kohn-Sham time-dependent equation is written as:

$$i\frac{\partial}{\partial t}\Psi_i(\vec{r},t) = \hat{H}_{KS}(\vec{r},t)\Psi_i(\vec{r},t). \quad (2.48)$$

The Kohn-Sham Hamiltonian is defined as:

$$\hat{H}_{KS}(\vec{r},t) = -\frac{\nabla^2}{2} + V_{KS}[\rho](\vec{r},t). \quad (2.49)$$

The existence of a potential $V_{KS}[\rho](\vec{r},t)$ yields the density of the interacting system:

$$\rho(\vec{r},t) = \sum_{i}^{N} |\phi_i(\vec{r},t)|^2. \tag{2.50}$$

The time-independent effective potential, $V_{ks}(\vec{r},t)$ can be defined as:

$$V_{KS}[\rho](\vec{r},t) = V_{ext}(\vec{r},t) + \int d^3r \frac{\rho(\vec{r}',t)}{|\vec{r}-\vec{r}'|} + V_{xc}[\rho](\vec{r},t). \tag{2.51}$$

V_{ext} is the external potential that the electrons feel, the second term is the Hartree potential and takes into account the classical electrostatic interaction between electrons. $V_{xc}[\rho](\vec{r},t)$ is the exchange-correlation potential, including all non-trivial many body effects:

$$V_{xc}(\vec{r},t) = \left.\frac{\delta A_{xc}[\rho]}{\delta\rho(\vec{r},\tau)}\right|_{\rho=\rho(\vec{r},t)}. \tag{2.52}$$

A_{xc} can be defined as:

$$A[\rho] = A_{KS}[\rho] - A_{xc}[\rho] - \frac{1}{2}\int_{\tau_0}^{\tau_1} d\tau \frac{dt}{d\tau} \int d^3\vec{r} \int d^3\vec{r}' \frac{\rho(\vec{r},\tau)\rho(\vec{r}',\tau)}{|\vec{r}-\vec{r}'|}, \tag{2.53}$$

where $A_{KS}[\rho]$ is the Kohn-Sham functional written in Eq. 2.46.

2.6 Exchange-Correlation potentials.

The development of time-dependent functional is still in early work, on the other way round to the normal DFT where a huge number of approximations are already done. In TD-DFT the simplest and common approximation is the adiabatic local density approximation (ALDA). In the limit of an external potential which varies slowly in time is reduced to:

$$A_{xc} = \int_{\tau_0}^{\tau_1} E_{xc}[\rho]dt. \tag{2.54}$$

E_{xc} is the exchange-correlation functional of the time-independent Kohn-Sham theory. This exchange-correlation functional is evaluated at each time from the density $\rho(\vec{r},t)$. The adiabatic approximation is a local approximation in time:

$$V_{xc}[\rho](\vec{r},t) = \frac{\delta A_{xc}[\rho]}{\delta\rho(\vec{r},t)} \cong \tilde{v}_{xc}[\rho](\vec{r})|_{\rho=\rho(\vec{r},t)}, \tag{2.55}$$

Where $\tilde{v}_{xc}$ is a exchange-correlation functional of the DFT ground-state. Using this assumption, the ALDA functional keep the same problems as the LDA approximation, *i. e.*, the same incorrect asymptotic behaviour as the LDA potentials. It is important to note that V_{xc} is a functional of density over the time and space while $\tilde{v}_{xc}$ is a functional of density over only the space, the time being fixed.

2.7 Linear Response theory

In the time-dependent density functional theory the goal is to find the response of the density due to an external electromagnetic field with respect to the time to obtain the linear absorption spectra of a molecule using a weak field to solve the time-dependent Kohn-Sham equations. The linear response time-dependent theory correspond to the response of a initially stationary state due to a perturbation switched on at t=0. The total potential is given by:

$$v_{ext}(\vec{r},t) = v_{ext,0}(\vec{r}) + \delta v_{ext}(\vec{r},t). \tag{2.56}$$

A Taylor series can be used to express the response of any observable (normally the density) related to δv_{ext}. Linear response is concerned with the first order-term ($\rho_1(\vec{r},t)$) of the Taylor expansion. The change of density due to a perturbation of the system by a small change of the external potential can be estimated from the dynamical susceptibility linear response function $\chi(\vec{r},\vec{r}',t)$ as:

$$\delta\rho(\vec{r},\omega) = \int d^3r' \chi(\vec{r},\vec{r}',\omega) v_{ext}(\vec{r}',\omega), \tag{2.57}$$

with

$$\chi(\vec{r}t,\vec{r}'t') = -i\omega(t-t')\langle\Psi_0|\left[\hat{\rho}_{H_0}(\vec{r},t),\hat{\rho}_{H_0}(\vec{r},t)\right]|\Psi_0\rangle, \tag{2.58}$$

Where $\hat{n}_{H_0} = e^{iH_0t}\hat{n}e^{-iH_0t}$ and $\omega(t-t')$ is the step function ensuring that the response function is properly casual and $\hat{\rho}(\vec{r})$ is the density operator:

$$\hat{\rho}(\vec{r}) = \sum_i \delta(\vec{r}-\vec{r}_i). \tag{2.59}$$

By inserting the completeness relation $\sum_i |\Psi_i\rangle\langle\Psi_i| = 1$ and by performing a Fourier transform with respect to $t-t'$, we get the Lehmann representation for the density response function:

$$\begin{aligned}\chi(\vec{r},\vec{r}',\omega) = \lim_{\eta\to 0^+}\sum_i \Bigg[&\frac{\langle\Psi_0|\hat{\rho}(\vec{r})|\Psi_i\rangle\langle\Psi_i|\hat{\rho}(\vec{r}')|\Psi_0\rangle}{\omega-(E_i-E_0)+i\eta} \\ &-\frac{\langle\Psi_0|\hat{\rho}(\vec{r}')|\Psi_i\rangle\langle\Psi_i|\hat{\rho}(\vec{r})|\Psi_0\rangle}{\omega+(E_i-E_0)+i\eta}\Bigg]\end{aligned} \tag{2.60}$$

In the case of a non-interacting system the previous equation can be quite simplified:

$$\chi(\vec{r},\vec{r}',\omega) = \sum_{jk}^{\infty}(f_k-f_j)\frac{\phi_j(\vec{r})\phi_j^*(\vec{r}')\phi_k(\vec{r}')\phi_k^*(\vec{r})}{\omega-(\epsilon_j-\epsilon_k)+i\eta} \tag{2.61}$$

Where f_k is the occupation of the state k. This equation involves the excitation of a single particle from an occupied state to an unoccupied state. The time-dependent exchange and correlation kernel, f_{xc}, to obtain the true electron density-response form the KS system can be written as:

$$f_{xc}[\rho_{gs}](\vec{r},\vec{r}',t-t') = \left.\frac{\delta v_{xc}[\rho](\vec{r},t)}{\delta\rho(\vec{r}',t)}\right|_{\rho=\rho_{gs}}. \tag{2.62}$$

For a given δv_{ext} the first order change in the time-dependent Kohn-Sham potential is an exact representation of the density response of the interacting system [59, 94–97]:

$$\delta v_{ks}(\vec{r},t) = \delta v_{ext}(\vec{r},t) + \int d^3r' \frac{\rho_1(\vec{r}',t)}{|\vec{r}-\vec{r}'|} + \int d^3t' \int d^3r' f_{xc}[\rho_{gs}](\vec{r}t,\vec{r}'t')\rho_1(\vec{r}'t'). \tag{2.63}$$

Following Casida's work, Eq. 2.61 can be transformed into a matrix representation:

$$\begin{pmatrix} L & K \\ K^* & L^* \end{pmatrix} \begin{pmatrix} X \\ Y \end{pmatrix} = \omega \begin{pmatrix} -1 & 0 \\ 0 & 1 \end{pmatrix} \begin{pmatrix} X \\ Y \end{pmatrix}.$$

The Casida equation yields the exact excitation energies of any many-body system. The exact Kohn-Sham ground state of the system must be calculated. All occupied and unoccupied Kohn-Sham orbitals and energy eigenvalues are needed including the continuum states. Also, the exact frequency-dependent exchange-correlation Kernel is required. Since the elements of the matrices A and B depend on the frequency, an iterative scheme is required. In practice, none of these requirements can be satisfied exactly. Setting the coupling-matrix elements to zero, the Casida equation simply reproduces the Kohn-Sham excitation energies as eigenvalues.

2.8 Real Time density functional theory.

The linear response quantities for the time-dependent Kohn-Sham equations, which contains the response of the system to all orders, by adding a perturbing field to the Kohn-Sham potential and propagating it in time was proposed by Yabana and Bertsch [98–100]. The wavefunction of the ground state has been changed and then propagated for some time:

$$\phi(\vec{r},\delta t) = e^{i\kappa x_j}\phi(\vec{r}), \tag{2.64}$$

where κ is a small momentum in the direction x_j to the electrons. The dynamic polarizability $\alpha(\omega)$ is essentially the Fourier transform of the dipole moment of the system.

$$\alpha_{ij}(\omega) = -\frac{1}{\kappa}\int dt \int d^3r x_i \delta\rho(\vec{r},t)e^{-i\omega t} \tag{2.65}$$

2.8.1 Propagators in real time density functional theory.

The propagators are Green functions, the solution of a differential equation, giving the probability amplitude for a particle to travel from one place to another in a given time. The traveller particle can be real or virtual, and the Feynman diagrams is essentially the representation of the particle propagators of virtual particles between nodes. Formally the solution of the time-dependent Schrödinger equation with a time independent Hamiltonian is simply:

$$\phi(t) = e^{-it\hat{H}}\phi_0. \tag{2.66}$$

$\phi(t)$ is computed from ϕ_0 in an interval [0,t] and this option is not convenient. To solve this problem it needs to break the interval [0,t] into smaller intervals. The time propagator can be written as:

$$\hat{U}(t,0) = \prod_{i=0}^{N-1} \hat{U}(t_i + \delta t_i, t_i), \tag{2.67}$$

by using the property $\hat{U}(t_1,t_2) = \hat{U}(t_1,t_3)\hat{U}(t_3,t_2)$ and the fact that t_0=0, $t_{i+1} = t_i$ and $t_n = t$. Splitting in small intervals has a double goal:

- the time-dependent Hamiltonian is smoothed
- and the norm of the argument of the exponential is reduced by increasing lineally the norm with Δt.

With this convenience reasons, there is a natural limit to the maximum size of Δt. From a numerical point of view, the propagation algorithm should be stable and accurate. The propagator is stable below Δt_{max} if $\Delta t < \Delta t_{max}$ and n > 0 where $\hat{U}^n(t + \Delta t, t)$ is uniformly bounded. If the algorithm is unitary, it is also contractive and hence stable. A contractive algorithm reduce the norm as a consequence the error will grow smaller.

Unfortunately, the evaluation of the exponential with the well known methods arise to a computational limitation due to the matrix order (less than a few thousands). An alternative is the use of a iterative method that yield directly to $\exp(\hat{A})v$. These methods have a much better scaling with the order of the matrix. The most famous technique is the polynomial expansion

where the exponential of a matrix $\hat{A}$ is defined by the Taylor expansion approximation the exponential as:

$$taylor_k[\hat{A}, v] = \sum_{n=0}^{k} \frac{1}{n!} \hat{A}^n v. \tag{2.68}$$

For a given k, the method is of order k and requires k matrix-vector operations. The truncation of this series at a given k breaks the unitary of the exponential. A Kyrlov subspace projection $\kappa_m \hat{A}, v$ for a given operator $\hat{A}$ and vector v is defined as:

$$\kappa_m[\hat{A}, v] = kyrl[v, \hat{A}v, \hat{A}^2 v, ..., \hat{A}^{m-1} v]. \tag{2.69}$$

The dimension of $\kappa_m \hat{A}, v$ may be smaller than m if v does not have non-null components of at least m distinct eigenvectors of $\hat{A}$. This projection is solved with the Lanczos procedure generating recursively and orthogonal base as:

$$\hat{A}\hat{V}_m = \hat{V}_m \hat{H}_m + h_{m+1,m} v_{m+1} e_m^T, \tag{2.70}$$

where $\hat{V}_m$=[v_1,...,v_m], $\hat{H}_m$ is an mx, symmetric tridiagonal matrix and e_i is the i-nth unit vector. The method consist to approximate any function and specifically the exponential:

$$lanczos_k[\hat{A}, v] = \hat{V}_k exp(\hat{H}_k) e_1. \tag{2.71}$$

Accurate values are obtained for relatively small values of k. The Krylov subspace projection is an order k method that requires k matrix-vector operations.

After the description of the approximations used to the exponential we now analyse the approximation of the evolution operator. Most methods require the knowledge of $\psi(\tau)$ and $\hat{H}(\tau)$ for $0 \leq \tau \leq$, and also the Hamiltonian at some points in time between $t \leq \tau \leq t + \Delta t$. The Hamiltonian can be obtained by extrapolation, propagating ψ to get $\psi(t + \Delta t)$, from $\psi(t + \Delta t)$ to obtain $\hat{H}(t + \Delta t)$. One of the most common methods is the exponential midpoint rule which consists in approximating the propagator by the exponential calculated at time $t + \Delta t/2$:

$$\hat{U}_{EM}(t+\Delta t,t) = exp[-i\Delta t\hat{H}(t+\Delta t/2)]. \tag{2.72}$$

The exponential is obtained exactly and $\hat{H}(t+\Delta t/2)$, which is obtained self-consistently, is unitary and time reversible. This method also requires small time steps to be stable. The term time reversible means that propagating backwards $\Delta t/2$ starting from $\psi(t+\Delta t)$ or propagating forwards starting from $\psi(t)$ should lead to the same result. The simplest approximation to the propagator leads to the condition:

$$exp\left(+i\frac{\Delta t}{2}\hat{H}(t+\Delta t)\right)\psi(t+\Delta t) = exp\left(-i\frac{\Delta t}{2}\hat{H}(t)\right)\psi(t). \tag{2.73}$$

The expression can be rewritten in terms of the propagator expression as:

$$\hat{U}(t+\Delta t,t) = exp\left(-i\frac{\Delta t}{2}\hat{H}(t+\Delta t)\right)\times exp\left(-i\frac{\Delta t}{2}\hat{H}t\right). \tag{2.74}$$

The exponential mid-point rule combined with the Lanczos exponential approximation gives a very accurate algorithm to represent the time propagator for a wide range of systems.

2.9 Conclusions

In this chapter I give a brief introduction of the theoretical background used in this work. The Density functional theory and the Time-Dependent density functional theory are explained. Density functional theory was selected due to the fact that it is one of the most successful approach to calculate the electronic structure of a determinate system. It is based on the Hohenberg and Kohn theory with the electronic density as the main variable to fully describe the ground state of the system. This methodology provides information about the electronic structure of the system allowing to describe its behaviour from a theoretical point of view. The time dependence is included in the extended version of the DFT. The Time Dependent Density functional theory was described by Runge and Gross with the one-to-one correspondence theorem between the time dependent external potential and the electron density. This method using the density as a variable are becoming more and more, growing exponentially the number of papers peer year.

The goal of our study is to understand the behaviour of a molecule subjected to an external potential (tunnel current from a STM experiment). To do this task, the TD-DFT under two different approaches like the linear response theory and the real time TDDFT is used. The real time-TDDFT shows the evolution of the density in contact with an external electromagnetic field during the time. The wavefunction is propagated in real space for some time obtaining a variation of the dipolar moment of the molecule. The Fourier transform of the dipolar moment variation is essentially the dynamic polarizability of the system. This physical variable gives us the photoabsorption spectra of the molecule. With the photoabsorption spectra we are able to describe the excitation (or emission) mechanism of the molecules perturbed by a electromagnetic field.

Chapter 3

Optical properties of phthalocyanine molecule and derivates.

Phthalocyanines were discovered in 1907 by Braun & Tchemiac [101] when they were investigating the reaction between the phthaloamide and acetic anhydrid. As a result of the reaction, traces of a blue compound were obtained. The meaning of phthalocyanine come from the Greek terms naptha (rock oil) and cyanine (dark blue) and was described for first time in 1933 by Linsteadi [102–106] and Robertson [107–110]. In 1949, copper phthalocyanine polymers were synthesized for first time by Ciba [111]. Ciba's report describes a black pigment from the reaction of 4,4'-dicyanobenzophenon-3,3'-dicarboxyl acid with cupric chloride and ammonium molybdate as catalyst. Moskalev and Kirin reported the preparation of a rare earth metal phthalocyanine [112, 113] in 1960's.

The discover of phthalocyanine and derivates have been a great advance in the field of the pigment industry. Phthalocyanines have acquired great importance as coloring pigments for their high power of pigmentation, the brightness, its high light fastness, the moderate cost of production (manufacturing), high thermal stability and blue-green pigmentation in a region of the visible spectrum have caused the phthalocyanines to become, since 1934 and continuing to the present day, the object of intensive worldwide investigations, particularly with respect to applications in the field of color. In addition, phthalocyanines are exploited commercially from optical data storage, catalysis and photoconductors. Therefore, phthalocyanines are used as materials for non-linear optics, liquid crystals, ordered thin films, photodynamic cancer therapy, molecular semiconductors, components of highly conducting charge-transfer salts , photovoltaic devices, fuel cells, and sensors [114–118].

Photophysical properties of phthalocyanines are stronger correlated by the metallic atom nature located at the center of the ring [119–121]. Metallophthalocyanines with diamagnetic metals as Zn^{+2}, Al^3 and Ga^3 give high quantum fields for the generation of triplet states. Zn and Al phthalocyanines increase the phototoxicity of the molecule in biological systems [122]. Zincphthalocyanine, for example, when excited by visible light in the range of 650 nm, induces photodynamic damage to cellular and perinuclear membranes, causing lysis and a necrotic or apoptotic response that can lead to tumor cell death [123–125]. The implementation of phthalocyanine as photosensitizers agents in cancer treatments is growing due to the excellent photophysical and photobiological properties of the compound and also due to the minimal side effects [126–128].

Phthalocyanine comprises one of the most studied classes of functional organic materials. Commonly, phthalocyanines are associated with porphyrins due to the similarities between both structures. Phthalocyanines have four isoindol rings linked by nitrogen atoms. In the other hand, porphyrins are composed by four pyrrol rings linked by carbon atoms. It is a large planar aromatic macrocyclic with a empirical formula $C_{32}H_{18}N_8$ composed by four isoindole units linked by nitrogen atoms with a ring system consisting of 18-π electrons giving a chromophore nature (Fig. 3.1). The coordination chemistry of the phthalocyanine is a huge field of study. The extensive delocalization of the π-electrons give to the molecule useful properties, lending itself to applications in dyes and pigments. Metal complexed derived from XPc (X=metal) where the two Hydrogens in the center of the molecule have been replaced by metals from every group of the periodic table present a D_{4h} symmetry group and are valuable in catalysis, organic solar cells and photodynamic therapy [129–131].

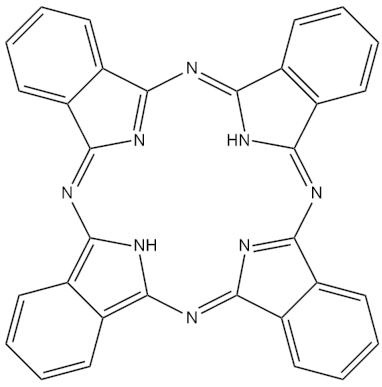

Figure 3.1: Phthalocyanine structure represented as sticks.

The hyperconjugation along the π-system leads to a bigger absorption wavelength band than porphyrins. The purity and dark blue color of phthalocyanines arise from an isolated band (Q-band) in the far-red of the visible spectrum of light around 670 nm and second band (B band) near 340 nm. The Q band arises from the doubly degenerated transition due to the LUMO degeneracy. The free-metal phthalocyanine presents a D_{2h} symmetry, and as a consequence, all states are non-degenerated. However, free-metal phthalocyanines strongly absorb light between 600 and 700 nm, thus these materials are blue or green [132–134]. Substitution can shift the absorption towards longer wavelengths, changing color from pure blue to green to colorless (when the absorption is in the near infrared). The π-orbital conjugation have a profound effect on the orbital structure of the phthalocyanine chromophore. This bathochromic shift is showed on the lowest-energy absorption band (Q-band) in the visible region of the spectrum and a strong enhancement of its intensity. There are many derivatives of the parent phthalocyanine, where either carbon atoms of the macrocycle are exchanged for nitrogen atoms or the peripheral hydrogen atoms are substituted by functional groups like halogens, hydroxyl, amine, alkyl, aryl, thiol, alkoxy and nitrosyl groups. These modifications allow for the tuning of the electrochemical properties of the molecule such as absorption and emission wavelengths and conductance [135].

3.1 Parametrical optimization

`Octopus` [136] software is an *ab-initio* code developed in the framework of the finite difference method. The finite difference method is one of the simplest and of the oldest methods to solve differential equations. The principle of the method is to solve ordinary differential equations by approximating the laplacian operator by replacing the derivate in equations using differential quotients. Consider an analytical function f(x) and its representation on a uniform grid with constant grid spacing h. The values f_i=f(x_i) correspond to the function evaluated at the grid point x_i. The main concept is related to the definition of the derivate of a smooth function f at a point x $\in \mathbb{R}$:

$$f'(x) = \lim_{h \to 0} \frac{f(x+h) - f(x)}{h}. \tag{3.1}$$

The grid spacing should be sufficiently small to get a good approximation. By using a Taylor expansion up to second order one can express the value of the analytical function in terms of the neighbours to both sides:

$$f''(x) = \frac{f(x-1) - 2f(x) + f(x+1)}{h^2}, \tag{3.2}$$

by using a 3-point centered scheme for the second-order derivate. The problem can be written in the matrix form as:

$$\begin{pmatrix} c(x_1) & 0 & \dots & \dots & 0 \\ 0 & c(x_2) & \dots & \dots & \vdots \\ \vdots & \ddots & \ddots & \ddots & \vdots \\ \vdots & \ddots & \ddots & c(x_{n-1}) & 0 \\ 0 & \dots & \dots & 0 & c(x_n) \end{pmatrix} \begin{pmatrix} f(x_1) \\ f(x_2) \\ \vdots \\ f(x_{n-1}) \\ f(x_n) \end{pmatrix} = \begin{pmatrix} f(x_1 + \frac{\alpha}{h^2}) \\ f(x_2) \\ \vdots \\ f(x_{n-1}) \\ f(x_n + \frac{\beta}{h^2}) \end{pmatrix}.$$

Using this matrix description it is easy to rewrite the Laplacian and obtain the eigenvalues and eigenvectors by diagonalizing the matrix using different methods as Davidson [50] or conjugated gradient [137].

3.1.1 Spacing parametrization.

The distance between the points of the mesh is defined by the spacing between them. The optimal values used in the finite difference method are between 0.12 Å and 0.20 Å. It should be noted that as much smaller the value of the spacing is, better is the accuracy of the simulation. In contrast, the number of points of the grid is larger when a small value of spacing is used. It implies longer computational time and more memory requirement. The objective is thus to determine the value of the spacing which offers the best compromise between computational time and accuracy of the simulation. In order to determinate the properly spacing values, the total energy of the system is taken into account.

The total energy of the system is an important quantity because it is used to determine when a structure is optimized during a structural relaxation. The total energy convergence is shown in Fig.3.2 and the converged values for the molecules of study are in the range of 0.14-0.16 Å. The selected value for the ground state simulations is 0.16 Å. A smallest value can be used but the simulation time increases due to a higher number of points chosen in the mesh distribution. Fig. 3.3 display the evolution of the lowest excitation energies, the oscillator strength and the dipolar moment transition versus the spacing.

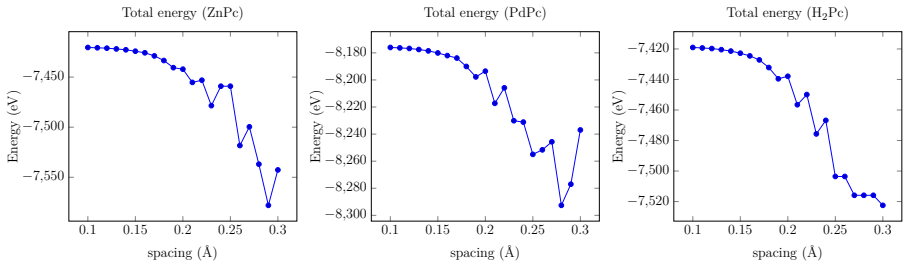

Figure 3.2: Total energy evolution as a function of the spacing between two neighbours of the mesh. a) ZnPc, b) PdPc and c) H_2Pc.

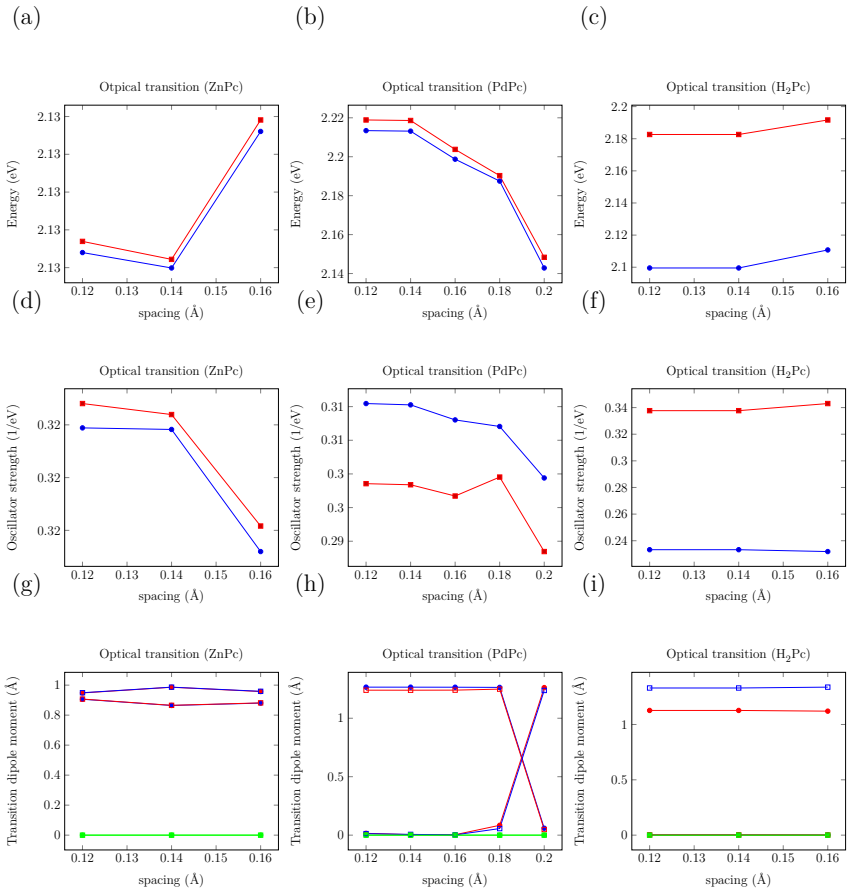

Figure 3.3: Evolution of the excitation energies (a,b,c), the oscillator strength (d,e,f) and the dipolar moment transitions (g,h,i) in the x, y and z directions as a functions of the spacing between two points of the mesh with a radius of 4.5 Å.

As in the case of the total energy parametrization as a function of the spacing, a convergence is shown when the distance between points also decreases. The oscillator strength, the dipolar moment transition and the excitation energies show a similar behaviour and a value of 0.14 Å for the spacing should be selected for the time-dependent simulations.

3.1.2 Radius parametrization.

The second variable to be parametrized in Octopus software is the Radius. It is defined as the radius of the simulation box and takes into account the number of points needed to build it. In other words, this parameter is used to restrict the number of points where the wavefunction is computed. It implies a reduction in the size of the matrices involved to solve the system. The radius also determine the size and shape of the simulation box. In Octopus it can be built as spherical, cylindrical or parallelepiped shape. This box is divided in intervals and as much number of points are taken into account more precise can be the simulation ruled by the spacing.

The normal values of the radius are in the range 3.5-6.5 Å and it corresponds with the pseudopotential domain for atoms. As the same procedure followed with the spacing parametrization, the total energy of the system is plotted versus the value of the radius Fig. 3.4, The selected value for the ground state simulations is 4.5 Å. A larger value can be used but the simulation time increases due to a construction of a bigger simulation box. As the case of the spacing, it is translated into a bigger number of points to take into account during the simulation.

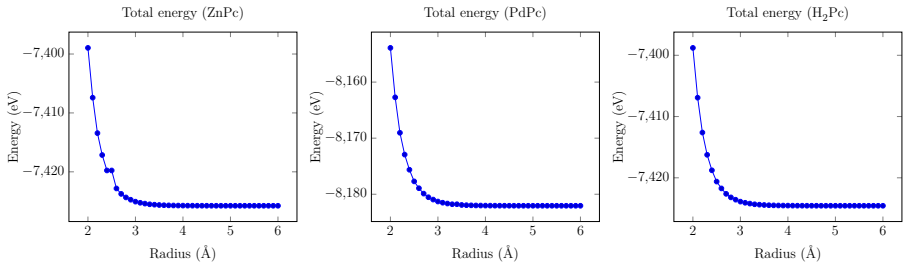

(b) (b) (c)

Figure 3.4: Total energy evolution as a function of the radius. a) ZnPc b) PdPc and (c) H_2Pc.

For Fig. 3.5 a spacing of 0.14 Å was chosen. The convergence of the parameters implies the use of a radius bigger than 5.0 Å for the TD-DFT

simulations and a radius bigger than 6.0 Å requires an important amount of memory. It is related to the size of the simulation box as bigger is it the number of points to describe increase as described above.

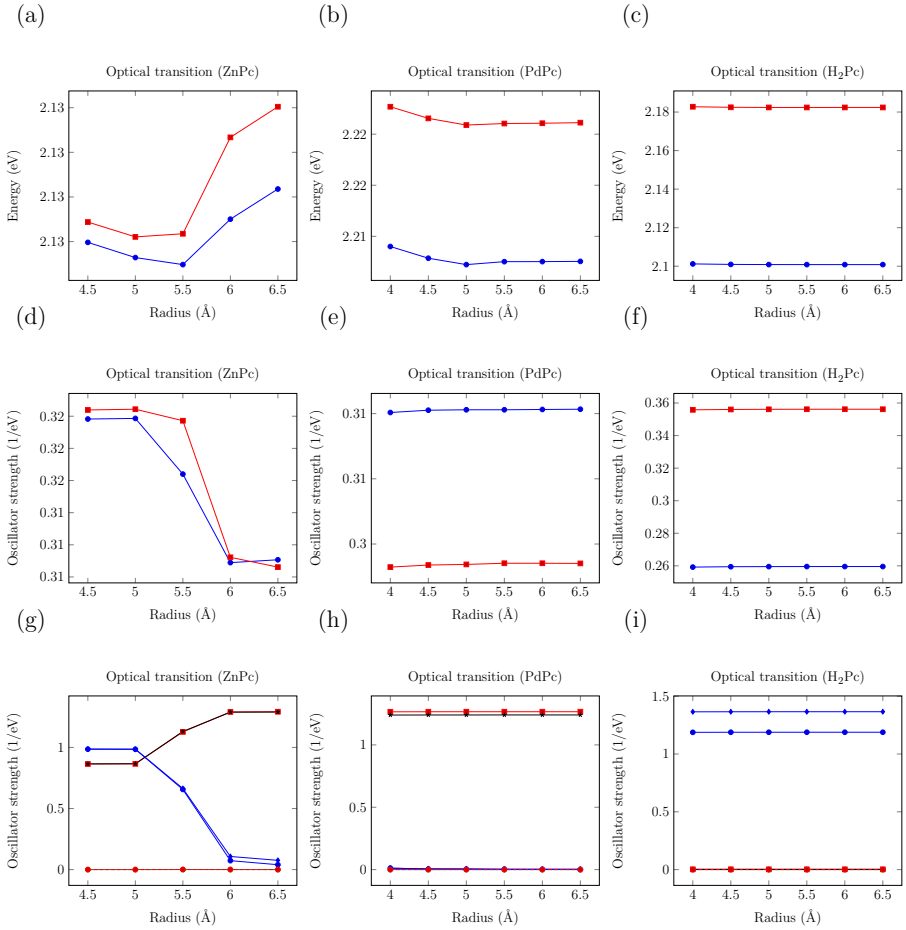

Figure 3.5: Evolution of the excitation energies (a,b,c), oscillator strength (d,e,f) and the dipolar moment transitions (g,h,i) in the directions x, y and z as a function of the radius. Note that the molecule is located in the xy plane and the z axis perpendicular to it.

3.1.3 Geometry optimization of H_2Pc, ZnPc and PdPc

The geometry optimization of phthalocyanine molecules is the starting point to compute the optical spectra. Consequently, the excitation mechanism of the molecule could be explained looking on the main transitions of the molecule. The Kohn-Sham equations, as well as the Poisson equation used to compute the Hartree potential, were discretized using finite difference. In

the framework of the finite difference method, the Kohn-Sham orbitals, the electronic density and the potentials are represented by their values over an array of points distributed in real space. The Laplacians of the computed quantities at each grid point were approximated by a sum over the values of these quantities at neighbouring points multiplied by a weight depending on the required precision [138]. A conjugated gradient (CG) scheme was used as eigensolver to get the lowest eigenvalues and eigenvectors of the Kohn-Sham equations and as the method for solving the Poisson equation. The exchange and correlations terms were described using the local density approximation in terms of the Perdew and Zunger parametrization [62] for the electron-electron interactions. The ion-valence electron interactions were modeled by replacing the ionic cores by norm-conserving pseudopotentials [44].

A damped dynamics was used to perform the structural optimization of the system. The atoms were moved according to Newton's equation by using the FIRE algorithm [139] with a velocity Verlet scheme as molecular dynamic integrator [140]. The structural optimization were carried out until the minimum force acting on each atom was weaker than 10^{-3} a.u. The selected values for the structural relaxation for spacing is 0.16 Å and 4.5 Å for radius for all molecules. The description of the bonds, angles and dihedrals for H_2Pc are shown in Table 3.1 taking into account the atom labels like in Fig 3.6. The optimize geometry of H_2Pc has a D_2h symmetry composed with a C_2 rotational axis perpendicular to the plane which contains the molecule. Also two C_2 axis are perpendicular to the main axis, one axis cross the molecule through the Hydrogens H17 and H18 and the second one through the nitrogen atoms N2 and N6. The molecule also contains 3 symmetry planes. The main one is the plane which contains the molecule and the other two planes are perpendicular to the main one. The three planes contain the 3 C_2 axis present in the molecule. The D_2h symmetry simplifies the description of the bonds, angles, and dihedral angles of the molecules due to the equivalent positions.

All the parameters are in a good agreement with the experimental values [141]. The C-N bonds in the pyrrol ring match with the experimental value of 1.37 Å. The imine bond C-N has a value of 1.32 Å meanwhile the experimental values are 1.28 Å (C=N) and 1.46 angstrom (C-N), the value obtained is a mean value between single and double bond due to the hyperconjugation present in the molecule along the π system. The C-H bonds are in the normal range (1.09 Å) as well as the C-C bonds in the pyrrol and the benzene ring. The dihedral angles confirm the planarity of the molecule and the angles are also in a normal range.

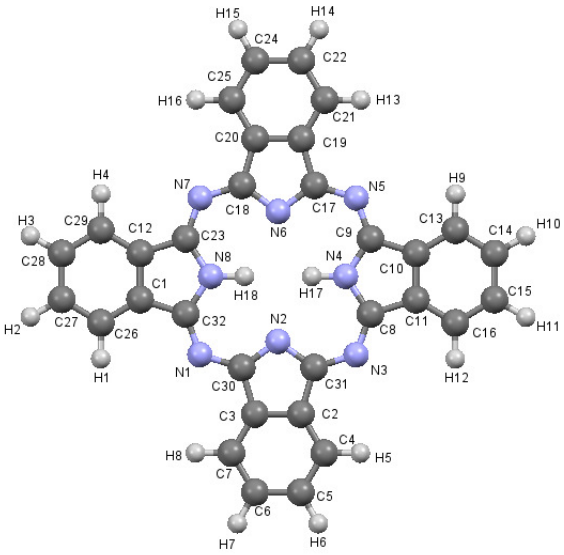

Figure 3.6: Asymmetric unit of phthalocyanine.

Bond distance (Å)		Angles (°)		Dihedral angles	
C-H	1.09	C-C-H (b.r.)	120	C-C (b.r.)	0
N-H	1.03	C-C-C (b.r.)	118-121	C-C-C-N (p.r)	0
C-N (p.r.)	1.37	C-C-C (p.r.)	105-107	N-C-N-C	180
C-N	1.32	C-N-C (N-C-N)	127	C-C-C-N (p.r)	0
C-C (b.r)	1.38-1.40	C-N-C (p.r.)	108-113		
C-C (p.r)	1.45-1.46	C-N-H	123		

Table 3.1: Structural parameters obtained in the geometry optimization of H_2Pc.

In table 3.2 the bonds, angles and dihedral angles for ZnPc are shown and labeled as in Fig. 3.7. The ZnPc molecule has a D_4h symmetry due to the Zn central atom. The molecule contains a C_4 axis perpendicular to the plane in which the molecule is contained, four C_2 axis are perpendicular to the main axis. The first one goes through the Nitrogen atoms N2 and N6, the second through N1 and N5, the third through N4 and N8, the fourth through N3 and N7. Therefore, the molecule has 5 planes, the main plane is the one which contains the molecule, the other four planes are perpendicular to the main one and contains the four C_2 axis perpendicular to the C_4.

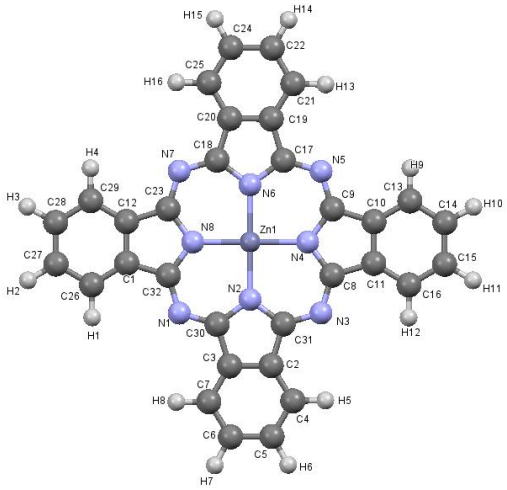

Figure 3.7: Asymmetric unit of ZnPc.

Bond distance (Å)		Angles (°)		Dihedral angles	
C-H	1.1	N-Zn-N	90	C-C-C-C (b.r.)	0
N-Zn	1.93	C-C-C (b.r.)	118-121	C-C-C-N (p.r)	0
C-N (p.r.)	1.39	C-C-C (p.r.)	106	N-C-N-C	180
C-N	1.33	N-C-N	127	C-C-C-N (p.r)	0
C-C (b.r)	1.39-1.40	C-N-C (p.r.)	107	N-C-N-Zn	0
C-C (p.r)	1.46	C-N-C	122		

Table 3.2: Structural parameters obtained in the geometry optimization of ZnPc. b.r= benzene ring and p.r= pyrrol ring

The same comments given for H_2Pc with the imine bonds (C-N and N=C are 1.33 Å) can be given to ZnPc. In this case the hyperconjugation is bigger due to a higher symmetry in the system. The C-H bonds and H-C-H (or H-C-C) angles are in a normal range as the same of C-N bonds and C-N-C angles in the pyrrol ring. The molecular is planar verified by the dihedral angles which are 0° or 180°. The N-Zn distance of 1.93 Å is a bit underestimated in comparison with experimental values in which give a average distance of 1.98-2.12 Å depending on the complex of study [142–144].

The PdPc molecule present a D_4h symmetry and has the same spatial configuration as the ZnPc molecule with a C_4 axis as the main one and four C_2 perpendicular to it, five planes containing all the rotational axis. In table 3.3 the bonds, angles and dihedral angles are shown. In Fig. 3.8 the atoms with labels are presented. The overall bonds and angles are in the normal range. However, due to the strong hyperconjugation in the molecule along the π system, the imine bonds for C-N=C system is between a single and double bond (1.33 Å while C-N is 1.46 Å and C=N is 1.28 Å). The N-Pd bond is in the normal range 2.02 Å, depending of the complex formed the range for this distance is between 1.94-2.13 Å [145, 146].

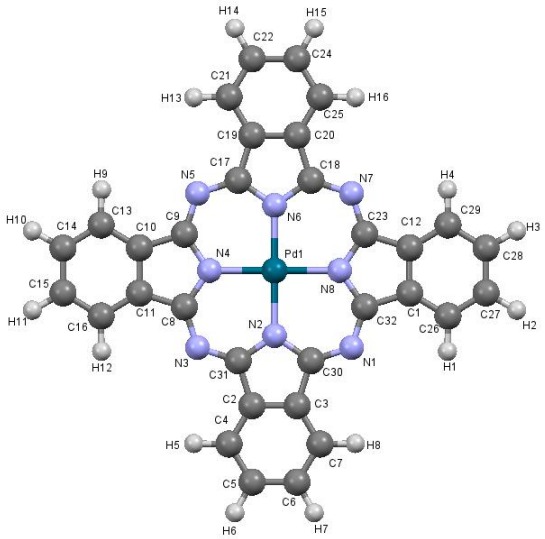

Figure 3.8: Asymmetric unit of PdPc.

Bond distance (Å)		Angles (°)		Dihedral angles	
C-H	1.1	N-Pd-N	90	C-C-C-C (b.r.)	0
N-Pd	2.02	C-C-C (b.r.)	118-121	C-C-C-N (p.r)	0
C-N (p.r.)	1.38	C-C-C (p.r.)	107	N-C-N-C	180
C-N	1.33	N-C-N	127	C-C-C-N (p.r)	0
C-C (b.r)	1.39-1.40	C-N-C (p.r.)	107	N-C-N-Pd	0
C-C (p.r)	1.46	C-N-C	127		

Table 3.3: Structural parameters obtained in the geometry optimization of PdPc.

3.1.4 Frontier orbitals study.

After the molecular optimization, the next step is the understanding of the behaviour of the Kohn-Sham orbitals for the three compounds. For this task, the study of the HOMO, LUMO, HOMO -1 and LUMO +1 has been done. The HOMO orbitals are associated to the capacity that the molecule has to lose electrons and the LUMO the capacity of accept electrons and the different behaviour of the central atom plays an important role on it.

In table 3.4 the energies of the Kohn-Sham orbitals is shown. The gap between HOMO-LUMO for the three different molecules is calculated. The molecule with the biggest gap is PdPc molecule (-1.508 eV) then ZnPc (-1.384 eV) and with the lowest gap is H_2Pc (-1.360 eV). In terms of excitation the H_2Pc has more probability to be excited at low energies than the other two molecules due to the lowest energy gap between HOMO and LUMO.

	H_2Pc	ZnPc	PdPc
HOMO -1	-6.382	-6.336	-6.176
HOMO	-5.248	-5.158	-5.295
LUMO	-3.888	-3.774	-3.787
LUMO +1	-3.831	-3.774	-3.787

Table 3.4: Energy of the Kohn-Sham orbitals for the different molecules of study.

In Fig. 3.9 - 3.11 is shown the plot of the HOMO-1, HOMO, LUMO and LUMO+1 for the three molecules. The HOMO for the three molecules is the same, and is delocalized on all the atoms presents in the π environment. An explanation for this behaviour is the high hyperconjugation present in the molecule, Zn and Pd atoms not having a big contribution because they are not involved in the aromatic π-system.

The LUMO and LUMO+1 are the same for all molecules, also they are symmetric. For ZnPc and PdPc this can be explained with the degeneration of the Kohn-Sham orbitals. A similar can be done for the H_2Pc, the difference of 0.05 eV can be taken into account as a small difference, and the high hyperconjugation plays an important role making this difference not big enough to have any difference with respect to the other molecules. The HOMO-1 for H_2Pc and ZnPc has a similar behaviour, but for the Pd shows that it has a big contribution on it changing the shape of the molecular orbital.

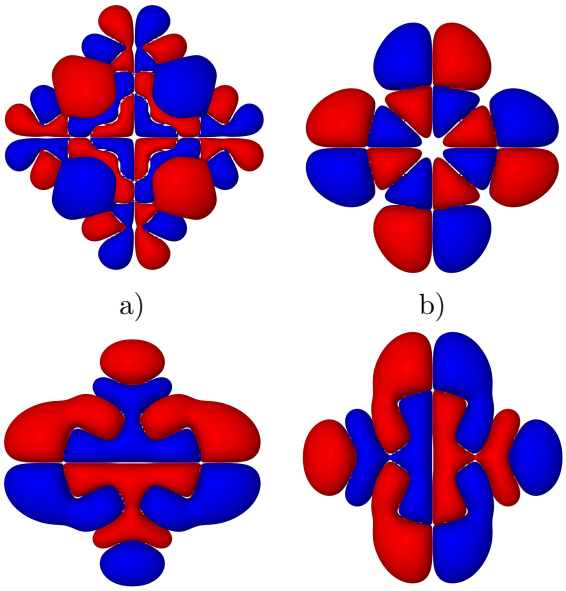

Figure 3.9: Frontier Orbitals of H_2Pc.

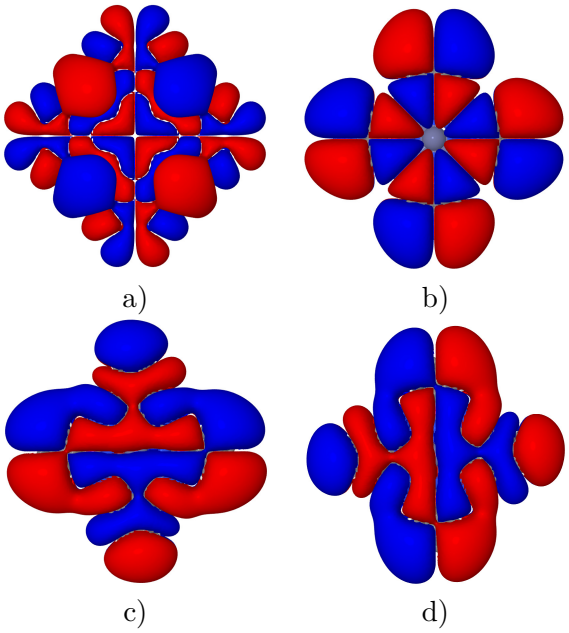

Figure 3.10: Frontier Orbitals of ZnPc.

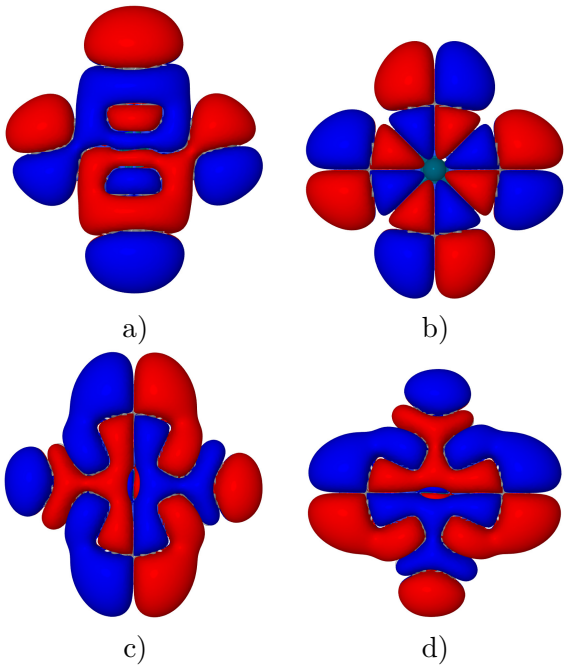

Figure 3.11: Frontier Orbitals of PdPc.

3.2 Absorption of the molecules on a metallic surface.

Experimental observation of light emission spectra by molecular nanostructures excited by the tip of a STM indicates, that in addition to the usual transitions observed with non-local excitation sources (e.g. laser) some additional peaks are observed. One of the ideas defended in this study is that some of the peaks are related to the local nature of the tunnel current. Therefore, it is possible to obtain information at the subnanometric scale by analyzing these specific peaks. However, the difficulty of the approach lies on the cohabitation of multiple different phenomena that can induce additional peaks in the optical spectra of the molecules.

In first place, the identification of the phenomena which induce the observation of these additional peaks has to be clarified. There is three possible phenomena that can generate different excitation peaks from those usually observed in gas phase with a laser as a excitation source. One of them is related to the elastic stress generated by the fact that the molecules are not isolated as when they are in gas phase but lye on substrates which may induce elastic deformations inside the molecules.

The study of this effects was carried out via the adsorption of phathalocyanine molecule on an NaCl substrate (Fig. 3.12). The NaCl surface was modeled as a mesh of 4x4 slabs along xy plane. A geometrical constraint on the atoms on the lower layers was applied. The Brillouin integration at the Γ point was used for the discretization of the Brillouin zone. The size of the mesh considered is big enough to ensure a good precision in the simulation. The adsorption energy ($E_{ad}^{MPc/NaCl}$) is described as a function of the total energy of the system ($E_T^{MPc/NaCl}$), the isolated molecule (E_T^{MPc}) and NaCl (E_T^{NaCl}):

$$E_{ad}^{MPc/NaCl} = E_T^{MPc/NaCl} - (E_T^{MPc} - E_T^{NaCl}) \tag{3.3}$$

Depending on the sign, $E_{ad}^{MPc/NaCl}$ represents the lose or gain of energy from the adsorption of the phthalocyanine on the NaCl surface. A negative value indicates a favorable adsorption on it. The position of the center of mass of the molecule was considered to be on top of an atom of chlorine and also on top of an sodium atom. Also, the determination of the barrier migration of the molecule on the surface can be considered on other positions by constraining the position in (x,y) of the metallic atom (Zn, Pd). For

each of this positions, the adsorption energy was computed for different angles (θ). It should be noted that during the simulation, no constraint was applied to the atoms of the molecule. The molecules can rotate during the optimization. The angle θ is just imposed in the initial coordinates. Whatever the configuration considered, a variation greater than 2° never was observed in the rotation angle of the relaxed molecule with respect to the initial rotation angle. Five different types of molecules were considered, CuPc, H_2Pc, MnPc,PdPc and ZnPc. For two of them (ZnPd and PdPc), we considered as a charged system.

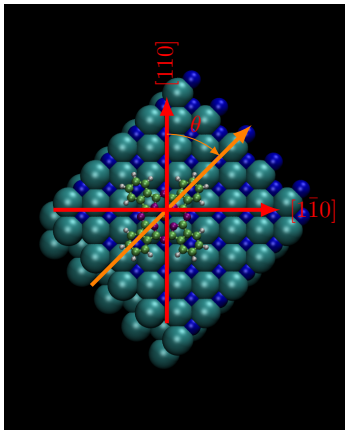

Figure 3.12: Geometry of the calculations. Angle θ is defined as the angle between the principal axis of the molecule and the [110] atomic direction of the NaCl substrate.

Several observations can be extracted from the examination of the adsorption energies as a function of the orientation of the molecule on NaCl (Fig. 3.13). Firstly, the chemical nature of the most stable adsorption site depends on the chemical nature of the metal. The ZnPc and MnPc on top of a chlorine atom is more stable than on the sodium. In the other hand, PdPc and H_2Pc are more stables on top of a sodium atom. For CuPc, the difference between both adsorption sites is around +0.70 meV less stable in chlorine site and is in good agreement with the experimental results obtained by Ullmann *et al* [147]. In Fig. 3.14 the minimal adsorption energies for considered molecules is shown. The sodium adsorption place is independent of the atom nature located in the center of the phthalocyanine since the energy only varies by 70 meV switching from ZnPc to PdPc. On the other hand, the variation is much greater when the chlorine site is consider for the adsorption. In this case a variation around 1.2 eV is obtained switching from PdPc to MnPc.

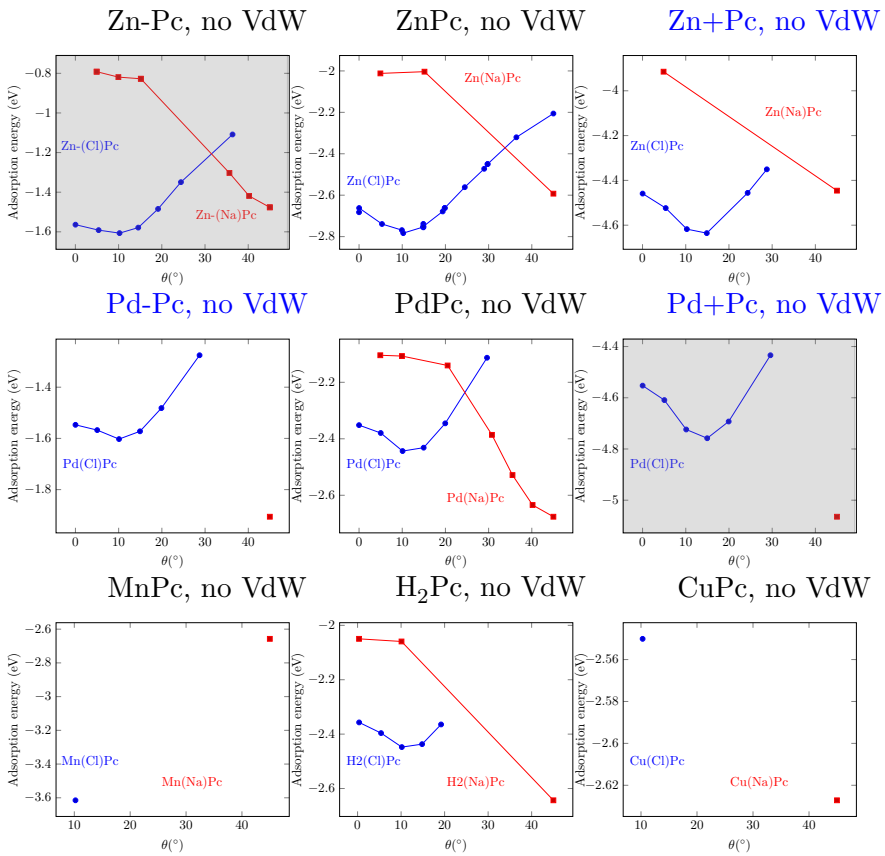

Figure 3.13: Adsorption energies of MPc/NaCl for charged and neutral molecules on the surface with different orientations and different 'on-top' adsorption sites; M=Zn, Pd. Figures with grey background correspond to configurations which are not observed experimentally.

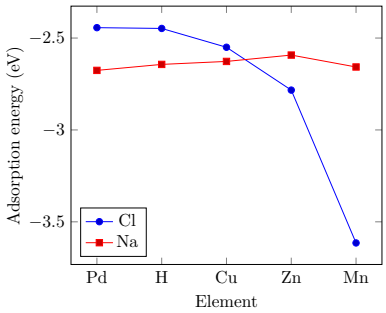

Figure 3.14: Adsorption energy as a function of the metallic atom in the center of phthalocyanine and of the adsorption site (in red sodium and blue chlorine.)

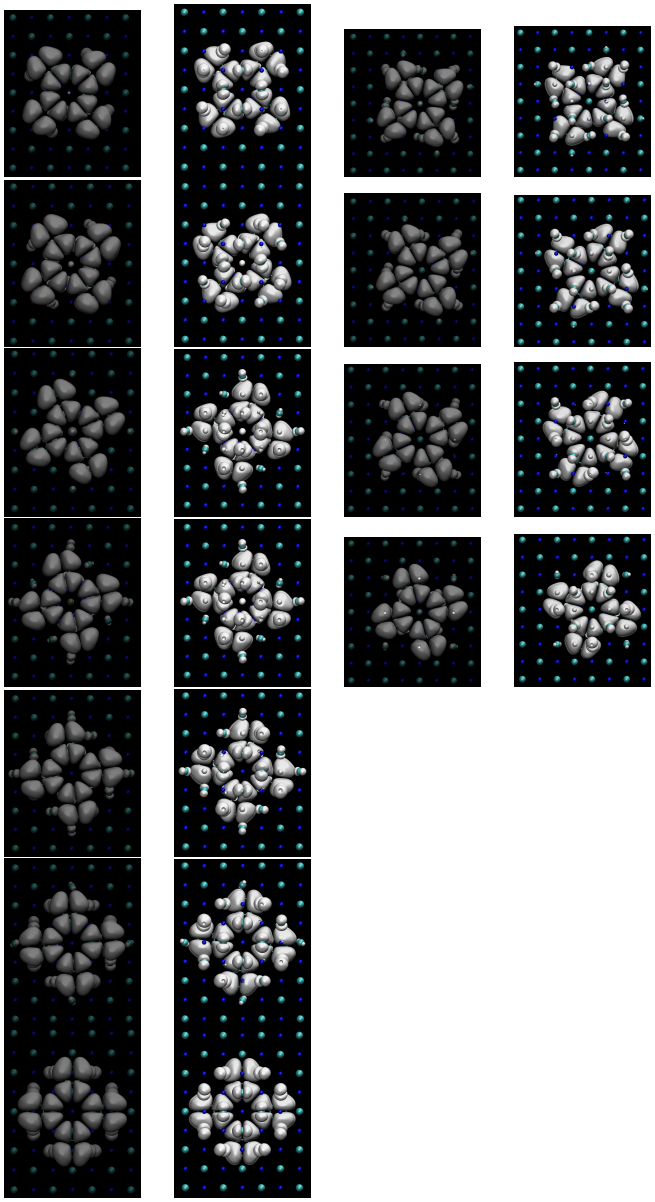

Figure 3.15: Total electronic density contribution of the HOMO for PdPc (isosurface 2×10^{-5}) adsorbed onto a sodium atom. ((a) Top view, (b) the point of view from the observer on a chlorine atom.

The contribution of the charge density to the HOMO of the PdPc molecule is shown in Fig. 3.15. A clear assumption can be made, whatever the site of adsorption, there is a delocalization of the HOMO from the molecule onto the

chlorine atoms on the surface. The delocalization is much important when the PdPc is adsorbed on sodium site (Fig. 3.15 a-b) than when is adsorbed on a chlorine site (Fig. 3.15 c-d). Therefore, the adsorption of PdPc is ensure via the interaction between the nitrogen, carbon and hydrogen atoms of the molecule with the chlorine atoms on the surface. In contrast, interactions with sodium atoms do not seem (or a few) to be involved in the adsorption. The deformation analysis of the molecule for different angles and for the two adsorption sites does not show significant changes. Besides, the optical spectra were computed within the framework of the linear response theory. It should be noted that the calculation of the optical spectra was not done on the whole system but only on the optimized symmetry. As for deformations, any marked differences were found between different conformations (angles and adsorption sites). The appearance of additional excitation peaks from a structural origin is unlikely to happen.

3.3 Effect of a constraint in a phthalocyanine molecule.

Benjamin Doppagne et al. [42] were able to describe a tautomerization process of the free phthalocyanine (H_2Pc) with a scanning tunneling microscope experiment combined with fluorescence spectroscopy [148–151] deposited on a NaCl-covered Ag(111) sample. STM-induced fluorescence (STM-F) spectra exhibit duplicate features that can be assigned to the emission of the two molecular tautomers (Fig. 3.17). In Fig. 3.16 the experimental and DFT calculated images of the HOMO and LUMO of H_2Pc are shown. A good description of the HOMO and LUMO can be done from a theoretical point of view. A differential conductance (dI/dV) spectrum recorded on H_2Pc molecule reveals the energy position of the highest occupied and lowest unoccupied molecular orbitals ($E_{HOMO} \approx$ -2.5 eV and $E_{LUMO} \approx$ 0.55 eV).

This assignment was confirmed by STM images recorded at the energies of the two spectral contributions. The LUMO may exhibit two similar twofold symmetry patterns, rotated by 90°, which can be assigned to the two different tautomers. The HOMO, however, always reveals the same fourfold symmetry image. However, to explain the tautomerization process, the molecule is perturbed locally in three different regions (Fig. 3.17-e) giving different STM-F spectra (Fig. 3.17-f). The spectrum for the perturbation in the position 1 shows an intense peak at 1.80 eV, a weaker peak at 1.92 eV and a series of very weak vibronic features on the low energy side of the main peaks. The peaks at 1.80 eV and 1.92 eV can be assigned to the two first optical transitions of H_2Pc molecule named Q_x and Q_y, respectively. Q_x and Q_y correspond to transition dipole moments oriented along and perpendicularly, respectively, to the two inner hydrogen atoms of H_2Pc. The

spectrum acquired on the same molecule in position 3 (Fig. 1f) shows a very similar spectral structure, but with a 20 meV shift of the Q_x peak to higher energies.

Eventually, the spectrum for position 2 acquired in-between two benzopyrrole units of the H_2Pc molecule shows that this shift results from a duplication of the main spectral feature. The presence or absence of duplicate features in the spectra results from minute changes in the environment of the H_2Pc molecules caused by their adsorption on different sites of the NaCl/Ag(111) Moiré pattern [152].

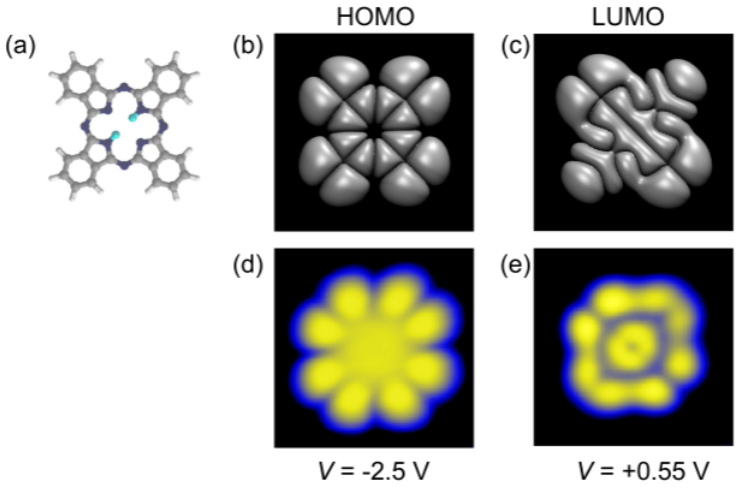

Figure 3.16: a) Chemical structure of H_2Pc used in DFT calculations. b) homo and c) LUMO computed in DFT and d) e) experimental STM images (3x3 nm^2, I=10 pA)

The STM-F spectra acquired perturbing in different regions of the molecule has revealed different energy gap between the $Q_{x1} - Q_{x2}$ peaks. The effect can be illustrated using the Fig. 3.18. Three characteristic STM-F spectra have been acquired on the three H_2Pc molecules labelled type 1, 2 and 3. Type 1 molecule exhibits nearly no splitting, while the spectra labelled type 2 and 3 show clear a duplication of the Q_x contribution, with a small (type 2) or a large (type 3) separation.

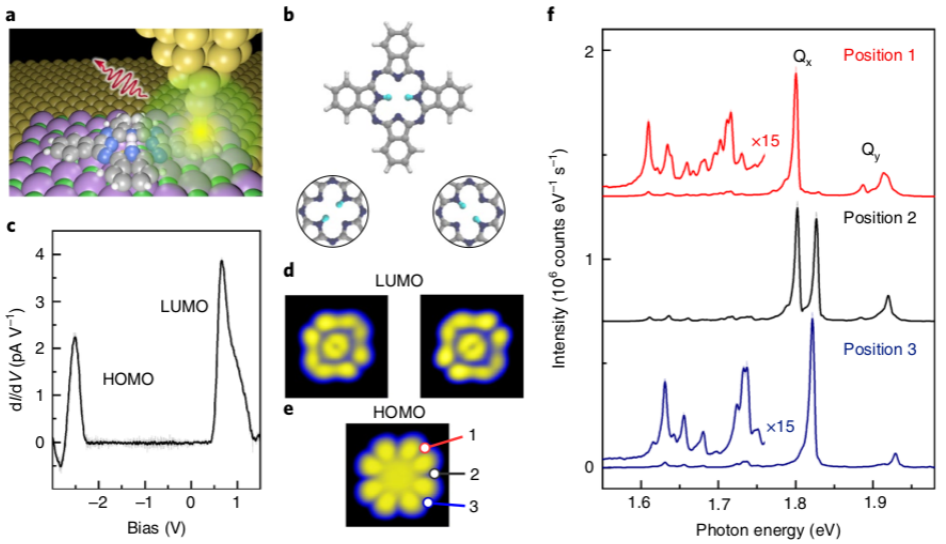

Figure 3.17: STM-F spectroscopy of individual H_2Pc molecules. a) Sketch of the STM-induced emission experiment. b) Ball-and-stick model of the free-base phthalocyanine and zoom on the central part of the molecule to highlight the structure of the two tautomers. c) dI/dV spectrum acquired on a single H_2Pc adsorbed on three layers of NaCl on Ag(111). d) and e) STM images (3 x 3 nm^2 , I = 10 pA) acquired at V = 0.55 V (d) and V = -2.5 V (e). Two patterns tilted by 90° from each other can be observed in the image of a same molecule recorded at V = 0.55 V (d) and correspond to the two tautomers. f) STM-F spectra acquired (V = -2.5 V, I = 100 pA, acquisition time t = 120 s) for the STM tip located at the positions identified in e.

A clearly assumption is that the differences comes from the adsorption site of the different molecules. With the image in Fig. 3.18-c it is possible to determine the adsorption site of the H_2Pc molecules with atomic-scale precision. Independently of the H_2Pc type, the molecules are absorbed on Na top sites with the H_2Pc axis oriented along [100] and [010] directions of the NaCl (001) layer [153] suggesting that the adsorption site is not responsible for the different types of STM-F spectra reported in Fig. 3.18-a.

To emit at different energies, the two tautomers, which are otherwise equivalent, must experience slightly different environments [154, 155]. This is confirmed by the substantially different Q_x-Q_y gaps of the two tautomers. This assumption can be supported by time-dependent density functional theory for an artificial compression (tension) of 5% (10%) of the molecule size along the Q_x axis (Q_y axis).

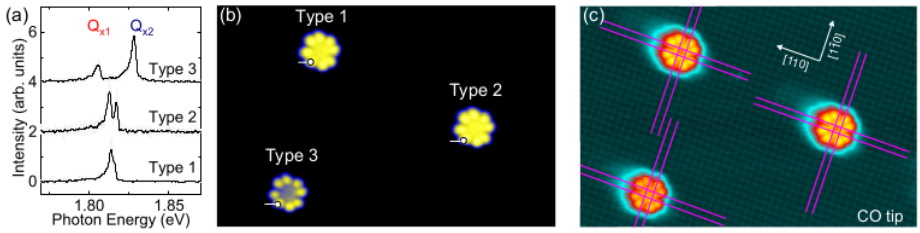

Figure 3.18: STM-F spectra acquired at V = -2.5 V, I = 200 pA, acquisition time t = 300 s for the three different H_2Pc molecules. STM images (20 x 14.2 nm 2 , V = -2.5 V) of the three type of H_2Pc molecules with (b) a silver terminated tip and (c) a CO terminated tip. The blue lines in (c) are aligned with chlorine atomic rows.

The structural relaxation calculations were carried out using the same procedure as in Section 3.1.3. Two strain directions for the molecule were computed Fig. 3.19. Strained molecules were obtained from the relaxed configuration by applying a strain tensor, ϵ, in the required directions:

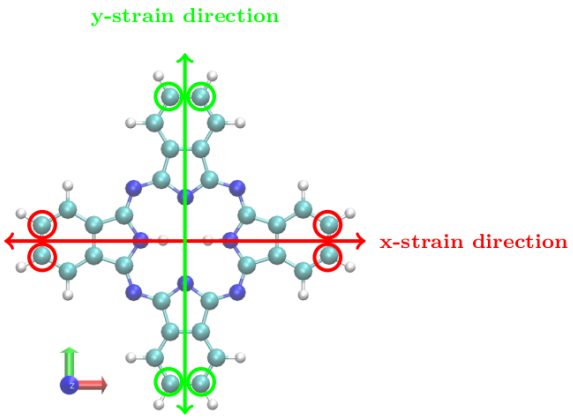

Figure 3.19: Scheme of the strained directions considered. The circles indicate the constraint atoms during the structural relaxation calculations.

$$\omega = \begin{pmatrix} \epsilon_{xx} & 0 & 0 \\ 0 & \epsilon_{yy} & 0 \\ 0 & 0 & \epsilon_{zz} \end{pmatrix}.$$

In the geometry optimization some atoms of the molecule are constrained in order to preserve the strain direction. Theoretical optical spectra of the H_2Pc molecule for different strain configurations were computed by resorting to Peterliska's formalism for compute the neutral excitations in finite systems [59]. This scheme provides a way to access to the electronic density response to an external potential required to compute the optical spectra. the full interacting linear density response is given by

$$\rho(r,\omega) = \int dr' \chi_{ks}(r,r',\omega) V_{ks}(r'\omega). \tag{3.4}$$

The excitation energies as well as the couples of occupied/virtual ground state Kohn-Sham orbitals involved in the transitions can be determined as solution of the non-Hermitian eigenvalues problem (Section 2.7):

$$\begin{pmatrix} L & K \\ K^* & L^* \end{pmatrix} \begin{pmatrix} X \\ Y \end{pmatrix} = \omega \begin{pmatrix} -1 & 0 \\ 0 & 1 \end{pmatrix} \begin{pmatrix} X \\ Y \end{pmatrix}.$$

93 occupied states and 100 virtual states where used in the TD-DFT simulation, with a gap of 5 eV between the HUMO and the LUMO. Also five molecular configurations were computed and the optical characteristics are displayed in Table-3.5 and Fig. 3.20.

Configuration	Transition				δQ(meV)
	Q_x		Q_y		
	Energy(eV)	Oscillator stength	Energy(eV)	Oscillator stength	
ϵ_{xx}=ϵ_{yy}=1.00(free)	2.10	0.26	2.18	0.36	80
ϵ_{xx}=0.95,ϵ_{yy}=1.00	2.10	0.26	2.18	0.36	80
ϵ_{xx}=1.00,ϵ_{yy}=0.95	2.13	0.29	2.17	0.31	40
ϵ_{xx}=1.10,ϵ_{yy}=1.00	2.03	0.29	2.06	0.33	30
ϵ_{xx}=1.00,ϵ_{yy}=1.10	2.03	0.19	2.12	0.39	90

Table 3.5: Energy transitions according to the strain of H_2Pc. $\Delta Q = E_{Q_y} - E_{Q_x}$.

Depending on the strain applied on the molecule, different behaviours are observed compared to the free configuration. A reduction of the ΔQ gap when a tension is applied along the Q_x axis or a compression along the Q_y one. When a compression is applied an increase of the gap is observed along Q_x or a tension along the Q_y one. This behaviour is similar to the evolution of ΔQ gap reported in the experiment carried out in Benjamin Doppagne et al. [42] between the unstrained tautomer 2 and tautomer 1 (Fig-3.21.)

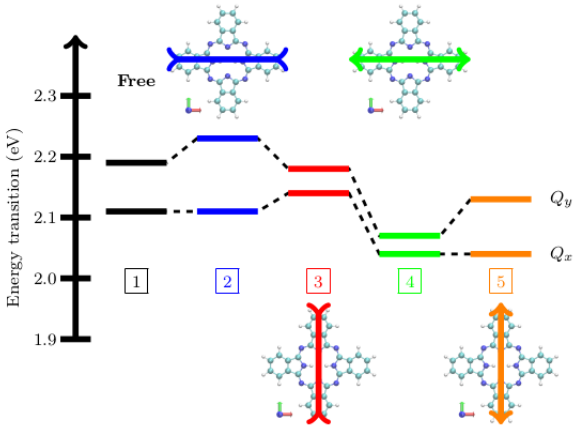

Figure 3.20: Energy transition diagram according the strain of H_2Pc

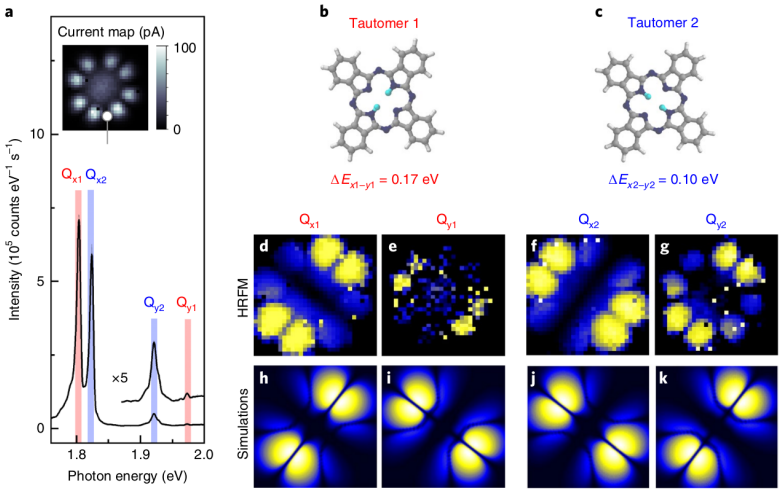

Figure 3.21: Highly resolved fluorescence mapping of a single H_2Pc molecule. a, STM-F spectrum (V = -2.5 V, I = 100 pA, acquisition time t = 180 s) acquired at the position marked by a white disk in the current image (2.5x2.5 nm^2 , V = -2.5 V) in the inset. **b**–**k**, The chemical structure of tautomers 1 (b) and 2 (c) from the associated HRFMs (**d**–**g**) (2.5x2.5 nm^2, acquired simultaneously with the current map in a, acquisition time t = 50 s pixel^{-1} , 30x30 pixels), and from their related simulated maps for the main contributions (Q_{x1}, Q_{x2}, Q_{y1} and Q_{y2}) (**h**–**k**) identified in **a**. Photon energy integration intervals were $1.798 < h\nu < 1.811$ eV (d), $1.972 < h\nu < 1.981$ eV (e), $1.824 < h\nu < 1.832$ eV (f) and $1.923 < h\nu < 1.941$ eV (g).

The emission of two tautomers is confirmed by the different ΔQ gaps of he two tautomers. This gap is larger for tautomer 1 than for tautomer 2. It can be easily explained due to the different dipolar moment of the tautomers. This coupling results in an increased (attenuated) emission intensity for the tip localized at the extremities (center) of the molecular dipoles. In our case, the extreme spatial localization of the field is responsible for the close to atomic-scale spatial resolution in the fluorescence maps. The excellent agreement between experimental and theoretical maps suggests that two series of Q_x and Q_y contributions correspond to the two tautomers of the H_2Pc molecules.

3.4 (LR)TD-DFT optical spectra for H_2Pc, ZnPc and PdPc

The electronic transitions are computed under the framework of the Time Dependent-Density Functional Theory (TD-DFT). Octopus code perform the time-propagation of electron orbitals and also the linear-response theory (Casida's method). In this section a discussion of the optical spectra computed under the Casida's approach. Which yields quantum mechanically under the plasmonic response [156–160].

In linear response regime, it is often formulated in frequency space [57, 59, 161] in terms of the Casida matrix expressed in the Kohn-Sham electron-hole space. Casida's formulation allows calculations of the excitation energies of a finite system. Normally, this method is the fastest one. The Casida's equation is a pseudo-eigenvalue problem written in the basis of particle-hole states. Indeed, a set of occupied and unoccupied orbitals has to be computed. The transition dipolar moment are computed using the dipolar moment along x, y and z direction:

$$\begin{aligned} < x > &= < \Psi_0 | x | \Psi_{ex} > \\ < y > &= < \Psi_0 | y | \Psi_{ex} > \\ < z > &= < \Psi_0 | z | \Psi_{ex} > \end{aligned} \tag{3.5}$$

where Ψ_0 is ground state wavefunction and Ψ_{ex} the wavefunction of a given excited state. An other important physical variable is the oscillator strength given as the average over the three directions:

$$f_{ex} = \frac{2m_e}{3\hbar^2}\omega_{ex}| < \Psi_0 | r | \Psi_{ex} > |^2. \tag{3.6}$$

The optical spectrum can be given as the strength function:

$$S(\omega) = \sum_{ex} f_{ex}\delta(\omega - \omega_{ex}). \tag{3.7}$$

The calculations are commonly performed by diagonalizing the Casida matrix directly or by solving the equivalent problem with different iterative subspace algorithms [58, 162–164]. The Casida approach directly enables a decomposition of the electronic excitations into the underlying Kohn-Sham electron-hole transitions and the results are often limited to absorption spectra or the analysis of induced densities or fields.

The goal of this section is the analysis of the optical response of the H_2Pc, ZnPc and PdPc molecules. These characteristic conjugated molecules have a well-defined $\pi - \pi^*$ transitions that exhibit a systematic red-shift as the extent of the conjugated π-system increase [165].

3.4.1 Virtual states convergence.

A previous test before the computation of the photoabsorption spectra shall be done as spacing and radius parametrization. The simple single orbital excitation structure (transition from an occupied orbital to one virtual orbital), which is characteristic for the exact Kohn–Sham orbitals and which is of great importance for the correct interpretation of the nature of the excited states. In Fig.3.22 is shown the evolution of the number of virtual states as a function of the lowest energy levels. As in the case of radius, depending of the molecule, different behaviour is obtained.

The convergence with respect to excitation energy indicates that a number of states higher than 70 seems converged for ZnPc and H_2Pc but not for PdPc. However, independently of the molecule, for the dipolar moment transition and oscillator strength seems converged at 70 virtual states. In terms of the optical transitions a spacing of 0.14 Å and a radius of 5.0 Å is enough. On the other hand, at least 70 virtual states should be taken into account to perform the Casida's approach to obtain the photoabsorption spectra.

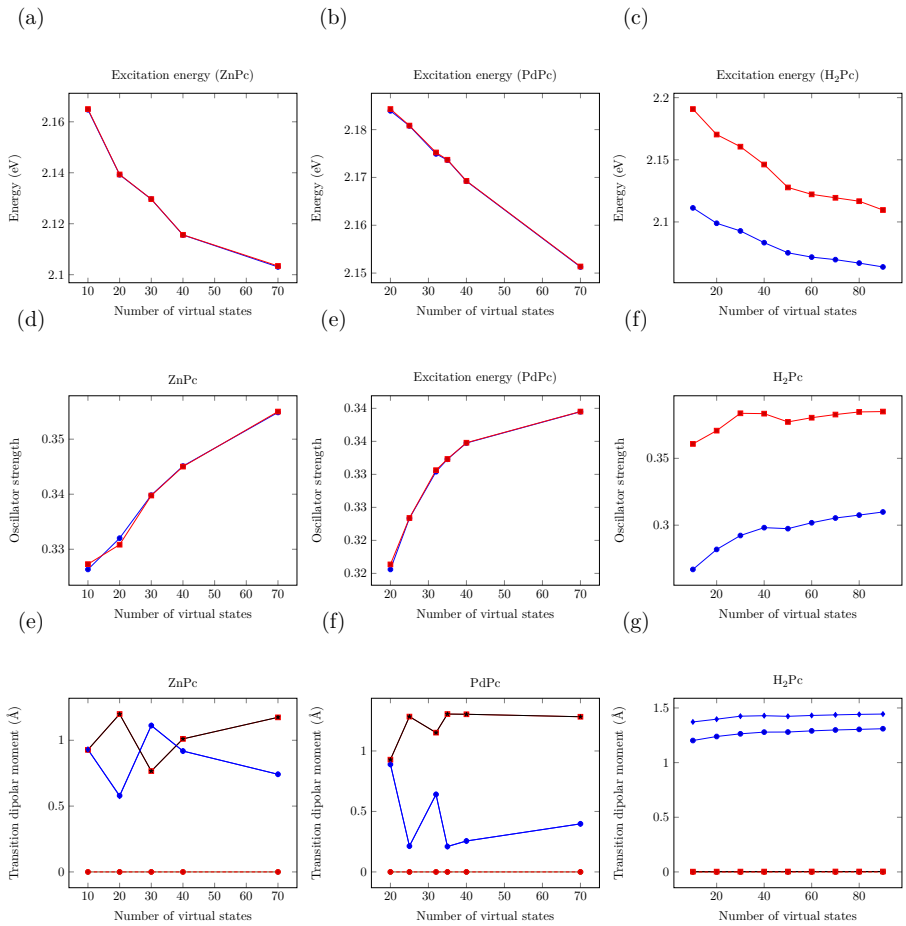

Figure 3.22: Evolution of the excitation energy as a function of the virtual states behind the Casida's approach. The results were obtained with a radius of 6.5 Å and a spacing of 0.14 Å.

3.4.2 Photoabsorption spectra in the Casida's approach.

The calculated photoabsorption spectra of the molecules are shown in Fig. 3.23. In Tables A.1, A.2 A.3 the Kohn-Sham decomposition of these excitations is shown as described by the components of the normalized Casida eigenvectors normalized to 1 for each excitation ($\sum F^2 = 1$). The response of each of the molecules is dominated by a set of transitions,the predominant being the HOMO-LUMO for all molecules. In the case of H_2Pc this excitation shows two peaks, the Q_x and Q_y which appears at 2.05 eV and 2.14 eV, respectively. ZnPc fundamental transition is located at 2.09 eV. This excitation is degenerated due to the degeneracy of the LUMO. Table A.2 indicates that the transitions have the same casida eigenvector value and

are from the orbital 93 (HOMO), the orbitals 94 and 95 (LUMO) being the orbitals which compose the LUMO. Therefore, the same situation is shown for the PdPc molecule, the HOMO-LUMO transitions involving the orbitals 97 (HOMO) and 98-99 (LUMO). The excitation energy in this case is 2.19 eV. This excitation have others contributions of different transitions but they much less predominant than the HOMO-LUMO with a Casida eigenvector close to the unity due to the normalization. A fully description of the spectra is done in Appendix-A

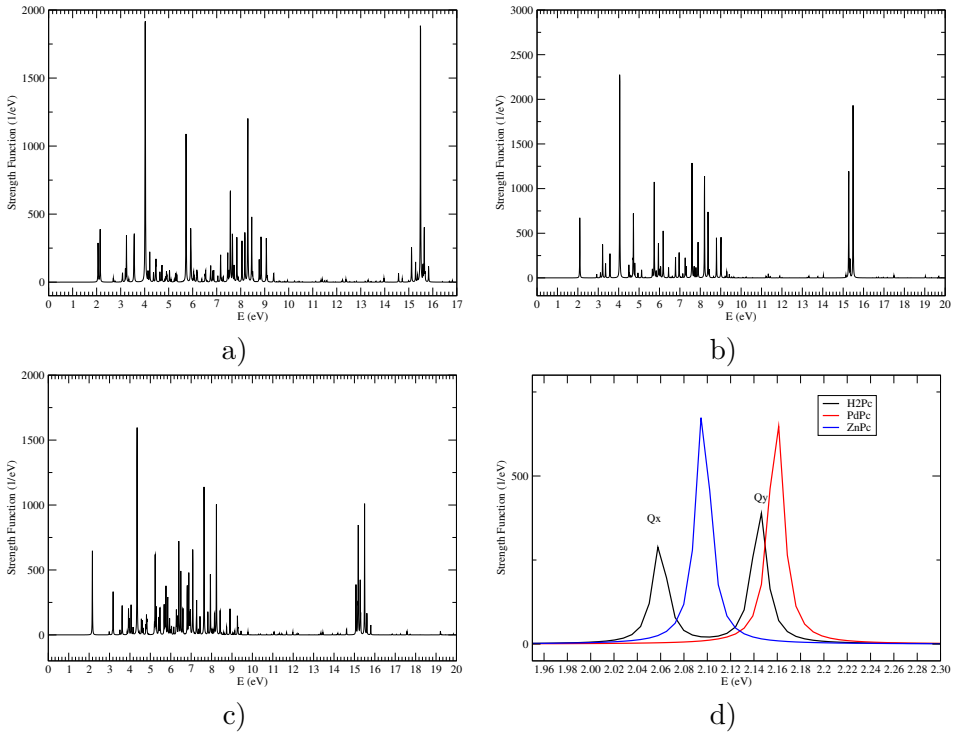

Figure 3.23: Photo-absorption spectra of a) H_2Pc, b) ZnPc, c) PdPc and d) comparison of all the spectra.

The energy comparison of the optical transitions computed theoretically indicates a good agreement with the experimental results. The order H_2Pc < ZnPc < PdPc is the same in both cases. On the other hand, from a qualitative point of view this agreement shows a difference around 200 to 300 meV in energy. A higher value is obtained with the linear response method (Table 3.6).

		Exp.	Calcul	Shift (Calc.-Exp.)
4	PdPc Q_{Pd}	1.925 ($\Delta_{3-4}^{exp} = 3$ meV)	2.169 ($\Delta_{3-4}^{calc} = 26$ meV)	+244 meV
3	H_2Pc Q_y	1.922 ($\Delta_{2-3}^{exp} = 23$ meV)	2.143 ($\Delta_{2-3}^{calc} = 53$ meV)	+ 221 meV
2	ZnPc Q_{Zn}	1.899 ($\Delta_{1-2}^{exp} = 89$ meV)	2.090 ($\Delta_{1-2}^{calc} = 23$ meV)	+191 meV
1	H_2Pc Q_x	1.810	2.067	+257 meV

Table 3.6: Energies of the optical transitions in MPc.

A review on the bibliography of the excitation energies measured for the ZnPc molecule under different conditions indicate values between 1.85 and 1.95 eV (Table 3.7). The calculations, carried out according to several different methods, indicate values lying rather around 2.0 to 2.10 eV, in accordance with the values we have determined.

Experimental conditions	Excitation energy (eV)	Oscillator strength
Exp. in THF	1.86[166]	
Exp. gas	1.88[167]	0.40[168]
Exp. in Ar matrix	1.89[169]	
Exp. in DMSO	1.85[170]	
Exp. in gas-phase supersonic jet	1.95[171]	
Functional	Excitation (eV)	Oscillator strength
M11	1.88[166]	
M06	2.02[172]	
CAM-B3LYP	2.04[172]	
BHLYP	2.06[172]	
B3LYP	2.08[173], 2.09[166, 172]	
BHandHLYP	2.10[173]	
LDA-PZ	2.103 (This work)	0.355 (This work)
GGA-PBE0	2.12[166, 173], 2.13[166]	

Table 3.7: Excitation energies of ZnPc.

3.5 Conclusions.

In this chapter the parametrization study was carried out. The principal simulation parameters were optimized, the optimal spacing for the ground state simulations is 0.16 Å for all molecules and 4.5 Å for the radius. With this parameters a geometry optimization was made to obtain the initial molecular configuration. The results are in good agreement with the experimental values. Also the study of the frontier orbitals was carried out in order to obtain the theoretical values to understand the behaviour of the Kohn-Sham orbitals. This study reveals a degeneracy on the LUMO for ZnPc and PdPc meanwhile for the H_2Pc a single orbital is obtained. The phenomena of a "extra" peaks in the optical spectra was taken into account in the study of

the absorption of the molecules in a metallic surface on NaCl. A mesh of 4 × 4 slabs of NaCl was considered and also a deeply study of the disposition of the molecule onto the surface. The observations that can be extracted, from the examination of the adsorption energy due to the angle of the molecule with respect to the surface, are that ZnPc molecule is more stable on the chlorine atoms than on sodium atoms. On the other hand, the PdPc and H_2Pc are more stable on sodium atoms than on chlorine atoms.

The constraint applied on the molecule reveals a energy change in the Q_x and Q_y transitions. With this energy changes we are able to justify from the linear response theory the tautomerization process that happens when the H_2Pc molecule is locally perturbed for the STM tip. The last section of the chapter is devoted to the theoretical study behind the linear response theory of the photoabsorption spectra for the molecules of study. The results obtained reveal a energy shift between theory and experiment around 200-300 meV. This error is considered as acceptable between theory and experiment. The convergence of the total energy respect to the number of virtual states considered in the simulations reveals that at least 70 virtual states should be considered in the simulation to a full convergence of the optical spectra. However, the limitation of the computational resources in terms of RAM memory and simulation time has to be taken into account.

Chapter 4

Real-Time Time-Dependent Density Functional Theory study.

The real-time propagation formulation [98, 174] is computationally efficient [175, 176]. A natural way to carry out a Kohn-Sham decomposition is to consider the full time-dependent Kohn-Sham density matrix in the Kohn-Sham electron-hole space [177, 178]. Other possibilities are to fit the Kohn-Sham transitions densities to induce densities [179], to consider time-dependent transition coefficients [180–182] or to analyze occupational numbers [183–185]. The analysis of the Kohn-Sham transition coefficients relies on the linear-response TDDFT approach, and a complementary information can be obtained from the analyses of the contributions [186–188].

The photoabsorption spectra for finite systems is computed using the photoabsorption cross section, which is proportional to the imaginary part of the dynamic polarizability (Eq. 2.61).

$$\sigma(\omega) = \frac{4\pi\omega}{c}\frac{1}{3}\Im\sum_{\gamma} -\int d^3r \int d^3r' r_\gamma \sum_{\sigma\sigma}\chi_{\sigma\sigma}(r,r',\omega)r'_\gamma,, \tag{4.1}$$

where c denotes the speed of light and γ=x,y,z. The function χ is also called the linear response function of the system. It measures the change of the density when the system is perturbed by an infinitesimal change Eq. 4.2 of the external potential:

$$\delta\rho_\sigma(r,\omega) = \sum_{\sigma'}\int d^3r' \chi_{\sigma\sigma'}(r,r',\omega)\delta V_{ext\sigma'}(r'\omega). \tag{4.2}$$

The procedure of the photoabsorption spectrum calculation consists in the application a perturbation of the form $\delta V_{ext\sigma}(r,t) = -\kappa_0 r_\nu \delta(t)$ on the ground state Kohn-Sham wavefunction ($\phi_{j\sigma}(r)$) of the system. The amplitude κ_0 should be small in order to keep the response of the linear system. The perturbation applied excites all frequencies of the system with equal weight. At t=0 the Kohn-Sham orbitals are defined as:

$$\phi_{j\sigma}(r, t = 0) = e^{i\kappa_0 r_\gamma} \phi_{j,\sigma}(r). \tag{4.3}$$

These orbitals are further propagated for a finite system and the dynamical polarizability can be obtained from:

$$\alpha_\gamma(\omega) = -\frac{1}{\kappa_0} \int d^3 r r_\gamma \delta\rho(r, \omega). \tag{4.4}$$

The photoabsorption spectra is obtained from the Fast Fourier transform of the dynamical polarizability. Several experimental techniques can be used to extract the optical spectra of nanostructures, such as near-field optical microscopy, photoelectron microscopy, scanning tunnelling microscopy or photoluminescence. In this chapter, a detailed description of the photoabsorption spectra computed in real-time time-dependent density functional is given. The first section is focused in the molecule under the action of an electric field, which perturbs the molecule along x,y,z. In the second section a scalar potential was used as local source of excitation over the molecules along x,y,z. The third section is devoted to the study of the energy transfer able to excitate a second molecule. It should be noticed that the accuracy in reproducing transitions of intermediate energy is known to be deteriorated, due to the wrong asymptotic behaviour of the LDA exchange-correlation potential. For this reason, the analysis is focused on the lowest energy peaks of the photoabsorption spectra.

4.1 Photoabsorption spectra of the molecules.

The real space propagation under the TD-DFT approach gives information to obtain a clear physical image of the wavefunction, which is not possible to obtain when the wavefunctions are expanded in terms of explicit basis sets. The optical spectra in the framework of the explicit time-propagation technique [98, 100] implemented in Octopus code will be discussed in this section.

A regular real-space grid was chosen under the LDA approximation using the Perdew-Zunger functional to describe the exchange-correlation effects. The electron-ion interaction is described with the Troullier-Martins non-relativistic non-local norm-conserving pseudopotentials [44]. To calculate non-linear optical properties of the molecules of study, the optimised geometries obtained in Section-3.1.3 were used.

The evolution of the system under the influence of a laser field behind the dipole approximation requires a parametrization. The most important parameters to be set are the time step and the maximum of steps of the simulation. The first parameter set was Δt and the second was the number of iterations. In this simulation the propagation length is t= 0.5/eV and the time step length is dt = 0.002/eV. The total simulation time is given by $\frac{t}{\Delta t}$ and is 400/eV making 200.000 the total number of steps for all molecules. In absence of perturbation the total energy of the system should be constant and it is a method to check that the time step chosen is a reasonable one. The approximation of the propagator used is the exponential midpoint rule which is one of the most simplest methods. This approach preserves the reversal symmetry and is defined as:

$$U_{EM}(t\delta t, t) = exp(-i\delta t H_{t,\delta t/2}). \tag{4.5}$$

The exponential of the Hamiltonian (a core part of the full algorithm used to approximate the evolution operator) is computed using the Lanczos method [189]. The time-dependent external perturbation applied on the system in the form $f(x,y,z)cos(\omega t + \phi(t))g(t)$, where f(x,y,z) is defined by a electric field, $\omega = 3$eV. The amplitude of the envelope function, g(t), is A=1 eV/Å. The type of time dependent function, f(x,y,z), used in this study is the tdf-cosinoidal variable defined as:

$$f(t) = F_0 cos\left(\frac{\pi}{2}\frac{t - 2\tau_0 - t_0}{\tau_0}\right). \tag{4.6}$$

If $|t - t_0|$ τ_0, then f(t)=0.

From the value of $\delta\rho(r,\omega)$ it is possible to calculate the induced dipole moment through the dynamical polarizability. The light absorption can be viewed as a dissipation process induced by the electronic excitation. As a consequence, the infinitesimal change in the density leads to an imaginary part and by applying the Fermi's Golden rule the photoabsorption cross section is obtained. Therefore, another widely used quantity is the strength function $S(\omega)$, which is connected to $\alpha(\omega)$ by:

$$S(\omega) = \frac{2m}{\hbar^2}\sum_n \delta(\omega-\omega_n)|\left\langle\rho\right|\hat{Q}\left|\rho_0\right\rangle|^2 = \frac{2m\Im\alpha(\omega)}{\pi\hbar^2}. \tag{4.7}$$

In real-time propagation, the expected value is simply expressed in the Schrödinger equation using the electronic wavefunction $\Psi(t)$ on the system at time t. As a consequence of the time dependence of the propagator, the electronic density has to be interpolated for Δt self consistently but there is an ongoing debate whether the additional computational cost worth the gained precision of the simulation [190, 191]. Also the matrix exponents needed for the propagation have to be approximated as well by series expansions or subspace algorithms. This errors can be decreased by the efficiency method of the propagator. In the same way as the functional development in DFT, the development of a precise and low cost computational propagator is under study [192, 193].

4.1.1 H_2Pc photoabsorption spectra.

The photoabsorption spectra was obtained by the propagation of the perturbation along x, y and z in three independent runs. Using the post-production subroutine oct-propagation_spectrum implemented in octopus the cross-section-tensor is obtained. In Fig. 4.1 the dipolar moment variation and the Fourier transform of the dipolar moment for H_2Pc is shown.

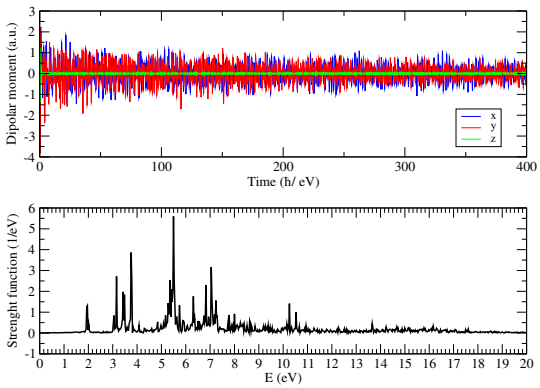

Figure 4.1: On the top is the dipolar moment variation due to the perturbation applied and on the bottom the photoabsorption spectra is shown for H_2Pc.

The plot on the top is the dipolar moment variation for the simulation run of 200.000 steps with a time step of 0.002 1/eV and a total simulation time of 400 1/eV. The Fast Fourier Transform of the dipolar moment variation gives the photoabsorption cross section spectra in a real time propagation simulation with a post-production spectrum energy step of 0.0001 eV. Considering the fundamental transition and comparing it with the experimental spectra (Fig. 4.2), we observe that the Q_x is split in two bands at 1.93 and 1.96 eV, with respect to the experimental spectra, and that the Q_y band appears at 2.00 eV. There is a energy shift about 0.15 eV for the Q_x band and 0.1 eV for the Q_y.

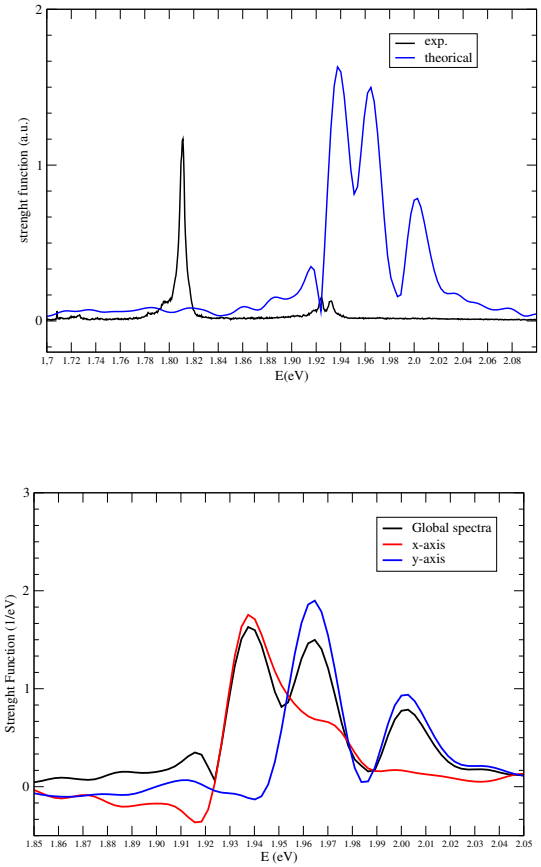

Figure 4.2: On the top, the comparison between the experimental spectra and the spectra obtained with (RT)-TDDFT approach. At the bottom, the theoretical spectra of the fundamental transition comparing the cross-section-tensor spectra with the cross-section-vector along x and y with a energy resolution of 0.0001 eV.

From RT-TDDFT the splitting observed in the Q_x band for H_2Pc is a consequence of the action of the perturbation of the system along each spatial direction. There is a shift in the Q_x band depending on the direction of the perturbation (Fig. 3.16). When the molecule is perturbed along x only the Q_x band appears. Meanwhile the perturbation along y the Q_x and Q_y are obtained. The explanation for this phenomena can be described as the different environment the molecule has due to the D_2h symmetry, the inner Hydrogens are contained in the x-axis, it means when the perturbation is along that direction the main component of the dipolar moment is along x direction. In the other hand, when the molecule is perturbed along y the action on the two inner Hydrogens perpendicular to the perturbation applied makes the global dipolar moment have a x component on it. The consequence of the action of the perturbation on them when it is propagated along y direction is a shift in energy on the Q_x band. To Conclude, a reduction of the gap ΔQ is observed along y-axis, and comparing it with the experiment, this behaviour is a consequence of the different components of the dipolar moment.

A comparison between the (LR)-TDDFT and (RT)-TDDFT photoabsorption spectra is shown in Fig. 4.3. The generation of the harmonics of the dipolar moment generate more peaks than expected in linear response approach. Despite of it, both methods are in good agreement with respect to the experimental results. The experimental Q band is located at 1.82 eV, meanwhile for RT-TDDFT is located at 1.93 eV and at 2.1 eV for LR-TDDFT method. In the other hand, the experimental B band is located at 3.73 eV, 3.73 for RT-TDDFT and 4.02 eV for LR-TDDFT [194].

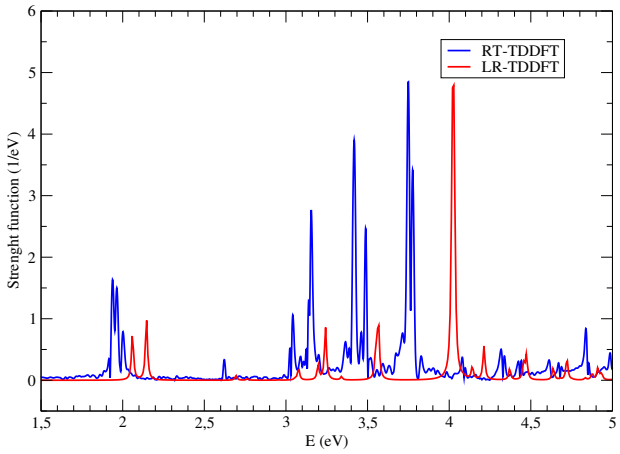

Figure 4.3: Comparison between real time and linear response time dependent density functional theory for the main transitions.

4.1.2 ZnPc and PdPc photoabsorption spectra.

The photoabsorption spectra of ZnPc and PdPc were obtained in the same way as in the previous section. A total simulation time of 400 1/eV, time step of 0.002 eV, mesh spacing of 0.15 Å and a radius of 4.5 Å. The dipolar moments along x and y are equivalents in this case due to the symmetry. In addition, the simulation of the photoabsorption spectra was carried out taking into account the three directions to ensure this fact. In Fig. 4.4 the variation for the dipolar moment and the photoabsorption spectra are shown.

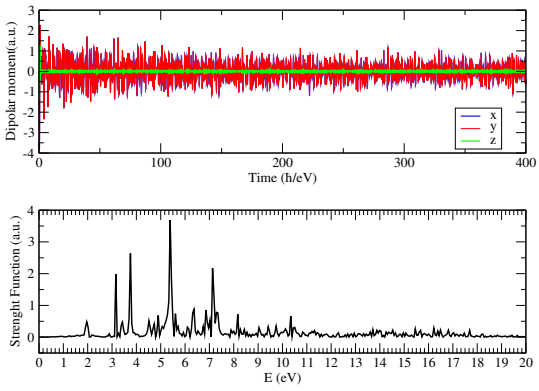

Figure 4.4: On the top is the dipolar moment variation due to the perturbation applied and on the bottom the photoabsorption spectra is shown for ZnPc.

The fundamental transition is located at 1.91 eV and it is close to the optical spectra obtained from the STM experiment (Fig. 4.5). The theoretical spectra is in good agreement whit a shift of 0.01 eV respecting the experimental spectra. The experimental ZnPc spectra is located at 1.899 eV. This main transition corresponds to degenerated transitions associated to dipoles oriented along the main molecular axes. The experiments associate the spectroscopic behaviour of the fundamental transition to the adsorption site of the ZnPc on top of Cl atoms. As a consequence there is a slight lifting of the degeneracy. From a theoretical point of view this degeneracy lift is related to the dipolar moment variation and not due to the position of the molecule on the NaCl surface. Also, a comparison between RT-TDFT and LR-TDDFT can be done in the same way as above(Fig. 4.6). The comparison between spectra shows a gap of 0.20 eV in energy. The B band is observed at 3.77 eV and 4.05 eV for RT-TDDFT and LR-TDDFT, respectively. In addition, both methods are in good agreement with the experimental spectra. The LR-TDDFT has a shift in energy about 0.20 eV.

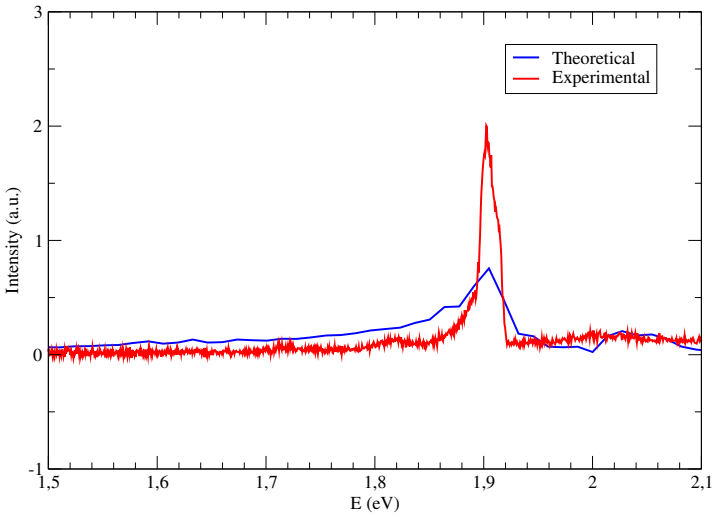

Figure 4.5: Theoretical spectra of the fundamental transition comparing with the experimental values for ZnPc with a energy resolution of 0.0001 eV.

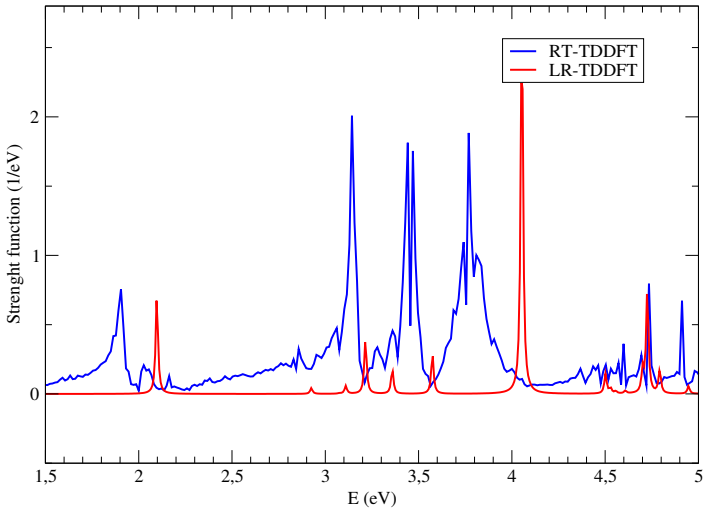

Figure 4.6: Spectra comparison of ZnPc between real time and linear response time dependent density functional theory for the main transitions.

Palladium phthalocyanine photoabsorption cross section spectra (Fig. 4.7) was computed in the x, y and z. As in the case of the ZnPc molecule, the dipolar moment propagation along x and y is equivalent due to the symmetry of the molecule. A total time of 400 1/eV and a time step of 0.002 1/eV was considered to compute the dipolar moment variation.

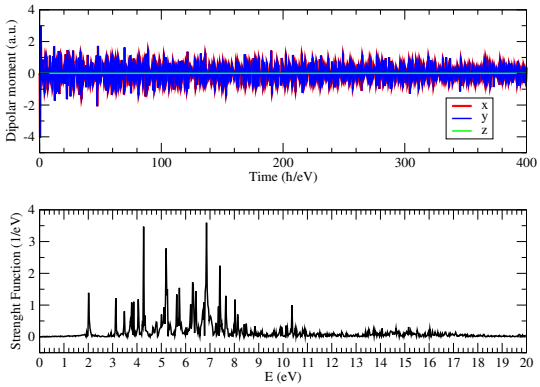

Figure 4.7: On the top is the dipolar moment variation due to the perturbation applied and on the bottom the photoabsorption spectra is shown for PdPc.

The degenerated fundamental transition for PdPc is located at 2.01 eV and the B band at 3.48 eV which is in agreement with the experimental results [195]. The fundamental transition obtained from the STM experimental transition is located at 1.92 eV. A shift of 100 meV is obtained between both methods. It can be considered in good agreement between theory and experiment due to the different techniques used to obtained the absorption spectra. Comparing with LR-TDDFT method (Fig. 4.9) it is possible to visualize a shift of energy around 0.1 eV between them for the Q and B band.

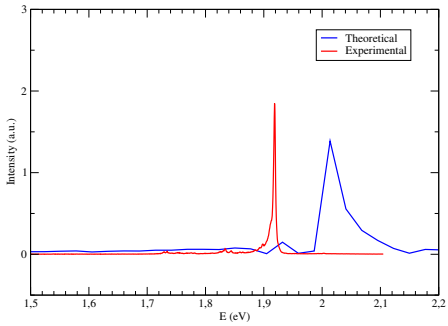

Figure 4.8: Photoabsorption comparison between theory and experiment for PdPc.

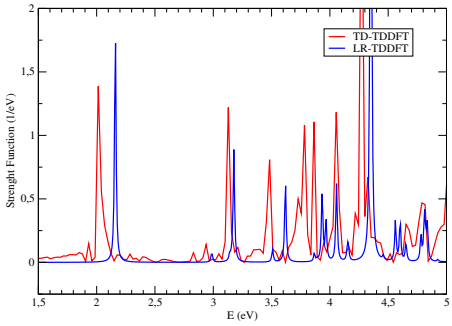

Figure 4.9: Spectra comparison of PdPc between real time and linear response time dependent density functional theory for the main transitions.

4.2 Local perturbation applied onto the molecules.

In the previous section the molecules were perturbed using a laser as a source of excitation. Nevertheless, for an accurate description of the STM experiment, the molecule must be perturbed locally. For this task, and taking into account the small lateral extension of the tunneling path between the tip and the substrate, the excited domain is much smaller than a typical size of the molecule leading to a spatial localization of the excitation. Currently, Octopus software allows the user to define the nature of the excitation source. Normally, the action of a electromagnetic field is defined as the action of a laser onto the molecule along x, y and z. Hence to this fact, a Gaussian function was selected to model the action of the perturbation. The use of a Gaussian function was considered due to the capability to be tuned. Setting the x_0, y_0, z_0, the amplitude (A) and the variances (σ_x,σ_y and σ_z) in Eq. 4.8 the system can be perturbed locally.

$$F(x,y,z) = Aexp\left(-0.5\left(\frac{(x-x_0)^2}{2\sigma_x^2} + \frac{(y-y_0)^2}{2\sigma_y^2}\frac{(z-z_0)^2}{2\sigma_z^2}\right)\right) \tag{4.8}$$

The laser field is treated as a scalar potential described by a Gaussian function define the type and an envelop modeling the time dependent external perturbation ($F(x,y,z)cos(\omega t + \phi(t))g(t)$). g(t) is the envelope function and $\phi(t)$ is the time dependent phase and ω is the frequency of the perturbation. This scalar potential is described as an inhomogeneous electric field. The inhomogeneity is the consequence of the local behaviour considered in the study.

4.2.1 Action of the local perturbation on H_2Pc.

The evolution of the dipolar moment under a local perturbation were carried out with the same parameters described for the global excitation. The differences related to it is the parametrization of the local perturbation. The amplitude is selected to 0.01 and the value of 1.0 for the variances Eq.4.8. The position where the local perturbation is applied on H_2Pc can be carried out with two main positions located at the center of the benzene ring Fig.4.10. H_2Pc is perturbed in two positions due to the D_2h symmetry of the molecule. From an experimental point of view the perturbation can be applied in any position of the molecule. However, for practical reasons the selected positions were chosen with the aim to align the variation of the dipolar moment with the x and y axis.

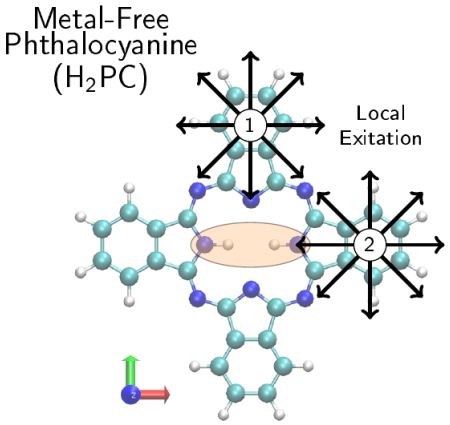

Figure 4.10: Positions where the local perturbation was applied onto the molecule

In Fig.4.11, the coordinates of the perturbation applied in position 1 are (0,5.37,0). The variation of the dipolar moment corresponds, mainly, with the y component of the dipolar moment containing C_2 symmetry axis perpendicular to the inner Hydrogen atoms of the molecule. In addition, the x component of the dipolar moment is minimal. The contribution of this component in this direction has almost no impact on the electronic density distribution of the molecule. In the other hand, the contribution of the z component has a great contribution to the global dipolar moment due to the interaction of the perturbation applied with the π aromatic system of the molecule.

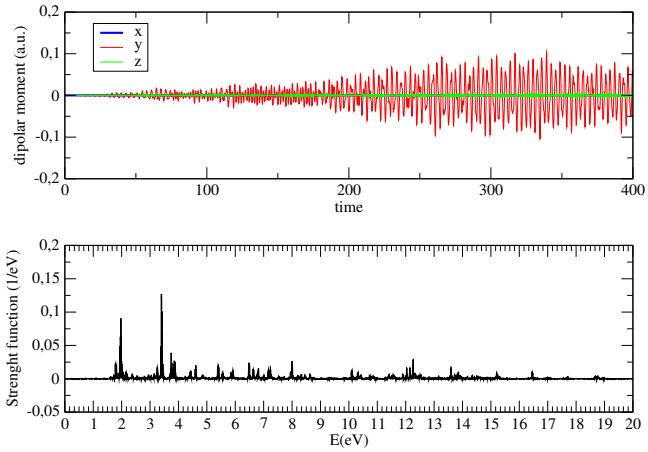

Figure 4.11: Local perturbation applied on H_2Pc in the position one.

The charge density distribution along the z direction is bigger than along x. Conversely, when the molecule is excited in the position 2 with coordinates (5.37,0,0) an opposite result is obtained. In this case the contribution of the y component to the dipolar moment is, practically, null. The main component of the dipolar moment in this case is the contribution of the x component. This component is aligned with a C_2 symmetry axis which contains the two inner hydrogen atoms.

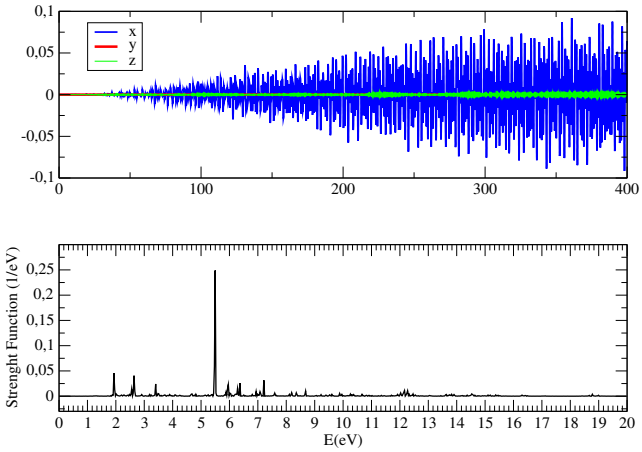

Figure 4.12: Local perturbation applied on H_2Pc in the position two. On top the dipolar moment variation and at the bottom the photoabsorption spectra.

Comparing both spectra, it can be verified that depending on the position where the perturbation has been applied there are discrepancies among them Fig. 4.13. The main difference is the intensity of the transition at 3.45 eV.

This transition is the characteristic phthalocyanine B band. the perturbation along position 1 makes this band more intense, what could be translated into a transition more favorable with respect to position 2 with less energy.

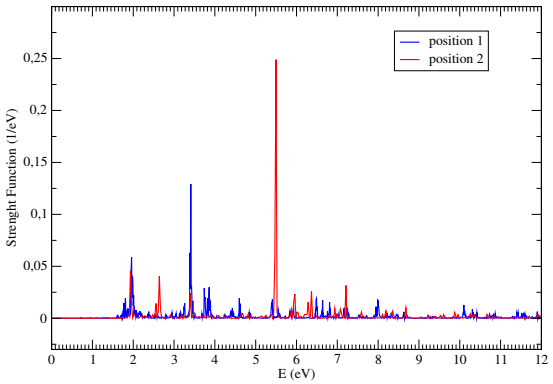

Figure 4.13: Comparison of the action of a local perturbation depending the position onto H_2Pc.

Focusing on the fundamental transition (Fig. 4.14), it can be seen that the results obtained are the same as in the case of global perturbation. In this case, the perturbation on position 2 leads to a single band obtained like the propagation of the dipole moment on the x direction of the global perturbation. Conversely, when the local disturbance is applied on position 1 the two bands Q_x and Q_y are obtained along the y axis. The position of the bands are located at the same energy as in the case of the global perturbation (1.93, 1.96 and 2.02 eV respectively).

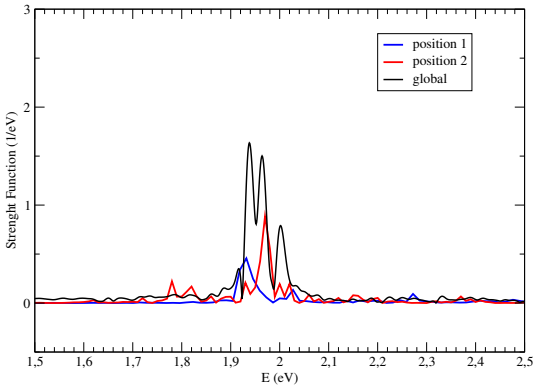

Figure 4.14: Comparison of the fundamental transition due to the action of a local perturbation depending on the position and the global perturbation for H_2Pc.

A third intermediate position between position 1 and position 2 has been selected to check the impact of a local perturbation on the molecule

considering the position where it is applied. The position selected is located on a Nitrogen atom which makes the link between the rings (Fig. 4.15). In contrast with the other positions, the action of this perturbation shows a variation of the total dipole moment with notable contributions from the components x and y.

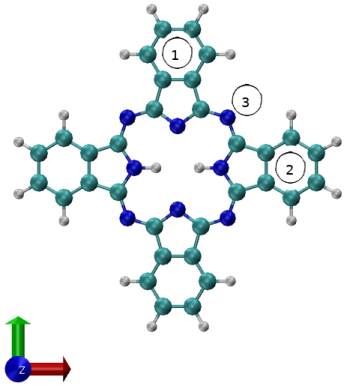

Figure 4.15: Positions where the local perturbation was applied.

The total dipolar moment evolution and the cross section tensor spectra is shown in Fig. 4.16. The result of the action of the local perturbation on this position gives equivalent results as in the action of the global perturbation. The resulting spectra can be considered as the sum of the two spectra of local perturbation at 1 and 2 (Fig. 4.17). A strong interaction of the perturbation along x and y with the electronic density is the consequence of this behaviour.

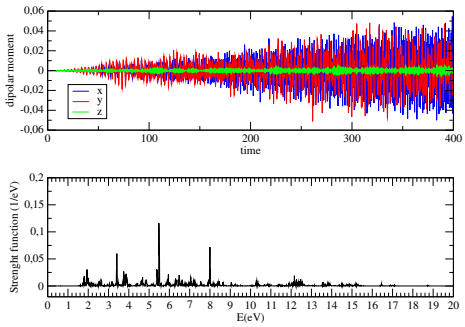

Figure 4.16: Dipolar moment variation and photoabsorption spectra for the local perturbation applied in position 3 on H_2Pc.

The intensity of the bands for the three different positions is relatively small in comparison with the global perturbation. The result of the action of the local perturbation onto the position three shows three bands, two of them at 1.94 eV and 1.96 eV which correspond with the degeneration of the

Q_x band. On the other hand, the Q_y band is located at 2.02 eV. There is a difference of 10 meV of difference in position two. Notably, the appearance of two bands at 1.78 and 1.80 eV can be the result of the action of the local perturbation onto the nitrogen atom.

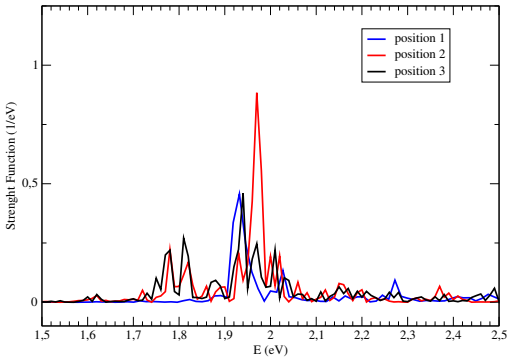

Figure 4.17: Spectra comparison for all the positions where the local perturbation was applied.

4.2.2 Action of the local perturbation on ZnPc.

The Zinc metallo-phthalocyanine was perturbed in two different positions Fig. 4.18. The main difference related to H_2Pc is that in this case all the rings of the molecule are identical by symmetry. So, the action behaviour of the dipolar moment variation is equivalent, independently of the position of the perturbation in any of the selected ring.. In Fig. 4.19 the time dependent dipolar moment variation and the photoabsorption spectra are shown for both positions.

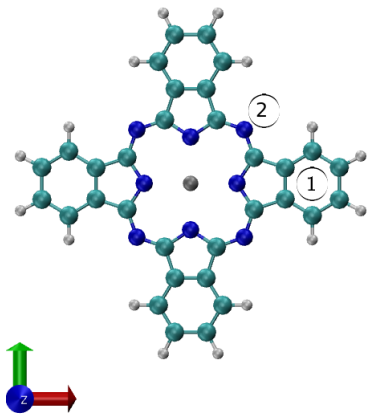

Figure 4.18: Positions where the perturbation was applied ion ZnPc molecule.

The simulation has been carried out with a spacing of 0.16 Å and a radius of 4.5Å. The total simulation time is 400 1/eV and a time step of 0.002 eV. The fundamental transition is located at 1.90 eV in the photoabsorption spectra. The B band is located at 3.46 eV for both positions. This values are in good agreement with the experimental spectra for the perturbation in both positions Fig. 4.20. For both cases, a break of the degeneracy due to the action of a local perturbation is shown. In the case of the perturbation in the position 1 a split in the fundamental transition with respect to the global perturbation is observed. This is a consequence of the action of the local perturbation onto the molecule. In the case of the global perturbation the molecule is perturbed simultaneously along the selected direction.

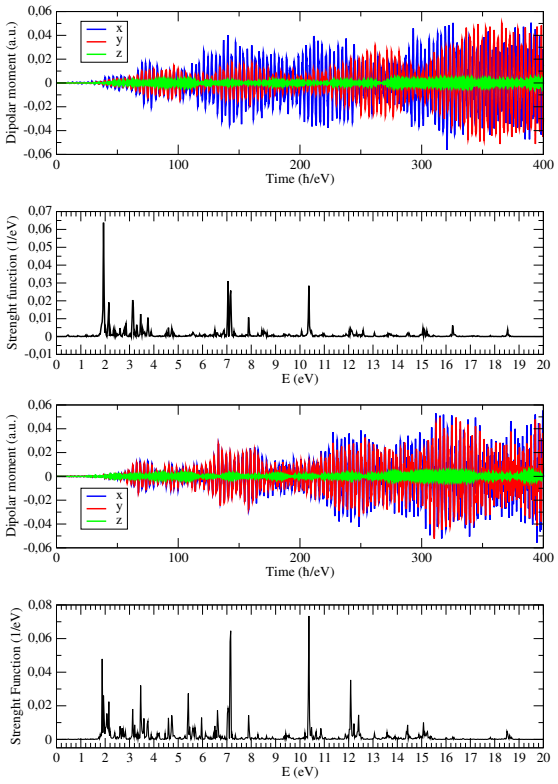

Figure 4.19: Comparison between a local perturbation and global perturbation for ZnPc.

The range of action for the local perturbation depends on the amplitude selected in the gaussian function. If the modelization of the excitation source excite a determined region of the space, as in this methodology, the D_4h symmetry the molecule had, when the simulation started, is broken due to

the local interaction between the source and the density. The Q_x band is located at 1.93 eV and 1.87 eV for the position 1 and 2 respectively. A second Q_x band at 1.93 eV is observed for position 2. Also, the Q_y bands are located at 2.14 eV for position 1 and 2. In fact, the determination of this fact is very interesting due to the nature of the excitation source. Therefore, in order to describe in a rigorously way from a theoretical point of view the effects caused by a local perturbation it is possible to describe this degeneracy break as a consequence of the local action of it. As in the case of H_2Pc, due to the local action of the perturbation, the dipolar moment variation behaviour depends on the position where the perturbation was selected to act.

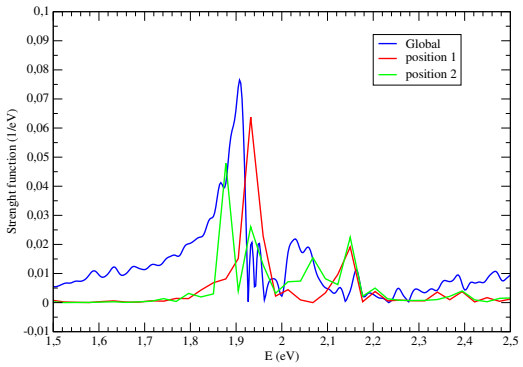

Figure 4.20: Comparison between a local perturbation and global perturbation for ZnPc.

4.2.3 Action of the local perturbation on PdPc.

For Palladium metallo-phthalocyanine, as ZnPc and H_2Pc, the photoabsorption spectra was obtained by a total simulation time of 400 1/eV with a time step of 0.002 eV. The spacing and radius values are 0.16 Å and 4.5 Å respectively. To obtain the absorption spectrum, it has been considered, as in the case of the Zn two spatial positions (Fig. 4.21). The position one is located in one of the four equivalent aromatic rings and the second position where the local perturbation was applied relies on one of the nitrogen atoms which is the bridge between rings.

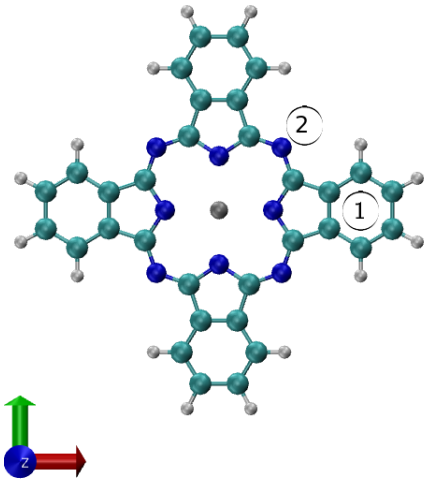

Figure 4.21: Positions where the local perturbation was applied on PdPc molecule.

In Fig. 4.22 the dipolar moment variation and the photoabsoption for both spatial positions are shown.

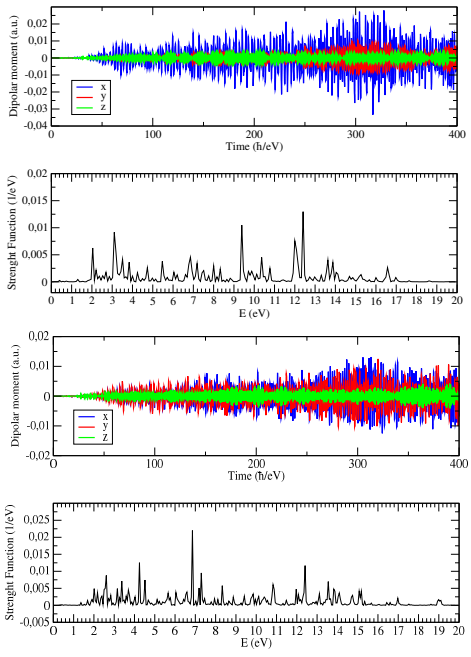

Figure 4.22: Dipolar moment variation and photoabsorption spectra for the two positions where the perturbation was applied. On the top the position 1 is shown and on the bottom the position 2.

In Fig. 4.23 the fundamental transition is plotted for the local perturbation action in position 1, position 2 and comparing them with respect to the global perturbation. The action of the local perturbation reveals a shift in the fundamental transition for both cases. In position 1 the Q_x is located at 2.03 eV and the Q_y band at 2.20 eV. In the case of position 2, the Q_x band is located at 2.01 eV and the Q_y band at 2.17 eV. Between both positions there is an energy shift of 20 meV for the Q_x band and 30 meV for the Q_y. Comparing the results described above with the experimental value there is a shift of 100 meV for position 1 and 120 meV for position 2. The same explanation can be made for the splitting of the fundamental transition for PdPc like in the previous cases. The local action of the perturbation on the D_4h symmetry is broken becoming a D_2h.

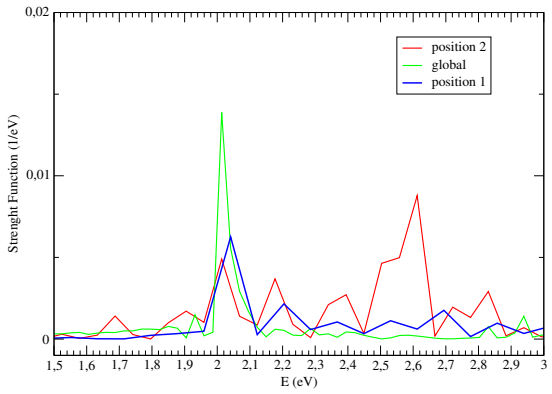

Figure 4.23: Comparison between a local perturbation and global perturbation for PdPc.

4.3 Energy transfer between molecules.

In this section the RT-TDDFT theory is used to investigate the energy transfer phenomena between chromophores. It is based primarily on dipole-dipole interactions occurring between high energy-gap chromophores to lower energy-gap chromophores. The influence of parameters as exchange interactions effects mediates energy transfer at short distances [196], delocalization of the excitation over coherently coupled molecules involving vibronic coupling or not [197, 198] or promoted energy transfer by the environmental medium[199, 200] can be tuned to improve the efficiency of the process. This resonant transfer of energy between chromophores plays a crucial role enabling an efficient and directional transport of solar energy between collection and reaction centers.

Recently, some experiments have shown that a scanning tunneling microscope (STM) operated at low temperature under ultra-high vacuum can be used to probe the fluorescent properties of individual or interacting chromophores with high spatial, spectral and temporal resolution. [25, 39, 41, 42, 201]. As an initial step the resonant transfer of energy efficiency between a pair of chromophores in a STM junction depends on the spectral overlap, the distance and the orientations between the transition dipole moments of the donor and acceptor molecules. The STM can be used as a selective and local source of excitation of molecular dipoles. Hyper resolved fluorescence microscopy maps [42] allows us to follow the energy transfer path from molecule to molecule in real space, revealing a resonant energy transfer path in real space between chromophores. The resonant transfer energy were carried out in inhomogeneous media, and which play a decisive role in fastening the energy transfer process in photosynthetic systems [199, 200].

The pioneering works of Zhang *et al.*[202] and Imada *et al.* [203] have reported the emission of coherently coupled chromophores and resonant energy transfer between a single donor and a single acceptor molecules. To study this approach from a theoretical point of view, the systems H_2Pc-ZnPc, H_2Pc-ZnPc and PdPc-ZnPc were considered. Resonant energy transfer relying on the dipole-dipole interactions, are, in principle, impacted by the angle between the donor and acceptor dipoles [204]. However, the energy transfer is much less efficient when the dipoles are essentially parallel to each other. This observation implies that one can selectively excite a given dipole of a molecule by locating the perturbation on it. In addition, the molecular disposition considered is the lock-key configuration. A local perturbation is applied on the molecule with higher energy gap. A previous parametrization of the spacing and radius was carried out as in the case of isolated molecules. A regular grid was chosen under the LDA approximation describing the exchange-correlation effects with the PZ functional. The core electrons were described with the Troullier-Martins non-relativistic non-local norm-conserving pseudopotentials. The evolution of the dipolar moment under the influence of a local perturbation was computed with a total time of 400 1/eV and a time step of 0.002 eV an amplitude of 1 eV/Å and $\omega = 3$ eV. the midpoint rule was selected as the propagator approximation. The Lanzcos method was used to compute the exponential of the Hamiltonian. The modeled local perturbation used is the same as in the previous section with an amplitude of 0.01 and 1.0 for the variances.

4.3.1 H_2Pc-ZnPc sytem

In the system H_2Pc-ZnPc (Fig. 4.24) the local perturbation was applied onto the ZnPc molecule. The selection of the spacing and radius value is shown in Fig. 4.26. The properly values considered to run the RT-TDDFT

simulations were 5.0Å for radius and 0.15 Å for spacing. In addition of the comments done in the parametrization of the isolated molecules, a radius of 6.0 Å requires a big amount of computational resources. The radius value is fully converged at 3.5 Å and the value of 5.0 Å was considered to be sure that the accuracy of the simulation obtained is well defined. In the other hand, a value of 0.15 Å ensures a good discretization mesh.

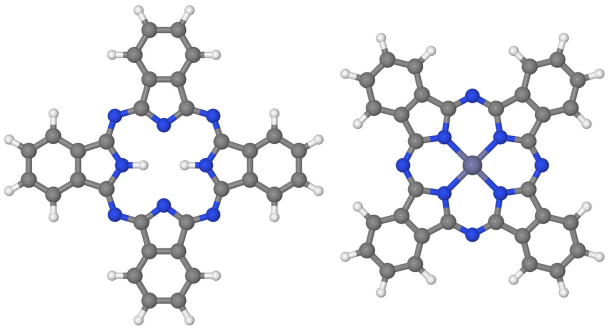

Figure 4.24: H_2Pc-ZnPc molecular system used on the simulation

The photoabsorption spectra were computed using a local perturbation acting in the lower-right benzene ring of the ZnPc molecule. The local perturbation is applied onto this position considering that the high energy-gap chromophore is the ZnPc molecule. The same procedure followed in all RT-TDDFT simulations was carried out. The global dipolar moment is computed along all spatial directions (x, y and z) the result of the FFT transform of the dipolar moment variation gives the photoabsorption spectra displayed on Fig. 4.25.

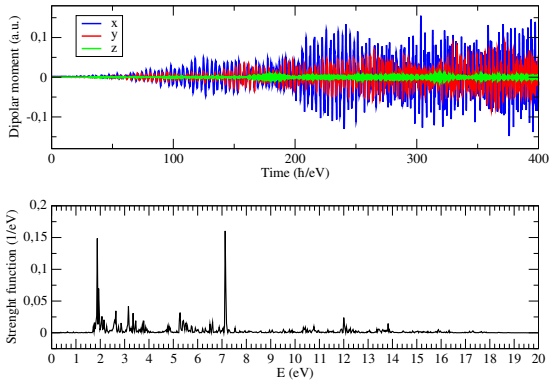

Figure 4.25: Dipolar moment variation and photoabsorption spectra for the system H_2Pd-ZnPc

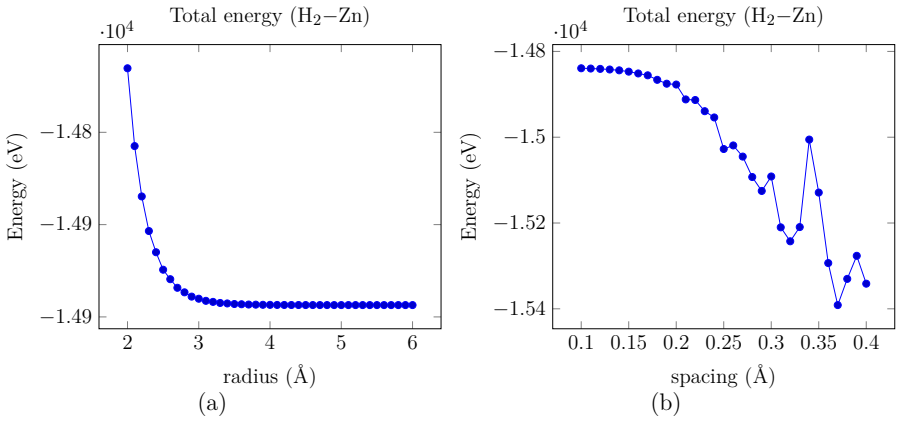

Figure 4.26: Total energy evolution as a function of a) the radius between two nodes of the mesh b) the spacing between two neighbours of the mesh.

The energy transfer can be described following the evolution of the dipolar moment along the TD simulation run. To this task, the photoabsorption spectra was plotted every 50 1/eV. The aim of this procedure is to follow the evolution of the fundamental transition of the two molecules to describe the energy transfer. The spectra for the total simulation time shows two fundamental bands at 1.87 and 1.93 eV. The first band is the fundamental transition for ZnPc and the second is the Q_x band for H_2Pc. The affirmation of an energy transfer mechanism between the two molecules is corroborated with the evolution of this peaks along the simulation time (Fig. 4.27).

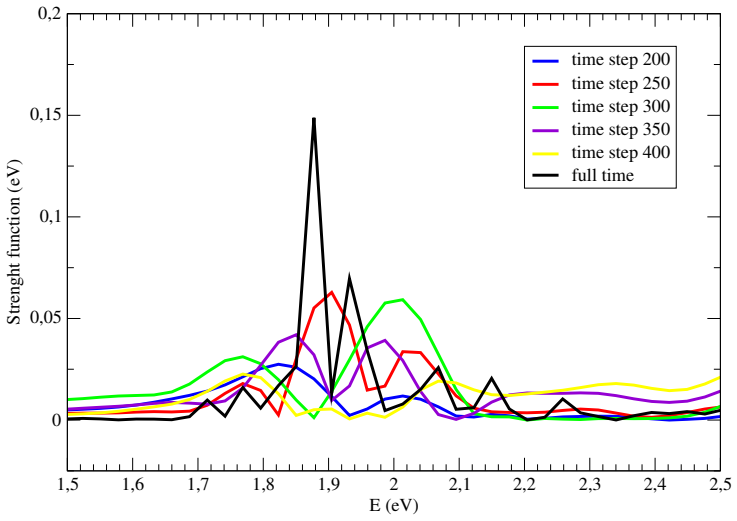

Figure 4.27: Fundamental transition evolution during the simulation time plotted every 50 1/eV time steps

The less energetic peak correspond to the ZnPc and the most energetic corresponds to the H_2Pc. The first plot corresponds to a simulation time of 200 1/eV. This start point has been selected due to the small intensity of the peaks and for the spectra clearance. The tracking of the peaks shows a evolution on the intensity, less energetic peaks (left peak) which corresponds to the ZnPc is more intense than the most energetic peak (right peak) which corresponds to the H_2Pc until a simulation time of 300 1/eV when the H_2Pc becomes the most intense peak. Should be notice that the perturbation applied in the upper-right benzene ring of ZnPc.

It means, apparently, that the ZnPc is excited. The distance of 1.5 nm between molecules is close enough for the dipole-dipole interaction. This dipole-dipole interaction makes possible the energy transfer between molecules and exciting the H_2Pc, which is a reasonable distance from the excitation source. However, the total photoabsorption spectra shows a left intense peak and a less intense right peak. This behaviour is explained due to the fact that this spectra is plotted for all simulation time and is an "average" of all time interval spectra plotted in the figure.

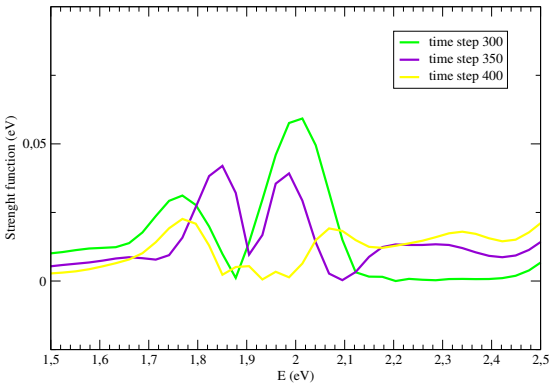

Figure 4.28: Proof of the local perturbation dissipation during the time.

Also, as the local perturbation was only applied for a short period of time at the starting point of the simulation, the dissipation of the perturbation can be probed (Fig. 4.29). The interval time of 350-400 1/eV shows an intensity loss in the peaks and an energy shift in comparison with the other interval time. Also it is corroborated that in the interval time of 300-350 1/eV, both peaks have the same intensity.

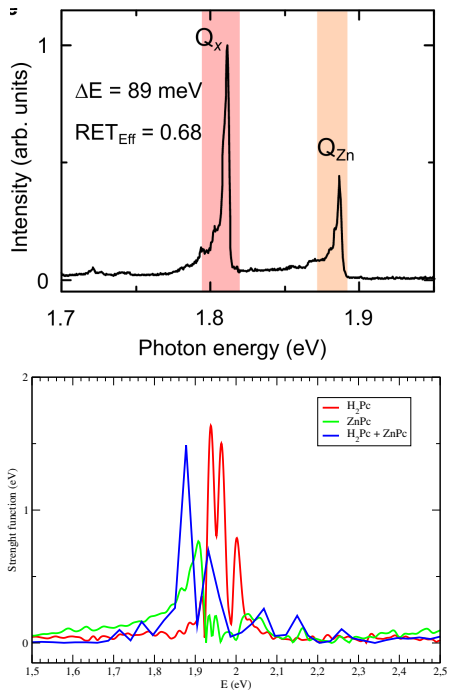

Figure 4.29: On the top, STML spectra, I=300 pA, acquisition time $t = 300$ s. At the bottom the theoretical spectra obtained and compared with the spectra obtained with a global perturbation for the isolated molecules.

The loss of intensity can be explained with the dissipation of the source of excitation after a long simulation time which was applied at time zero for a short period of time. In comparison with experimental results, the direct excitation of the acceptor molecules are negligible. The spectra (Fig. 4.27) displays peaks at the energy of both chromophores, attesting that part of the energy of the donor is transmitted to the acceptor. This phenomena has been described in terms of a resonant transfer energy process involving dipole-dipole interactions [203]. The main difference is the switch on the peaks. It is due to the shift in energy of the H_2Pc spectra related to the STM. Experimentally the effective resonant energy transfer can be defined as $RET_{eff} = I_a/I_d + I_a$, where I_d and I_a are the emission intensities of the donor and acceptor in the dimmer, respectively[205]. For the H_2Pc-ZnPc system $RET_{eff} = 0.68$. This quantity is more efficient when the difference in the gap energy between both chromophores is small. From RT-TDDFT simulation the energy transfer between chromophores for the system H_2Pc-ZnPc has been probed. The dipole-dipole interaction between molecules can be probed, but again the computation resources needed is the weak point. For distance of 1.5 Å (the same as in experiment) between molecules was computed using 25 cores and 600 processors with a RAM memory of 115 Gb per core in the HSW24 partition of occigen batch from Centre Informatique

National de l'Enseignement Supérieur (CINES). Increasing the distance between molecules also, increase the number of points of the simulation, and also increasing the amount of resources.

4.3.2 H_2Pc-PdPc system

The system H_2Pc-PdPc is perturbed in one of the rings of the Pd molecule far from the free-metal phthalocyanine. The selection of this position was considered because the PdPc has the high-energy gap (Fig. 4.30). The parametrization of the spacing and radius are shown in Fig. 4.31, the selected values are 0.15 Å for spacing and 5.0 Å for radius and the distance between molecules is 1.5 nm. The photoabsorption spectra is computed using the same parameters of all RT-TDDFT simulations carried out in this manuscript (total simulation time 400 1/eV and 0.002 eV time step).

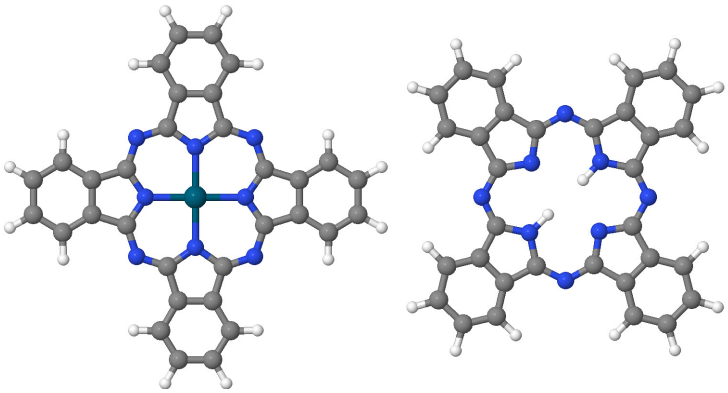

Figure 4.30: Molecular system used on the simulation

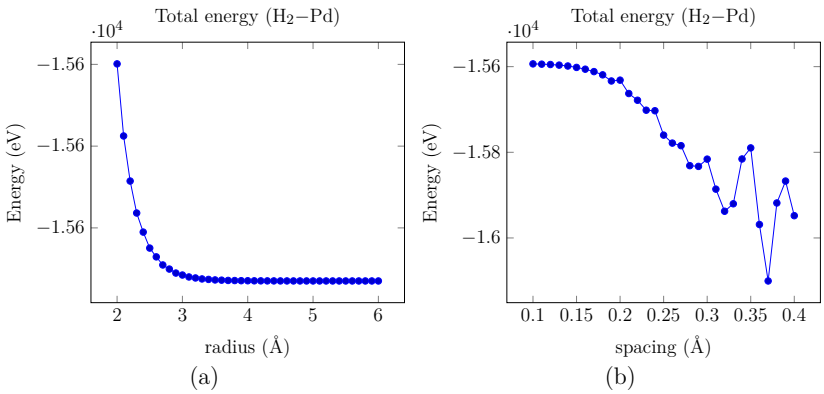

Figure 4.31: Total energy evolution as a function of a) the radius between two nodes of the mesh b) the spacing between two neighbours of the mesh.

The fundamental transitions of the two molecules are located at 1.93 eV for H_2Pc and 2.03 eV for PdPc molecule (Fig. 4.32).

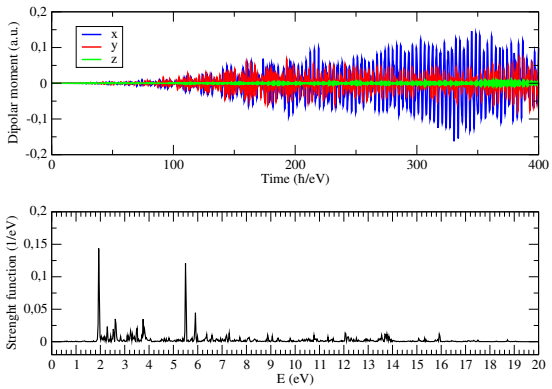

Figure 4.32: Dipolar moment variation on the top and photoabsorption spectra at the bottom for H_2Pc-PdPc system due to the action of a local perturbation.

The evolution of the dipolar moment tracked in intervals of 50 1/eV are plotted in Fig. 4.33.

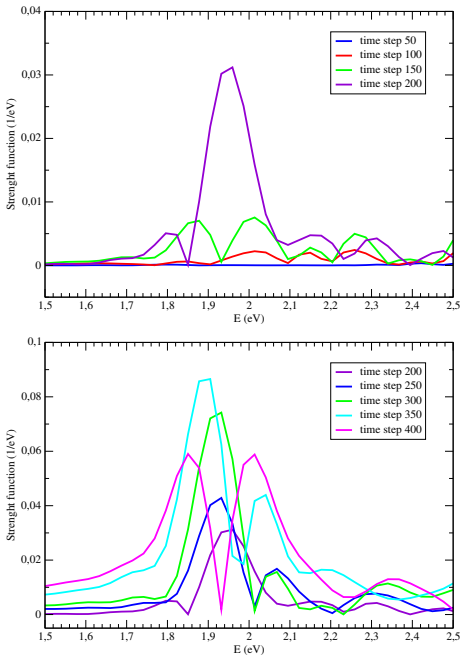

Figure 4.33: Photoabsorption spectra computed every 50 1/eV time step to track the evolution of the fundamental transition.

The plot on the top shows the evolution of the fundamental transition at 200 1/eV. With a simulation time of 100 1/eV the fundamental transition of PdPc is observed in the next interval of time both fundamental transitions are observed. After a simulation time of 200 1/eV the fundamental transition of H_2Pc becomes the more energetic transition, corroborating the energy transfer between molecules. The plot on the bottom, shows the plots for the interval time of 200 1/ev and 400 1/eV a increase on the intensity of the fundamental transitions is shown. After a simulation time of 400 1/eV the intensities are starting to decrease, it seems that the local perturbation is starting to dissipate.

Comparing with experimental results from STM (Fig. 4.34), RT-TDDFT displays peaks at the energy of the fundamental transitions of both molecules. The energy transfer mechanism can be explained with a dipole-dipole interaction between molecules. The distance between molecules in the RT-TDDFT simulation is 1.5 nm. This distance is far enough to avoid the molecule interactions and to ensure the dipole-dipole interaction. An energy shift about 0.1 eV is shown for the theoretical spectra in comparison with the experimental. Despite this energy shift, the energy transfer between the high gap and the low energy gap chromophore achieved by theoretical and experimental studies are in good agreement.

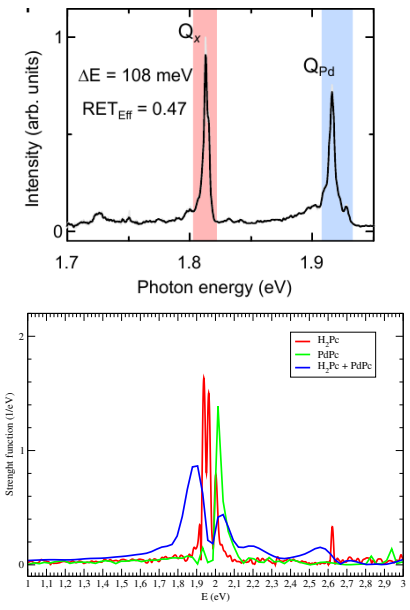

Figure 4.34: On the top, STML spectra, I=300 pA, acquisition time $t = 300$ s. At the bottom the theoretical spectra obtained and compared with the spectra obtained with a global perturbation.

4.3.3 ZnPc-PdPc system

The system ZnPc-PdPc (Fig. 4.35) as in the case of H_2Pc-PdPc the local perturbation is applied on one aromatic ring far from the second molecule. The PdPc is the chromophore with the highest energy gap of both molecules.

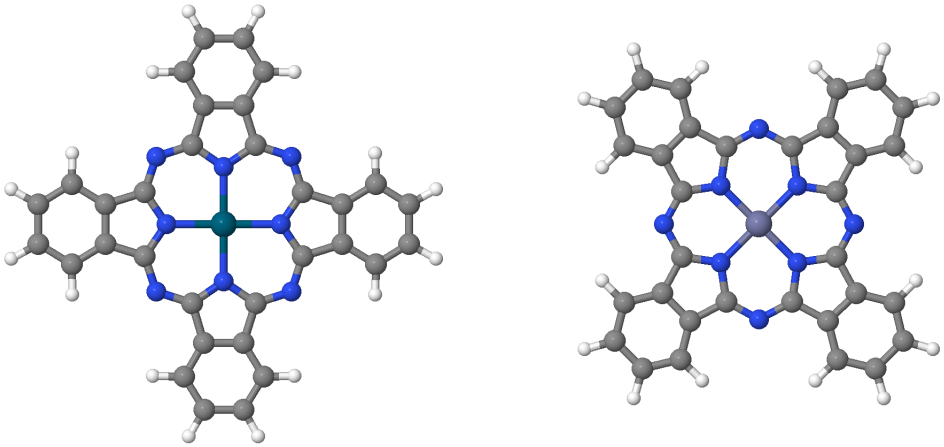

Figure 4.35: ZnPc-PdPc system scheme, the molecule at left is the PdPc molecule where the perturbation was applied and at right the ZnPc molecule with a distance of 1.5 nm between them.

The selected values of the spacing and radius are 0.15 Å and 5.0 Å respectively (Fig 4.36).

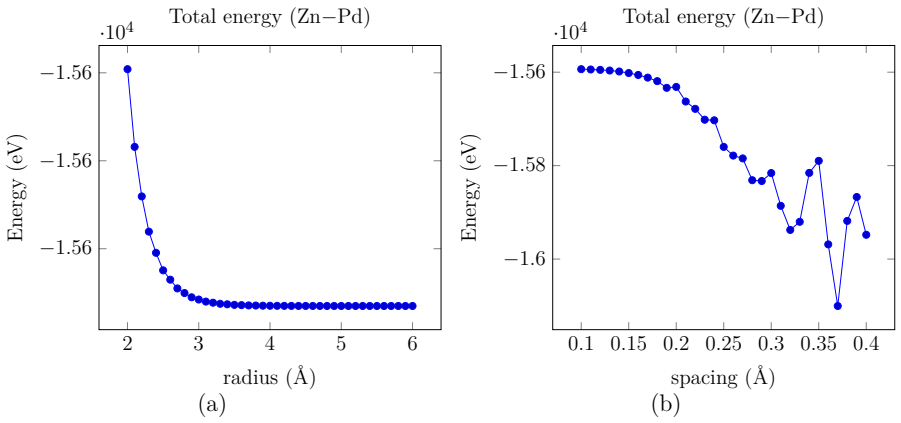

Figure 4.36: Total energy evolution as a function of a) the radius between two nodes of the mesh b) the spacing between two neighbours of the mesh.

The photoabsorption spectra was computed for a total simulation time of 400 1/eV and a time step of 0.002 1/eV(fig, 4.37).

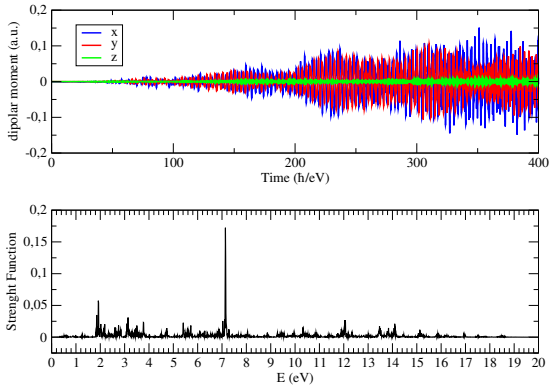

Figure 4.37: Dipolar moment variation at the top and the photoabsorption at the bottom for the ZnPc-PdPc system.

The fundamental transitions are located at 1.86 eV for ZnPc and 1.92 eV for PdPc. In Fig 4.38 the photoabsorption spectra is plotted every 50 1/eV time step. In that spectra is shown the evolution of the fundamental transitions for both molecules. At time step of 200 1/eV the PdPc molecule is excited. Therefore, as time progresses, it is clearly seen that the Zn molecule begins to get excited. The ZnPc fundamental transition becomes the most intense at a time step of 300 1/eV. Also at a time step of 350 1/eV confirms the energy transfer between molecules because the ZnPc transition is the most intense of both transitions.

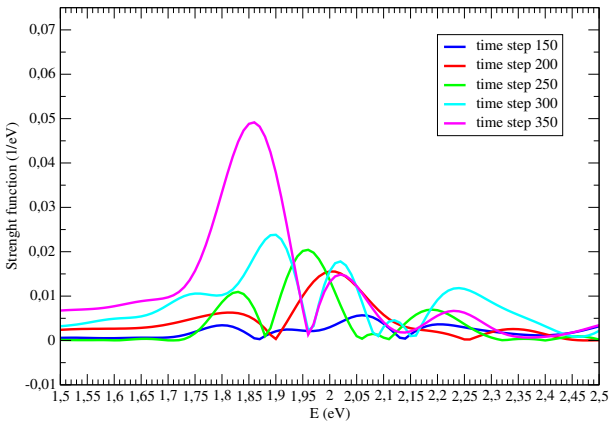

Figure 4.38: Variation of the fundamental transition for the ZnPc-PdPc system plotted every 50 1/eV time step.

In Fig 4.39 the global perturbation of the isolated molecules are plotted with respect to the local perturbation applied onto the Zn-Pd system. There is a difference of 5 meV for the fundamental transition of the Zn and a difference of 9 meV in the case of PdPc. This energy shift can be explained due to the dipole-dipole interaction between molecules. Comparing with the experimental results also a difference of energy around 5 meV is obtained for the ZnPc fundamental transition. In the case of PdPc this difference is around 4 meV when the local perturbation is applied on the system. This difference is lower than in the case of the global perturbation of the isolated molecule.

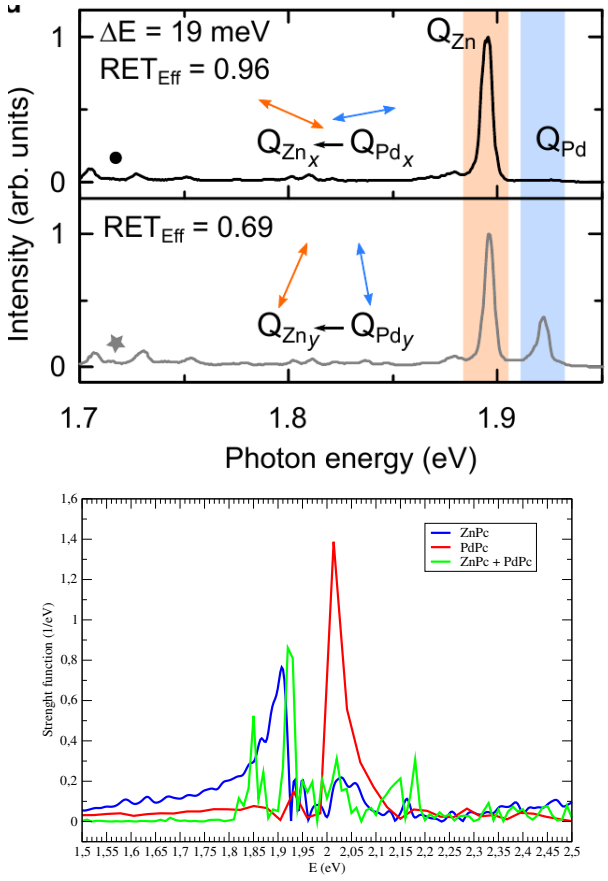

Figure 4.39: On the top, STML spectra, I=300 pA, acquisition time $t = 300$ s. At the bottom the theoretical spectra obtained and compared with the spectra obtained with a global perturbation.

From a experimental point of view the dipole-dipole interactions are impacted by the angle between chromophores (Fig 4.40). Two positions are perturbed (black dot and grey dot in the figure). The spectra reveal that the

energy transfer is more efficient when the tip is located on top of the PdPc dipole oriented towards the ZnPc acceptor (Fig 4.39) corresponding with the situation where the donor and acceptor dipoles are colinear. By analyzing the RET_{eff} parameter it is also possible to affirm that the resonant energy transfer is much less efficient when the dipoles are essentially parallel to each other (Gray spectra).

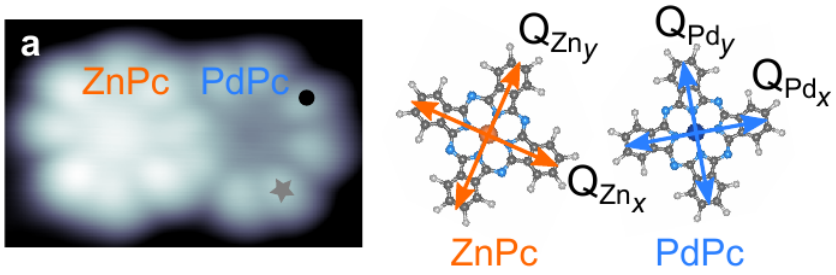

Figure 4.40: STM image (5.1 x 3.2 nm^2, V=-2.5 V for the ZnPc-PdPc system.

4.4 Conclusion

The results presented in this chapter are divided in three blocks correlated between them. The real space propagation gives enough information to obtain a clear physical image of the evolution of the wavefunction in real time. The results are focused in the analysis of the lowest energy peaks. It is due to the accuracy in reproducing transitions of intermediate energy in which it is known to be deteriorated for the wrong asymptotic behaviour of the LDA exchange-correlation potential. In the first part of the chapter, the evolution of the dipolar moment in real time-time dependent density functional theory is shown. Secondly, the action of a local perturbation in a specific position of the molecules was carried out. Last but not least, the study was devoted to the energy transfer between two chromophores.

The results obtained in the first block are the consequence of a perturbation of the molecules along each spatial direction. The Fast fourier Transform for the variation of the dipolar moment along each direction gives as a result the photoabsoption spectra for the moleculeVs studied. The fundamental transition study reveals a good concordance between experiment and theory. A energy shift around 100 meV is obtained for H_2Pc and PdPc molecules and 20 meV for ZnPc. For H_2Pc a decoupling in the fundamental Q_x band

is observed. It is due to the evolution of the dipolar moment along each direction of the space and also the symmetry of the system. The dipolar moment variation was carried out in three independent runs and merged to obtain the full cross section tensor (the photoabsorption spectra).

The action of the local perturbation modeled as a Gaussian function is described as an inhomogeneous electric field. The spectra obtained gives us the opportunity to do a fully description of the excitation mechanism of the molecule. A detailed behaviour depending on the position where the perturbation was applied reveals the decoupling in the Q_x band for H_2Pc. In the position 2 only the Q_x band is obtained. Meanwhile the action of the local perturbation in the position 1, a Q_x and a Q_y is obtained. An intermediate position (position 3) reveals the same behaviour of the global perturbation. On the other hand, the action of the perturbation on ZnPc and PdPc reveals a symmetry break when it acts on the position 2. This behaviour is also obtained for PdPc molecule.

The last part of the chapter was devoted to study the energy transfer between two chromophores. Three systems were taken into account, H_2Pc-ZnPc, H_2Pc-Pd and ZnPc-PdPc. The real time propagation simulations reveals a energy transfer between the two molecules when the higher energy level chromophore was locally perturbed. The track of the evolution of the dipolar moment clearly shows this energy transfer due to the change on the intensity of the fundamental transitions of the molecules of the considered system. The RT-TDDFT methodology followed in this chapter is effective to understand the behaviour of a molecule when it is perturbed for a excitation source as a laser.

Chapter 5

Impact of the tunnel current as source of excitation.

The work presented in the previous chapters indicates that, although we are able to understand and to reproduce a large part of the structures of the spectra of excitation of molecules by a tunnel current observed experimentally, some of them are poorly modeled. We have identified several paths of exploration for explain these disagreements. In the third chapter, the structural effect were considered and the in fourth chapter I have discussed the specific effects associated to the local excitation of the molecule by the tip.

In the third chapter, we have shown that, although the optical spectra is very sensitive to the constraint level applied on the molecule when it is supported in surface of NaCl, the constraint applied is not enough to produce visible effects on the photoabsorption spectra of the supported molecule with respect to the photoabsorption spectra of the isolated molecule. In the fourth chapter the local perturbation applied on the system has been made by a laser field treated as a scalar potential in form of a Gaussian function (Eq. 5.1). This function describes the type and shape of time-dependent external perturbation in the form $F(x,y,z)cos(\omega t+\phi(t))g(t)$. F(x,y,z) is defined by a field type (scalar potential), g(t) is defined by an envelope function and $\phi(t)$ is the time-dependent phase. ω is the frequency of the pulse. This scalar potential described an external field as an inhomogeneous electric field. This inhomogeneity is the local perturbation applied.

$$F(\vec{r},t) = Aexp\left(-\left(\frac{(x-x_0)^2}{2\sigma_x^2}+\frac{(y-y_0)^2}{2\sigma_y^2}+\frac{(z-z_0)^2}{2\sigma_z^2}\right)\right) \tag{5.1}$$

In the considered system the excitation source is a laser spot of just few tenths of nanometers which is not the case in the tunnel junction considered in this work. But from a theoretical point of view it is much simpler to deal with an electric field as excitation source than to deal with an electron. However, this approach has been very useful to get information about the way a perturbation generated locally is propagated inside the molecule and how it may be at the origin of "secondary" excitations specific to location of the "primary" excitation. The evolution of the dipolar moment gives a invaluable information to understand the effect on the excitation of the molecule due to the action of a local perturbation. The results of its action on the isolated molecules are in a good agreement with the experiment as the same for the energy transfer.

In this chapter, the validity of the description of the perturbation used to obtain the photoabsorption spectra is considered. From STM experiment, the tunnel current effect plays an important role in the system of study. It has two major impact on the excitation of a molecular nanojunction. First, due to the small lateral extension of the tunneling path between the tip and the substrate, the excited domain is much smaller than the typical size of the molecule, leading to a spatial localization of the excitation. Secondly, the electronic nature of the excitation source makes the mechanisms at the origin of the excitation of the molecule by the tunnel electron current different from those due to a photon. Hartree and exchange interactions are, for example, specific to the electron and they can produce specific excitation. This excitation can be used for collecting information which can be impossible to get by using a laser as excitation source.

The scanning tunnel microscopy is a versatile technique and is an instrument for imaging surfaces at the atomic level and is based on the concept of quantum tunneling. When a conducting tip is brought very near to the surface to be examined, a bias (voltage difference) applied between the tip and the surface can allow electrons to tunnel through the vacuum between them. The resulting tunneling current is a function of tip position, applied voltage, and the local density of states (LDOS) of the sample[206]. The information is acquired by monitoring the current as the tip's position scans across the surface, and is usually displayed in image form. STM can be a challenging technique, as it requires extremely clean and stable surfaces, sharp tips, an excellent vibration control and sophisticated electronics.

5.1 Modelization of the tunnel current.

The excitation source commonly used is a laser. Laser light is created when the electrons in atoms in special glasses, crystals or gases, absorb energy from an electrical current, or another laser, are excited. This excited electrons come back to the ground state through a deactivation process emitting photons. The photons in turn travel around the space and excite the molecule. The laser has a particular wavelength determined by the amount of energy released excited electron drops to the ground state. Also, the laser is directional with a very tight beam, the coherence of laser light make it stay focused for vast distance.

In this section the development of a theory to describe the time evolution of the tunnel current is presented. The tunnel excitation can be described as a propagation (transmission) of the tunnel electron using a wavepacket from the tip to the substrate (Fig 5.1)

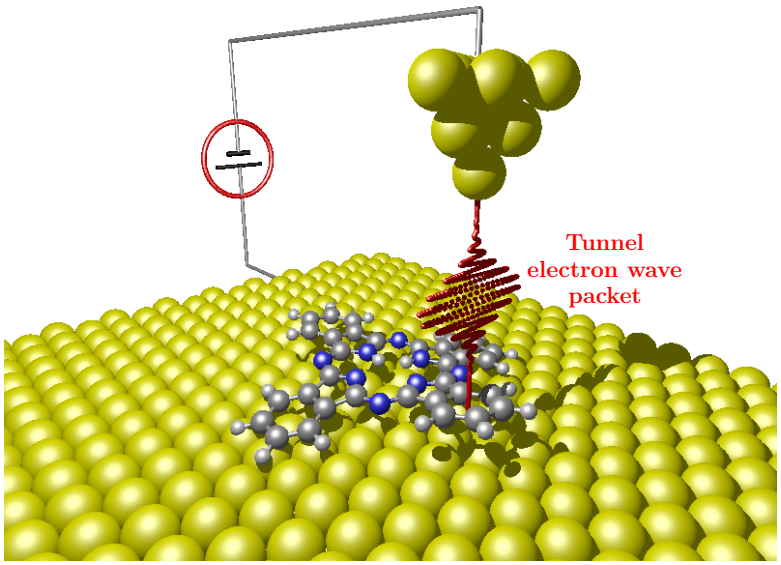

Figure 5.1: Scheme of the local excitation of a phthalocyanine molecule by tunnel electron wave packet supported in a surface.

The one-dimensional wavepacket, initially centered at some position z_0 with a spread Δz, is propagated. An integration of the time-dependent wave equation governed by a time-dependent potential V(z) is required. This wavepacket equation can be written as:

$$\psi_j(\vec{r},t) = \hat{P}\psi_{j,0}(\vec{r}). \tag{5.2}$$

The evolution operator $\hat{P}$ is defined as:

$$\hat{P} = exp\left(-\frac{i\hat{H}t}{\hbar}\right). \tag{5.3}$$

The excitation of the molecule comes from the interaction between the excitation source with the electrons of the molecules. From a physical point of view, the electronic density must be evaluated to understand the excitation process. The changes on the electronic density, induced by the excitation source, which will make it possible to identify the phenomena that may explain the disagreements between theory and experiment. The dimension of the studied system obey the laws of the quantum mechanics. It means that only certain discrete electronic distributions in the system can be observed due to the action of a perturbation.

The goal of this section is to establish a relationship between the changes induced on the electronic density and the perturbation applied on the system. When the molecule is subjected to a excitation source ($\hat{V}(t)$), $|\Psi(t)\rangle$ state will evolve over the time according to the time-dependent Schrödinger equation:

$$\left(\hat{H}_0 + \hat{V}(t)\right)|\Psi(t)\rangle = i\hbar\frac{\partial|\Psi(t)\rangle}{\partial,t} \tag{5.4}$$

where $\hat{H}_0$ is the Hamiltonian without perturbation. In this work, two types of excitation has been taken into account. Firstly, a electromagnetic excitation generated by a laser light beam. Secondly, the tunnel current excitation through the molecule located between the tip and the NaCl surface where it is supported. In both cases, the perturbation generates a displacement of negative charges (electrons) and positive charges (cores) in the molecule. However, the different nature of the two excitations is the source of differences in the excitation spectra. The objective in this chapter is to present these differences.

The response of the molecule due to the action of the perturbation can be estimated analysing the behaviour of the dipolar moment. The molecular dipolar moment is the sum of a electronic and nuclear contribution:

$$\mu_{molecule}(t) = -e\sum_{i=1}^{N_e}\langle\Psi(t)|\,\boldsymbol{r}_i\,|\Psi(t)\rangle + e\sum_{I=1}^{N_n} Z_I\boldsymbol{R}_I\,(t)\,, \tag{5.5}$$

Where N_e and N_n are the total number of electrons and the total number of nuclei respectively. The relative weight of these two contributions depends on the excitation energy. The applied in scanning microscopy tunnel are located in the infrared and visible domains, two domains where the dipole moments electronic and nuclear are of the same order of magnitude[207]. Behind the linear response theory, the state $|\Psi(t)\rangle$ should be computed to evaluate the dipolar moment[208]. The idea of the linear response theory is to express the state of the perturbed system,$|\Psi(t)\rangle$, as a function of the stationary state, $|\Phi_i\rangle$, of the unperturbed system:

$$|\Psi(t)\rangle = \sum_{i=0}\tilde{a}_i(t)\,|\Phi_i\rangle\,. \tag{5.6}$$

In the approach I developed, the ground state of the unperturbed system, $|\Phi_0\rangle$ is computed in the framework of the density functional theory. Therefore, further on how the other stationary states of the unperturbed system are determined. The temporal evolution of the perturbed system $|\Psi(t)\rangle$ is governed by the time dependent Schrödinger equation:

$$\left(\hat{H}_0 + \hat{V}(t)\right)|\Psi(t)\rangle = i\hbar\frac{\partial|\Psi(t)\rangle}{\partial t}. \tag{5.7}$$

Inserting the expression of the wave function in terms of linear response theory (5.6) into the Scrödinger equation (5.7), a set of differential equations of first order are obtained for each of the coefficients $\tilde{a}_i(t)$:

$$i\hbar\sum_{i=0}\frac{d\tilde{a}_i(t)}{dt}\,|\Phi_i\rangle = \sum_{i=0}\tilde{a}_i(t)\left(E_i\,|\Phi_i\rangle + \hat{V}(t)\,|\Phi_i\rangle\right). \tag{5.8}$$

E_i is the eigenvalue associated to the stationary state $|\Phi_i\rangle$ of the unperturbed system:

$$\hat{H}_0\,|\Phi_i\rangle = E_i\,|\Phi_i\rangle\,, \tag{5.9}$$

$$\hat{H}_0 |\Phi_i\rangle = E_i |\Phi_i\rangle . \tag{5.10}$$

The expression in eq. 5.8 can be simplified if a change of notation is made.

$$\tilde{a}_i(t) = e^{-iE_i t/\hbar} a_i(t). \tag{5.11}$$

The coefficients $a_k(t)$ are computed by a set of differential equations of first order projecting the state $|\Phi_k\rangle$:

$$\frac{da_k(t)}{dt} = -\frac{i}{\hbar} \sum_{i=0} a_i(t) \langle \Phi_k | \hat{V}(t) | \Phi_i \rangle e^{-i(E_i - E_k)t/\hbar}. \tag{5.12}$$

The perturbation $\hat{V}(t)$ represents the action of the light (laser) or the tunnel electron between the tip and the sample on the electrons of the molecule. To describe this fact the amplitude should be known, ε, the time evolution (the function $f(t)$) and the action mode ($\hat{v}$ operator):

$$\hat{V}(t) = \varepsilon f(t) \hat{v}, \tag{5.13}$$

Laser as excitation source. In this case, the classical force $\boldsymbol{F}(\boldsymbol{r},t)$ that will undergo an electron linked to the electric field, $\boldsymbol{E}(\boldsymbol{r},t)$, of the light is:

$$\boldsymbol{F}(\boldsymbol{r},t) = -q\boldsymbol{E}(\boldsymbol{r},t). \tag{5.14}$$

Where q is the electron charge. However, a uniform electric field is polarized with the z axis (direction $\hat{\boldsymbol{e}}_z$), $\boldsymbol{r},t = E_z(t)\hat{\boldsymbol{e}}_z$ and the associated classical potentials is:

$$V(\boldsymbol{r},t) = E_z(t) z. \tag{5.15}$$

$$\frac{da_k(t)}{dt} = -\frac{i}{\hbar} \sum_{i=0} \varepsilon a_i(t) f(t) \langle \Phi_k | \hat{v} | \Phi_i \rangle e^{-i(E_i - E_k)t/\hbar}. \tag{5.16}$$

The perturbations considered in this work are weak, so a development of the coefficients $a_i(t)$ is a Taylor series around $\varepsilon = 0$ can be made:

$$a_i(t) = a_i(t)|_{\varepsilon=0} + \left.\frac{\partial a_i(t)}{\partial \varepsilon}\right|_{\varepsilon=0} + \frac{\varepsilon^2}{2}\left.\frac{\partial a_i(t)}{\partial \varepsilon}\right|_{\varepsilon=0} + \cdots \tag{5.17}$$

The coefficients of the development 5.17 are determined by inserting the Taylor development in the equations 5.16 and identifying the terms in order of magnitude. At order 0:

$$\left.\frac{da_k(t)}{dt}\right|_{\varepsilon=0} = 0. \tag{5.18}$$

The information on this equation implies that the coefficients at order 0 are time independent. In addition, considering the fundamental state and the system in a initial time $t = -\infty$, only the 0 order term is not null and equal to 1:

$$a_{k\_}\varepsilon = 0 = \delta_{k,0}. \tag{5.19}$$

The Taylor development at first order in time of the perturbed system is described by the expression:

$$\frac{d}{dt}\left.\frac{\partial a_k(t)}{\partial \varepsilon}\right|_{\varepsilon=0} = -\frac{i}{\hbar} f(t) e^{i(E_k - E_0)t/\hbar} \langle \Phi_k | \hat{v} | \Phi_0 \rangle . \tag{5.20}$$

At first order all coefficients of the development $(a_k(t))$ are zero except the coefficent $a_0(t)|_{\varepsilon=0} = 1$

$$\left.\frac{\partial a_k(t)}{\partial \varepsilon}\right|_{\varepsilon=0} = -\frac{i}{\hbar} \langle \Phi_k | \hat{v} | \Phi_0 \rangle \int_{-\infty}^{t} \mathrm{d}\tau f(\tau) e^{i(E_k - E_0)\tau/\hbar}. \tag{5.21}$$

The perturbed state of first order in time is given by the expression:

$$|\Psi(t)\rangle = \sum_{i=0} e^{-iE_i t/\hbar} \left(a_i(t)|_{\varepsilon=0} + \varepsilon \left.\frac{\partial a_i(t)}{\partial \varepsilon}\right|_{\varepsilon=0} + \cdots \right) |\Phi_i\rangle \tag{5.22}$$

$$|\Psi(t)\rangle = e^{-iE_0 t/\hbar} |\Phi_0\rangle + \sum_{i=0} e^{-iE_i t/\hbar} \left(\varepsilon \left.\frac{\partial a_i(t)}{\partial \varepsilon}\right|_{\varepsilon=0} + \cdots \right) |\Phi_i\rangle \tag{5.23}$$

$$|\Psi(t)\rangle \approx e^{-iE_0 t/\hbar}\left\{|\Phi_0\rangle - \frac{i}{\hbar}\varepsilon\sum_{i=0} e^{-i(E_i-E_0)t/\hbar}\langle\Phi_i|\,\hat{v}\,|\Phi_0\rangle \int_{-\infty}^{t} \mathrm{d}\tau f(\tau) e^{i(E_i-E_0)\tau/\hbar}|\Phi_i\rangle\right\} \tag{5.24}$$

$$|\Psi(t)\rangle \approx e^{-iE_0 t/\hbar}\left\{|\Phi_0\rangle - \frac{i}{\hbar}\varepsilon\sum_{i=0} \langle\Phi_i|\,\hat{v}\,|\Phi_0\rangle \int_{-\infty}^{t} \mathrm{d}\tau f(\tau) e^{-i(E_i-E_0)(t-\tau)/\hbar}|\Phi_i\rangle\right\} \tag{5.25}$$

The second term of the right side on eq 5.25 gives the variation $|\delta\Phi_0(t)\rangle$ along the time of the unperturbed state $|\Phi_0(t)\rangle$ of the system, and is also defined as:

$$|\delta\Psi_0(t)\rangle = |\Psi(t)\rangle - e^{-iE_0 t/\hbar}|\Phi_0\rangle = -\frac{i}{\hbar}\varepsilon\sum_{i=0}\langle\Phi_i|\,\hat{v}\,|\Phi_0\rangle\,|\Phi_i\rangle\int_{-\infty}^{t}\mathrm{d}\tau f(\tau)e^{-i(E_i-E_0)(t-\tau)/\hbar} \tag{5.26}$$

In order to extend the integral of the equation 5.26 from $-\infty$ to $+\infty$, the Heaviside function ($\theta(t)$) is introduced:

$$\theta(t) = \begin{cases} 0 & if \quad t<0, \\ 1 & if \quad t>0, \end{cases} \tag{5.27}$$

so that

$$|\delta\Psi_0(t)\rangle = -\frac{i}{\hbar}\varepsilon\sum_{i=0}\langle\Phi_i|\,\hat{v}\,|\Phi_0\rangle\,|\Phi_i\rangle \int_{-\infty}^{+\infty}\mathrm{d}\tau f(\tau)\theta(t-\tau)e^{-i(E_i-E_0)(t-\tau)/\hbar} \tag{5.28}$$

The variation of the perturbed state of the system along the time appears as a product of two terms, a spatial term reflecting the coupling between the stationary state $|\Phi_i\rangle$ of the system induced by the perturbation. The

second term is the temporal part which is the temporal convolution of the perturbation by the kernel,

$$g_i(t) = \theta(t) e^{-i(E_i - E_0)t/\hbar} \tag{5.29}$$

Then, it is reduced to a convolution product of,

$$(f * g_i)(t) = \int_{-\infty}^{+\infty} \mathrm{d}\tau g_i(t-\tau) f(\tau) \tag{5.30}$$

The spatial part in equation 5.28 guarantees that only electronic distributions compatible with the nature of the quantum system are accessible. The convolution product acts as a phase matching term between the perturbation and the stationary states of the system. It guarantees that the perturbation provides the energy needed for the excitation.

The convolution theorem stipulate the product of the two functions is equal to the inverse Fourier transform of the product for the Fourier transform of the two functions[209]:

$$\begin{aligned}(f * g_i)(t) = \int_{-\infty}^{+\infty} \mathrm{d}\tau g_i(t-\tau) f(\tau) &= \int_{-\infty}^{\infty} F(\omega) G(\omega) e^{-i\omega t} \mathrm{d}t \\ &= \int_{-\infty}^{\infty} (f * g_i)(\omega) e^{-i\omega t} \mathrm{d}t\end{aligned} \tag{5.31}$$

However, it should be noted that this theorem is only applied if the two functions are summable over the interval $[-\infty, +\infty]$. It is obvious that this condition is satisfied for the temporal part $f(t)$ of the perturbation. On the other hand, in the form explained above, this is not the case with the convolution kernel which is the product of a Heaviside function by a complex exponential. To make the convolution kernel compatible with the conditions of application of the convolution theorem, a multiplication of the convolution kernel by a function $e^{-\eta t}$, η being a positive real number. The convolution kernel therefore tends towards zero when $t \to +\infty$, making the convolution kernel summable.

With these conditions:

$$\begin{aligned} G_i^{(\eta)}(\omega) &= \int_{-\infty}^{+\infty} \mathrm{d}t\theta(t)e^{-i(E_i-E_0)t/\hbar}e^{i\omega t}e^{-\eta t} \\ &= \frac{i}{\omega-\omega_i+i\eta} \end{aligned} \tag{5.32}$$

$$F(\omega) = \int_{-\infty}^{+\infty} \mathrm{d}t f(t)e^{i\omega t} \tag{5.33}$$

$$(f * g_i^{(\eta)})(\omega) = \frac{i}{\omega-\omega_i+i\eta}\int_{-\infty}^{+\infty} \mathrm{d}t f(t)e^{i\omega t} \tag{5.34}$$

$$(f * g_i^{(\eta)})(\omega) = \frac{i}{\omega-\omega_i+i\eta}F(\omega) \tag{5.35}$$

With $\omega_i = (E_i - E_0)/\hbar$.

$$\begin{aligned} |\delta\Psi_0(t)\rangle = -\frac{i}{\hbar}\varepsilon\sum_{i=0}\langle\Phi_i|\,\hat{v}\,|\Phi_0\rangle\,|\Phi_i\rangle \\ \int_{-\infty}^{+\infty}\mathrm{d}\tau f(\tau)\theta(t-\tau)e^{-i\omega_i(t-\tau)} \end{aligned} \tag{5.36}$$

$$|\delta\Psi_0(t)\rangle = -\frac{i}{\hbar}\varepsilon\sum_{i=0}\langle\Phi_i|\,\hat{v}\,|\Phi_0\rangle\,|\Phi_i\rangle\,(f * g_i)(t) \tag{5.37}$$

$$|\delta\Psi_0(\omega)\rangle = -\frac{i}{\hbar}\varepsilon\sum_{i=0}\langle\Phi_i|\,\hat{v}\,|\Phi_0\rangle\,|\Phi_i\rangle\,(f * g_i)(\omega) \tag{5.38}$$

$$|\delta\Psi_0(t)\rangle = \int_{-\infty}^{+\infty}\mathrm{d}\omega\,|\delta\Psi_0(\omega)\rangle\,e^{-i\omega t} \tag{5.39}$$

$$|\delta\Psi_0(t)\rangle = -\frac{i}{\hbar}\varepsilon\sum_{i=0}\langle\Phi_i|\,\hat{v}\,|\Phi_0\rangle\,|\Phi_i\rangle\int_{-\infty}^{+\infty}\mathrm{d}\omega(f * g_i)(\omega)e^{-i\omega t} \tag{5.40}$$

$$|\delta\Psi_0(t)\rangle = \frac{1}{\hbar}\varepsilon \sum_{i=0} \langle\Phi_i|\,\hat{v}\,|\Phi_0\rangle\,|\Phi_i\rangle \int_{-\infty}^{+\infty} \mathrm{d}\omega \frac{F(\omega)}{\omega - \omega_i + i\eta} e^{-i\omega t} \tag{5.41}$$

It should be noted that throughout the process, the wave function associated with the state of the system must be normalized.

$$|\Psi(t)\rangle \approx e^{-iE_0 t/\hbar}\{|\Phi_0\rangle + |\delta\Psi_0(t)\rangle\} \tag{5.42}$$

This implies that the variation of $|\delta\Psi_0(t)\rangle$ must be orthogonal (First order) to the initial state of the system at the beginning of the process, i.e. the stationary state $|\Psi_0\rangle$ ($\langle Psi_0|\,|\delta\Psi_0(t)\rangle = 0$ implying $\langle\Psi_0|\,\hat{v}\,|\Psi_0\rangle = 0$). With these conditions, the sum over the stationary states of the system is carried out over $i > 0$:

$$\begin{aligned} |\delta\Psi_0(t)\rangle &= \frac{1}{\hbar}\varepsilon \sum_{i>0} \langle\Phi_i|\,\hat{v}\,|\Phi_0\rangle\,|\Phi_i\rangle \int_{-\infty}^{+\infty} \mathrm{d}\omega \frac{F(\omega)}{\omega - \omega_i + i\eta} e^{-i\omega t} \\ |\delta\Psi_0(\omega)\rangle &= \frac{1}{\hbar}\varepsilon \sum_{i>0} \langle\Phi_i|\,\hat{v}\,|\Phi_0\rangle\,|\Phi_i\rangle \frac{F(\omega)}{\omega - \omega_i + i\eta} \end{aligned} \tag{5.43}$$

At this point, it is convenient to take a look in the expressions Fig. 5.43 and notices which terms are known and which terms are unknown. The terms $F(\omega)$ are the Fourier components of the temporal part of the perturbation. This data is obtained from a system which is therefore known. It is the same regarding the operator $\hat{v}$ and the amplitude ε of the perturbation.

The states $|\Phi_i\rangle$ and the associated energies (E_i) are given by the unperturbed system. That terms can be described adopting the Kohn-Sham approach [73] which consists in the description of the system by a set of non-interacting particles evolving in a common potential resulting from their distribution in the system. Each of the particles obeys a single-particle Schrödinger equation:

$$H_{KS}\,|\varphi_i\rangle = \varepsilon_i\,|\varphi_i\rangle \tag{5.44}$$

The Hamiltonian described as a isolated pseudo-particle in a $|\varphi_i\rangle$ state with a energy ε_i evolving in a potential $V_{KS}(\boldsymbol{r})$ which is composed by the sum of three terms

$$H_{KS} = -\frac{\hbar^2}{2m}\boldsymbol{\nabla}^2 + v_{KS}(\boldsymbol{r}) \tag{5.45}$$

$$v_{KS}(\boldsymbol{r}) = v_{ext}(\boldsymbol{r}) + \int \frac{\rho(\boldsymbol{r'})}{\mid \boldsymbol{r} - \boldsymbol{r'} \mid} \mathrm{d}\boldsymbol{r'} + \frac{\delta E_{XC}[\rho]}{\delta \rho(\boldsymbol{r})} \tag{5.46}$$

$V_{ext}(\boldsymbol{r})$ is the external potential, for example due to the action of the nuclei over the electrons of the molecule.

$V_H(\boldsymbol{r})$ is the Hartree potential which consider the Coulombian classical interaction between the pseudo-particle and the electronic distribution $\rho(\boldsymbol{r})$ of the electrons in the system:

$$V_H(\boldsymbol{r}) = \int \frac{\rho(\boldsymbol{r'})}{\mid \boldsymbol{r} - \boldsymbol{r'} \mid} \mathrm{d}\boldsymbol{r'} \tag{5.47}$$

$V_{xc}(\boldsymbol{r})$ is the exchange-correlation potential, which consider the N many-body interactions ignored due to the choice of a set of pseudo-particles non-interacting:

$$V_{xc}(\boldsymbol{r}) = \frac{\delta E_{XC}[\rho]}{\delta \rho(\boldsymbol{r})} \tag{5.48}$$

In the context of this approach, the Hamiltonian of the system therefore does not include a term electron-electron interaction:

$$\hat{H}_0 = \sum_{i=1}^{N} \left\{ -\frac{\hbar^2}{2m}\boldsymbol{\nabla}_i^2 + v_{KS}(\boldsymbol{r}_i) \right\} \tag{5.49}$$

Moreover, since electrons are fermions, they must obey the Pauli exclusion principle. The eigenstates of the molecule can then be expressed as Slater's determinant [210]:

$$\Phi(\boldsymbol{r}_1, \boldsymbol{r}_2, \ldots, \boldsymbol{r}_N) = \frac{1}{\sqrt{N!}} SD\left[\varphi_1(\boldsymbol{r}_1)\varphi_2(\boldsymbol{r}_2)\ldots\varphi_N(\boldsymbol{r}_N)\right] \tag{5.50}$$

The total energy of the system, therefore, is the sum of all energies of the occupied states of the pseudo-particles ε_i:

$$E_j = \sum_{i=1}^{N} \varepsilon_i \tag{5.51}$$

The density functional theory and the Hohenber-Kohn theorem [66] shows that the $|\varphi_j\rangle$ states can be determined when the molecule is in the ground state. It means that the $|\Phi_0\rangle$ and the energy E_0 of the unperturbed system are known. The state $|\Phi_0\rangle$ is the lowest energy state and the N mono-electronic occupied states $|\varphi_i\rangle$ lowest in energy.

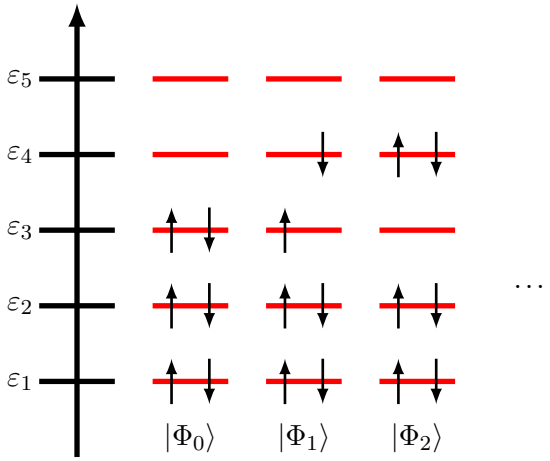

Figure 5.2: Excited states modelization. The ground state energy $|\Phi_0\rangle$ of the unperturbed system is $E_0 = 2(\varepsilon_1 + \varepsilon_2 + \varepsilon_3)$. The state $|\Phi_1\rangle$ is $E_1 = 2(\varepsilon_1 + \varepsilon_2) + \varepsilon_3 + \varepsilon_4$. The state $|\Phi_2\rangle$ is $E_1 = 2(\varepsilon_1 + \varepsilon_2 + \varepsilon_4)$, ...

Also the other states $|\Phi_0\rangle$ which are obtained by swapping one or more of these occupied states with empty states of higher energy (Fig. 5.2). The mono-electronic states $|\varphi_i\rangle$ derived from the same Kohn-Sham Hamiltonian, are orthogonal between them, which means that the stationary states of the molecule $|\Phi_j\rangle$ are also orthogonal to each other.

Whether a laser or the tunnel electron, the $\hat{v}$ operator which describes the perturbation acting on the electrons of the molecule is an operator which acts on only one particle at a time,

$$\hat{v} = \sum_{i=1}^{N} v\boldsymbol{r}_i \tag{5.52}$$

Therefore, the elements $\langle\Psi_i|\,\hat{v}\,|\Phi_0\rangle \neq 0$ in Eq. 5.43 are those for which the states of the molecules $|\Phi_i\rangle$ and $|\Phi_0\rangle$ do not differ only by a single permutation,

$$\langle\Phi_i|\,\hat{v}\,|\Phi_0\rangle = \sum_{j=1}^{N} \langle\Phi_i|\,v(\boldsymbol{r}_j)\,|\Phi_0\rangle \tag{5.53}$$

In order to illustrate this, I consider a system with three electrons. In this case we have:

$$\Phi_0(\boldsymbol{r}_1,\boldsymbol{r}_2,\boldsymbol{r}_3) = \frac{1}{\sqrt{6}}\begin{vmatrix}\varphi_1(\boldsymbol{r}_1) & \varphi_1(\boldsymbol{r}_2) & \varphi_1(\boldsymbol{r}_3)\\ \varphi_2(\boldsymbol{r}_1) & \varphi_2(\boldsymbol{r}_2) & \varphi_2(\boldsymbol{r}_3)\\ \varphi_3(\boldsymbol{r}_1) & \varphi_3(\boldsymbol{r}_2) & \varphi_3(\boldsymbol{r}_3)\end{vmatrix} \tag{5.54}$$

$$\Phi_1(\boldsymbol{r}_1,\boldsymbol{r}_2,\boldsymbol{r}_3) = \frac{1}{\sqrt{6}}\begin{vmatrix}\varphi_1(\boldsymbol{r}_1) & \varphi_1(\boldsymbol{r}_2) & \varphi_1(\boldsymbol{r}_3)\\ \varphi_2(\boldsymbol{r}_1) & \varphi_2(\boldsymbol{r}_2) & \varphi_2(\boldsymbol{r}_3)\\ \varphi_4(\boldsymbol{r}_1) & \varphi_4(\boldsymbol{r}_2) & \varphi_4(\boldsymbol{r}_3)\end{vmatrix} \tag{5.55}$$

$$\Phi_2(\boldsymbol{r}_1,\boldsymbol{r}_2,\boldsymbol{r}_3) = \frac{1}{\sqrt{6}}\begin{vmatrix}\varphi_1(\boldsymbol{r}_1) & \varphi_1(\boldsymbol{r}_2) & \varphi_1(\boldsymbol{r}_3)\\ \varphi_5(\boldsymbol{r}_1) & \varphi_5(\boldsymbol{r}_2) & \varphi_5(\boldsymbol{r}_3)\\ \varphi_4(\boldsymbol{r}_1) & \varphi_4(\boldsymbol{r}_2) & \varphi_4(\boldsymbol{r}_3)\end{vmatrix} \tag{5.56}$$

$$\begin{aligned}\langle\varphi_1|\,\hat{v}\,|\varphi_0\rangle &= \sum_{j=1}^{3} \langle\varphi_1|\,\hat{v}(\boldsymbol{r}_j)\,|\varphi_0\rangle\\ \langle\varphi_1|\,\hat{v}(\boldsymbol{r})\,|\varphi_0\rangle &= \langle\varphi_1|\,\hat{v}(\boldsymbol{r}_1)\,|\varphi_0\rangle + \langle\varphi_1|\,\hat{v}(\boldsymbol{(r}_2)\,|\varphi_0\rangle + \langle\varphi_1|\,\hat{v}(\boldsymbol{r}_3)\,|\varphi_0\rangle\end{aligned} \tag{5.57}$$

After some maths the integral can be expressed as:

$$\langle\Phi_1|\,v(\boldsymbol{r}_1)\,|\Phi_0\rangle = \frac{1}{3}\int d\boldsymbol{r}_1 \Phi_4^* v(\boldsymbol{r}_1)\Phi_3(\boldsymbol{r}_1) \tag{5.58}$$

If instead to consider the state $|\Phi_1\rangle$, we consider the state $|\Phi_2\rangle$, there are two possible permutations of mono-electronic states $|\varphi_2\rangle \to |\varphi_5\rangle$ and $|\varphi_3\rangle \to |\varphi_4\rangle$. Instead of only the permutation $|\varphi_3\rangle \to |\varphi_4\rangle$ for the state $|\Phi_1\rangle$. Then the two non-zero integrals $\int \mathrm{d}\boldsymbol{r}_2\varphi_2^*(\boldsymbol{r}_2)\varphi_2(\boldsymbol{r}_2)$ and $\int \mathrm{d}\boldsymbol{r}_3\varphi_2^*(\boldsymbol{r}_3)\varphi_2(\boldsymbol{r}_3)$ become $\int \mathrm{d}\boldsymbol{r}_2\varphi_2^*(\boldsymbol{r}_5)\varphi_2(\boldsymbol{r}_2)$ and $\int \mathrm{d}\boldsymbol{r}_3\varphi_5^*(\boldsymbol{r}_3)\varphi_2(\boldsymbol{r}_3)$ which are null.

The element $\langle\Phi_1|\, v(\boldsymbol{r}_2)\,|\Phi_0\rangle$ therefore implies an occupied monoelectronic state and a monoelectronic state virtual from the point of view of the molecule in its ground state. Furthermore, due to the indistinguishability of particles, the elements $\langle\Phi_1|\, v(\boldsymbol{r}_2)\,|\Phi_0\rangle$ and $\langle\Phi_1|\, v(\boldsymbol{r}_3)\,|\Phi_0\rangle$ can be defined in the same way as $\langle\Phi_1|\, v(\boldsymbol{r}_1)\,|\Phi_0\rangle = \frac{1}{3}\int d\boldsymbol{r}_1 \Phi_4^* v(\boldsymbol{r}_1)\Phi_3(\boldsymbol{r}_1)$ so that can be written as the double sum on the states of the molecules other than the ground state and on the electrons of the molecule:

$$\sum_j \langle\Phi_j|\,\hat{v}\,|\Phi_0\rangle = \sum_{j>0}\sum_{i=1}^{N} \langle\Phi_i|\, v(\boldsymbol{r}_j)\,|\Phi_0\rangle \tag{5.59}$$

It is possible to write the sum over the occupied and virtual monoelectronic states of the molecule:

$$\begin{aligned} \sum_j \langle\Phi_j|\,\hat{v}\,|\Phi_0\rangle &= \sum_{v\in occ}\sum_{c\in virt}^{N} \langle\Phi_c|\, v(\boldsymbol{r})\,|\Phi_v\rangle \\ \sum_j \langle\Phi_j|\,\hat{v}\,|\Phi_0\rangle &= \sum_{v\in occ}\sum_{c\in virt}^{N} \int d\boldsymbol{r}\Phi_c^*(\boldsymbol{r}) v(\boldsymbol{r})\Phi_v(\boldsymbol{r}) \end{aligned} \tag{5.60}$$

The goal is to stablish a relationship between the perturbation suffered by the molecule (laser or tunnel current) and the variation of the electronic density. The electronic density of the system can be computed from the state of the system and using the density operator, $\hat{n}(\boldsymbol{r})$, defined by Ullrich [211] over all electrons on the system:

$$\hat{n}(\boldsymbol{r}) = \sum_{i=1}^{N} \delta(\boldsymbol{r} - \boldsymbol{r}_i) \tag{5.61}$$

The electron density is an observable, and as such quantum mechanics teaches us that a mean value when the system is in the state $|\Psi(t)\rangle$ is given by the expression:

$$< \hat{n}(\boldsymbol{r}) >= n(\boldsymbol{r}) = \langle\Psi(t)|\,\hat{n}(\boldsymbol{r})\,|\Psi(t)\rangle \tag{5.62}$$

That is the content of eq 5.42 at first order:

$$n(\boldsymbol{r}) \approx \langle \Phi_0 | \hat{n}(\boldsymbol{r}) | \Phi_0 \rangle + \langle \Phi_0 | \hat{n}(\boldsymbol{r}) | \delta\Phi_0(t) \rangle + \langle \delta\Phi_0(t) | \hat{n}(\boldsymbol{r}) | \Phi_0 \rangle \tag{5.63}$$

The term $\langle \Phi_0 | \hat{n}(\boldsymbol{r}) | \Phi_0 \rangle = n_0(\boldsymbol{r})$ represent the electronic density without perturbation, and the difference represents the change in the electronic density of the system due to the action of the perturbation:

$$n(\boldsymbol{r}) - n_0(\boldsymbol{r}) = \langle \Phi_0 | \hat{n}(\boldsymbol{r}) | \delta\Phi_0(t) \rangle + \langle \delta\Phi_0(t) | \hat{n}(\boldsymbol{r}) | \Phi_0 \rangle = \delta n(\boldsymbol{r}) \tag{5.64}$$

$$\begin{aligned} \langle \Phi_0 | \hat{n}(\boldsymbol{r}) | \delta\Phi_0(t) \rangle = \frac{1}{\hbar} \varepsilon \sum_{i>0} \langle \Phi_i | \hat{v} | \Phi_0 \rangle \langle \Phi_0 | \hat{n}(\boldsymbol{r}) | \Phi_i \rangle \\ \int_{-\infty} \mathrm{d}\omega \frac{F(\omega)}{\omega - \omega_i + i\eta} e^{-i\omega t} \end{aligned} \tag{5.65}$$

5.2 Conclusions.

This chapter is the most exploratory in this study. The idea is to model a local perturbation and how it is propagated inside de molecule. The starting point of the hypothesis is to establish a relationship between the changes induced on the electronic density by the perturbation. To this task, the approach was developed under the linear response theory, working in the Fourier space. The theory is in early work but we were able to obtain an expression considering the changes in the electronic density of the system due to the action of a local perturbation. As a perspective, the code under development will teach us if the hypothesis we are postulating is the right direction.

Conclusions and perspectives.

In this study we reported a theoretical study of the optical properties of three different molecules. The thesis is based in three chapters. Chapter three is dedicated to the parametrization of the optical parameters. The aim of this study is to provide a set of reference spectra. For this reason the study of the molecules under a NaCl surface was taken into account. This results reveals the preferential position of the molecules on the surface. H_2Pc and PdPc prefer to be on the top of a sodium atoms and ZnPc on the top of a chlorine atom. Also, the constraint applied to the H_2Pc give us the enough information to justify the tautomerization process observed in the STM experiment. This affirmation could be done thanks to the linear response-time dependent density functional theory, which revealed the variation on the fundamental transitions due to the constraint applied. The study of the fundamental transitions obtained in the photoabsorption spectra behind the real time propagation density functional theory reveals the behaviour of the molecules under the action of a electromagnetic field. Furthermore, the action of a local perturbation allows us to faithfully describe the energy transfer between chromophores. It should be notice that all the simulations carried out in the present work are in good agreement with the experimental results. An error in the range of 100-300 meV were obtained, but considering the theoretical approximations behind the approaches used for this proposal are acceptable.

The last chapter is a purely theoretical chapter. The modelization of the tunnel current is needed, due to the fact that the comparison with the STM experiment was carried out along the study. A better comprehension of the STM-F optical spectra leave us the duty of reproduce faithfully the mechanism from a theoretical point of view. For this reason, the hypothesis postulated in this work is to consider the time variation of the density due to the action of a local perturbation, such a laser or the tunnel current as a wavepacket. The lack of time and the code development, in which we still working, make us to present only the theoretical formulation. The code

is in early development, we are trying to build a time dependent density functional theory from scratch and it takes a lot of effort.

The main perspective of this work is the theory development in early steps. Considering the hypothesis described, a preliminary version of the code will be released to proof them. Also, a more detailed study of the energy transfer should be done. It can be made considering another positions to test the fact of the efficiency on the resonant energy transfer mechanism obtained experimentally. The evolution of the electronic density distribution will give a visual picture of the action of a local perturbation on the molecules. It will allows us to corroborate the propagation of the perturbation on the molecule and also the dipole-dipole interaction from a theoretical point of view.

Appendix A

LR-TDDFT spectra of H_2Pc, ZnPc and PdPc.

A brief description of the fundamental excitation for all molecules was made in chapter three. In this part I give a full description of each spectra. First, consider the H_2Pc molecule. The spectra of this molecule shows 9 main excitations in the range of 2.14-15.487 eV. The excitation of 2.14 eV is the main transition of the molecule between HOMO-LUMO. Q_x band appear at 2.05 eV. The third excitation appears at 3.23 eV and the predominant transition is from the orbital 82 (HOMO-9) to the LUMO. The excitation at 3.56 eV is contained by two main transitions, the first component is from the orbital 82 (HOMO-11) to the orbital 94 (LUMO) with a value of 0.2813 for the Casida eigenvector and the other main component is the transition from the orbital 80 (HOMO-13) to 95 (LUMO+1) with a value of 0.7237 for the Casida eigenvector. This transition is the characteristic B band in phthalocyanines. The sixth excitation is the most intense of the spectra and is a sum of two main transitions, from the orbital 88 (HOMO-5) to 95 (LUMO+1) and a transition between 93 (HOMO) and 94 (LUMO). The excitation at 5.724 consists in a contribution of three main transitions and the transition at 7.56 eV is composed by three transitions. However, the transitions are becoming more and more energetic and depending of the energy applied start to have less probability to happen.

Nevertheless, in the linear response spectra for H_2Pc three more intense excitations are observed at 8.294, 8.845 and 15.487. Also, this excitations do not show a predominant component. In the case of the excitation at 8.294 eV a transition between 63-98 is obtained with a Casida eigenvector value of 0.4868 and this transition can be considered the main one for this band with a contribution of others. The same case is obtained with the other two transitions, where the transitions do not have a main component, conversely,

Molecule	ω (eV)	I(a.u.)	i $\rightarrow$ a	$F^2_{i,ia}$
	2.05		93-95	0.9012
	2.143	37.383	93-94	0.9278
	3.236	37.18	82-94	0.7475
	3.563	49.122	82-94	0.0.2746
			80-95	0.7237
	4.028	164.276	93-94	0.2813
			88-95	0.4829
	5.724	86.068	65-94	0.444
			84-97	0.340
			88-101	0.465
	7.567	89.307	77-102	0.5327
			86-101	0.2350
H_2Pc			86-100	0.2476
	8.294	109.253	74-96	0.2560
			84-96	0.1554
			63-98	0.4868
			82-101	0.3316
			92-101	0.1008
	8.845	46.030	45-95	0.1694
			53-97	0.2860
			57-100	0.3972
			80-103	0.1844
	15.487	150.198	27-97	0.2930
			28-98	0.3160
			31-101	0.3193

Table A.1: Casida analysis of the excitations of H_2Pc.

these excitations are composed by a large contribution of different transitions from orbitals lower in energy to the different virtual orbitals considered in the simulation. As an example the excitation at 15.87 eV, which is the most energetic, the transitions are from orbitals as 27-32 to the unoccupied orbitals as the LUMO+3 to LUMO+10.

The spectra of ZnPc Fig A.2 is dominated by 11 excitations in a range between 2.09-15.47 eV. The excitations are degenerated and the explanation can be done visualizing the table.

Molecule	ω (eV)	I(a.u.)	i $\rightarrow$ a	$F^2_{i,ia}$
ZnPc	2.09	40.94	93-94 / 93-95	0.9182
	3.20	36.7	92-94 / 92-95	0.6685
	4.02	159.48	82-94	0.4519
			82-95	0.5118
	4.70	71.21	83-99 / 83-100	0.5281
	5.73	84.73	64-95 / 65-94	0.5505
			78-97 / 77-97	0.1681
	7.58	92.14	63-96 / 64-96	0.2316
			80-101 / 80-102	0.1189
			77-103 / 78-103	0.4094
			84-103 / 85-103	0.1202
	8.18	99.61	56-94 / 56-95	0.2741
			62-99 / 62-100	0.3922
			90-103 / 89-103	0.2689
	8.78	44.4	63-98 / 64-98	0.1148
			56-99 / 56-100	0.7205
	9.00	42.92	56-100 / 56-99	0.4290
			71-100 / 71-99	0.3078
			80-102 / 80-101	0.2064
	15.25	115.03	31-102	0.2620
			33-103	0.2313
	15.47	146.31	27-100	0.2090
			31-102	0.2516
			33-103	0.2231

Table A.2: Casida analysis of the excitations of ZnPc.

The degeneracy of the perturbations is related to the D_4h symmetry of the molecule that implies the degeneracy of the LUMO. Due to this, two transitions are observed in the main excitation at 2.09 eV, in which two transitions are shown with the same Casida eigenvector value and are from the HOMO (93) to the two orbitals of the LUMO (94 and 95). The excitation that appears at 3.20 eV is a transition from the orbital 92 (HOMO-1) to the two orbitals of the LUMO. The most intense transition of the ZnPc molecule is located at 4.02 eV. This transition is also degenerated but the Casida eigenvector has different value for both transitions from the orbital 82 to the LUMO. It means that the weight of another transitions have more influence in the excitation, in which the the transition from 82 to 94 is the most important.

For the excitation at 4.70 eV the degeneracy still present with two transitions with the same Casida eigenvector for both from the orbital 83 to the degenerated orbital 99 and 100. The excitation at 5.73 eV is composed by a set of 4 transitions being the transition from the orbital 64 to the LUMO the main one with a Casida eigenvector value of 0.5505. The excitation at 7.5 eV is a set of transitions and the couple 77-103 / 78-103 has the highest Casida eigenvector value (0.4094). A degenerated set of three transitions are obtained in the excitation of 8.18 eV with a similar intensity as 7.58. The transitions of this excitation are from the orbital 56 to the LUMO. A transition from the orbital 62 to the degenerated orbital 99-100 with the highest Casida eigenvector value is also observed.

The excitation of 8.78 eV is mainly composed for a transition between the orbital 56 to the degenerated orbital 99-100. A close excitation to this one appears at 9.0 eV composed for a double transition to the degenerated orbital 99-100 from the orbital 56 and 71. For the last two excitation, the degeneracy is broken leading to transitions from non-degenerated to non-degenerated orbitals. The excitation at 15.25 eV is mainly composed by two transitions from orbitals lower in energy as the orbitals 31 and 33 to the orbitals 102 and 103 respectively. The last excitation of the ZnPc is the second most intense of the spectra and is located at 15.47 eV and it is composed by three transitions from the orbitals 27, 31 and 33 to 100, 102 and 103 non-occupied orbitals respectively.

The PdPc is the last to be described and is resumed in Table A.3. The spectra is composed by 15 excitations. The lowest one is the transition from the HOMO to the LUMO and it is located at 2.19 eV.

Molecule	ω (eV)	I(a.u.)	i $\rightarrow$ a	$F^2_{i,ia}$
PdPc	2.16	39.69	97-98 / 97-99	0.9273
	3.17	25.74	88-98 / 88-99	0.8942
	3.61	26.77	84-98 / 84-99	0.7362
	4.35	120.08	96-103	0.6694
	5.23	79.82	81-101 / 82-101	0.5516
			91-104 / 91-105	0.3171
	5.76	73.38	77-100 / 78-100	0.8917
	6.39	93.97	76-102	0.5310
			89-106	0.3791
	6.88	100.52	56-98	0.2608
			64-101	0.4091
	7.63	92.43	65-101	0.2940
			66-104	0.3058
	8.23	83.65	63-104	0.5481
			68-107	0.1617
	8.42	28.96	46-99	0.5306
			47-100	0.3480
	8.90	22.53	64-102 / 64-103	0.2949
			56-104	0.4385
	9.26	18.68	44-100	0.9162
	15.18	100.32	19-99	0.7934
	15.49	82.43	15-98 / 16-99	0.5456

Table A.3: Casida analysis of the excitations of PdPc.

The second excitation at 3.17 eV is mainly the transition from the orbital 88 to the degenerated LUMO with a Casida eigenvector value of 0.8942. The excitation at 3.61 eV also is a transition to the LUMO from the orbital 84. The excitation located at 4.35 eV is the most intense of the spectra and is mainly composed by the transition from the orbital 96 to the unoccupied orbital 103 with a 0.6694 Casida eigenvector value. The next excitation in energy is composed by a double transition from the orbitals 81 and 82 to the orbital 101 and from the occupied orbital 91 to the degenerated

unoccupied 104 and 105. The excitation at 5.76 eV is described by the transition from degenerated occupied orbital 77 and 78 to the orbital 100. The next excitation of the spectra is located at 6.39 eV and is composed by two transition involving four non-degenerated orbitals as the occupied orbitals 76 and 89 to the unoccupied orbitals 102 and 106 respectively. The second most intense excitation is at 6.88 eV composed mainly by two transitions. The transition at 7.63 eV is composed by two main transitions from the degenerated orbital 65/66 to the orbitals 101 and 104 respectively. There is more transition involved on it but the Casida eigenvector values are around 0.05-0.1. That is the reason why such transitions are not taken into account.

The last six excitations to be described can be considered as energetic excitations due to the amount of energy needed to obtain them due to the gap between the orbitals involved in the transitions. The excitation at 8.23 eV is composed by two transitions from the orbitals 63 and 68 to the unoccupied orbitals 104 and 107 respectively. The excitation at 8.42 eV is one of the less intense of the spectra as the transition at 8.90 eV and 9.26 eV. The first one is composed by two main transitions from the orbitals 46 and 47 to the orbitals 99 and 100. The second one is composed by a degenerated transition from the occupied orbital 64 to the degenerated unoccupied orbital 102/103, also there is a transition, with the biggest Casida eigenvector value from the orbital 56 to the orbital 104. The last one is the less intense of the spectra composed mainly by the transition from the orbital 44 to the orbital 100. The last two excitations are the most energetic of the spectra and are located at 15.18 eV and 15.49 eV respectively. The fist of them is the third most intense excitation for the spectra and it is mainly composed by the transition from the occupied orbital 19 to the 99. The last excitation of the spectra is composed by a degenerated transition from the degenerated occupied orbital 15/16 to the same unoccupied orbital as the previous excitation, the unoccupied orbital 99.

The less energetic fundamental transition HOMO-LUMO is obtained in the ZnPc molecule with a value of 2.09 eV with difference of 0.05 eV and 0.1 eV respect to H_2Pc and PdPc respectively. Moreover, the next three excitations around 3.15-4.0 eV are in good agreement between them. However, there is a shift of 0.3 eV for the most intense excitation of all spectra for the PdPc molecule in comparison with the excitation located at 4.02 eV for H_2Pc as well as ZnPc. All the transitions from occupied orbitals reach the LUMO of the different molecules. In the case of H_2Pc the LUMO+1 is also involved in the excitations.

The ZnPc molecule shows a excitation more intense than the other molecules located at 4.70 eV. In the same way the PdPc molecule shows a

excitation at 5.23 eV which is missing on the other spectra. For instance, the excitation at 5.72 eV is present in all spectra. In the PdPc molecule is mainly composed by one transition, although, a combination of transitions is obtained for the other two molecules. A set of two intense excitations are obtained in the PdPc spectra located at 6.39 and 6.88 eV. These excitations also appear in the H_2Pc and ZnPc but with a small intensity making them negligible for the explanation. The difference of intensity in this bands could be explained due to the fact that Pd has a high contribution in the orbitals involved on the excitations. The excitations located in the range of 7.5-8.30 eV show a small shift of 0.1 eV. The main difference is the intensity of the excitations around 8.20 eV being the H_2Pc the most intense followed by the ZnPc and the less intense is the PdPc excitation.

The H_2Pc molecule shows a single band located at 8.84 eV but in the case of ZnPc and PdPc is split in two transitions located at 8.78 and 9.00 eV for ZnPc molecule and 8.90 and 9.26 eV for the PdPc molecule. This band splitting can be considered as an effect due to the metallic atoms in the center of the molecule. Therefore, it can be a consequence of the different symmetry of the molecules of study. The same splitting is obtained in the most energetic excitation of the spectra, a single band is obtained for the H_2Pc molecule at 15.48 eV. For ZnPc the less intense is located at 15.25 eV and the most intense at 15.47 eV. This band splitting has more significance in PdPc molecule where the two bands can be clearly identified. After the description and spectra comparison for all molecules the main conclusion that can be extracted is big influence of the Palladium atom in the electronic structure. This affirmation is done due to the fact of the obtention of three bands which are missed in the other two spectra. Also the small role played by the symmetry is shown in the split of some bands. In general, the linear response behaviour is similar for all molecules of study.

Bibliography

[1] Oppenheimer, J. R. *Physical Review* **1928**, *31*, 66–81.

[2] Fowler, R. H.; Nordheim, L. *Proceedings of the Royal Society of London. Series A, Containing Papers of a Mathematical and Physical Character* **1928**, *119*, 173–181.

[3] Gamow, G. *Zeitschrift for Physik* **1928**, *51*, 204–212.

[4] Rice, O. K. *Physical Review* **1929**, *34*, 1451–1462.

[5] Frenkel, J. *Physical Review* **1930**, *36*, 1604–1618.

[6] Holm, R.; Meissner, W. *Zeitschrift for Physik* **1932**, *74*, 715–735.

[7] Holm, R.; Meissner, W. *Zeitschrift for Physik* **1933**, *86*, 787–791.

[8] Zener, C. *Proceedings of the Royal Society of London. Series A, Containing Papers of a Mathematical and Physical Character* **1934**, *145*, 523–529.

[9] Binnig, G.; Rohrer, H.; Gerber, C.; Weibel, E. *Applied Physics Letters* **1982**, *40*, 178–180.

[10] Becker, R. S.; Golovchenko, J. A.; Swartzentruber, B. S. *Nature* **1987**, *325*, 419–421.

[11] Shedd, G. M.; Russell, P. *Nanotechnology* **1990**, *1*, 67–80.

[12] Foster, J.; Frommer, J. E.; Arnett, P. *Nature* **1988**, *331*, 324–326.

[13] Eigler, D. M.; Schweizer, E. K. *Nature* **1990**, *344*, 524–526.

[14] LYO, I.-W.; AVOURIS, P. *Science* **1991**, *253*, 173–176.

[15] Joachim, C.; Gimzewski, J. K.; Schlittler, R. R.; Chavy, C. *Physical Review Letters* **1995**, *74*, 2102–2105.

[16] Bumm, L. A.; Arnold, J. J.; Cygan, M. T.; Dunbar, T. D.; Burgin, T. P.; Jones, L.; Allara, D. L.; Tour, J. M.; Weiss, P. S. *Science* **1996**, *271*, 1705–1707.

[17] Gomes, K. K.; Mar, W.; Ko, W.; Guinea, F.; Manoharan, H. C. *Nature* **2012**, *483*, 306–310.

[18] Kempkes, S. N.; Slot, M. R.; Freeney, S. E.; Zevenhuizen, S. J. M.; Vanmaekelbergh, D.; Swart, I.; Smith, C. M. *Nature Physics* **2018**, *15*, 127–131.

[19] Xu, B. *Science* **2003**, *301*, 1221–1223.

[20] Poot, M.; Osorio, E.; O'Neill, K.; Thijssen, J. M.; Vanmaekelbergh, D.; van Walree, C. A.; Jenneskens, L. W.; van der Zant, H. S. J. *Nano Letters* **2006**, *6*, 1031–1035.

[21] Schmaus, S.; Bagrets, A.; Nahas, Y.; Yamada, T. K.; Bork, A.; Bowen, M.; Beaurepaire, E.; Evers, F.; Wulfhekel, W. *Nature Nanotechnology* **2011**, *6*, 185–189.

[22] Vazquez, H.; Skouta, R.; Schneebeli, S.; Kamenetska, M.; Breslow, R.; Venkataraman, L.; Hybertsen, M. *Nature Nanotechnology* **2012**, *7*, 663–667.

[23] Verlhac, B.; Bachellier, N.; Garnier, L.; Ormaza, M.; Abufager, P.; Robles, R.; Bocquet, M.-L.; Ternes, M.; Lorente, N.; Limot, L. *Science* **2019**, *366*, 623–627.

[24] Song, H.; Kim, Y.; Jang, Y. H.; Jeong, H.; Reed, M. A.; Lee, T. *Nature* **2009**, *462*, 1039–1043.

[25] Doppagne, B.; Chong, M. C.; Bulou, H.; Boeglin, A.; Scheurer, F.; Schull, G. *Science* **2018**, *361*, 251–255.

[26] Gimzewski, J. K.; Reihl, B.; Coombs, J. H.; Schlittler, R. R. *Zeitschrift fr Physik B Condensed Matter* **1988**, *72*, 497–501.

[27] Gimzewski, J. K.; Sass, J. K.; Schlitter, R. R.; Schott, J. *Europhysics Letters (EPL)* **1989**, *8*, 435–440.

[28] Coombs, J. H.; Gimzewski, J. K.; Reihl, B.; Sass, J. K.; Schlittler, R. R. *Journal of Microscopy* **1988**, *152*, 325–336.

[29] Berndt, R.; Gimzewski, J. K. *Physical Review B* **1993**, *48*, 4746–4754.

[30] Berndt, R.; Gaisch, R.; Gimzewski, J. K.; Reihl, B.; Schlittler, R. R.; Schneider, W. D.; Tschudy, M. *Science* **1993**, *262*, 1425–1427.

[31] Berndt, R.; Gaisch, R.; Schneider, W. D.; Gimzewski, J. K.; Reihl, B.; Schlittler, R. R.; Tschudy, M. *Physical Review Letters* **1995**, *74*, 102–105.

[32] Uehara, Y.; Fujita, T.; Ushioda, S. *Physical Review Letters* **1999**, *83*, 2445–2448.

[33] Downes, A.; Welland, M. E. *Physical Review Letters* **1998**, *81*, 1857–1860.

[34] Hoffmann, G.; Libioulle, L.; Berndt, R. *Physical Review B* **2002**, *65*, DOI: 10.1103/physrevb.65.212107.

[35] Alemani, M.; Peters, M. V.; Hecht, S.; Rieder, K.-H.; Moresco, F.; Grill, L. *Journal of the American Chemical Society* **2006**, *128*, 14446–14447.

[36] Kuang, G.; Zhang, Q.; Lin, T.; Pang, R.; Shi, X.; Xu, H.; Lin, N. *ACS Nano* **2017**, *11*, 6295–6300.

[37] Ormaza, M.; Bachellier, N.; Faraggi, M. N.; Verlhac, B.; Abufager, P.; Ohresser, P.; Joly, L.; Romeo, M.; Scheurer, F.; Bocquet, M.-L.; Lorente, N.; Limot, L. *Nano Letters* **2017**, *17*, 1877–1882.

[38] Yadav, K.; Mahapatra, S.; Halbritter, T.; Heckel, A.; Gopakumar, T. G. *The Journal of Physical Chemistry Letters* **2018**, *9*, 6326–6333.

[39] Qiu, X. H. *Science* **2003**, *299*, 542–546.

[40] Nazin, G. V. *Science* **2003**, *302*, 77–81.

[41] Doppagne, B.; Chong, M. C.; Lorchat, E.; Berciaud, S.; Romeo, M.; Bulou, H.; Boeglin, A.; Scheurer, F.; Schull, G. *Physical Review Letters* **2017**, *118*, DOI: 10.1103/physrevlett.118.127401.

[42] Doppagne, B.; Neuman, T.; Soria-Martinez, R.; López, L. E. P.; Bulou, H.; Romeo, M.; Berciaud, S.; Scheurer, F.; Aizpurua, J.; Schull, G. *Nature Nanotechnology* **2020**, *15*, 207–211.

[43] Phillips, J. C.; Kleinman, L. *Physical Review* **1959**, *116*, 287–294.

[44] Troullier, N.; Martins, J. L. *Physical Review B* **1991**, *43*, 1993–2006.

[45] Rappe, A. M.; Rabe, K. M.; Kaxiras, E.; Joannopoulos, J. D. *Physical Review B* **1990**, *41*, 1227–1230.

[46] Vanderbilt, D. *Physical Review B* **1990**, *41*, 7892–7895.

[47] Blöchl, P. E. *Physical Review B* **1994**, *50*, 17953–17979.

[48] Greengard, L.; Rokhlin, V. *Journal of Computational Physics* **1987**, *73*, 325–348.

[49] Greengard, L. *Computers in Physics* **1990**, *4*, 142.

[50] Davidson, E. R. *Journal of Computational Physics* **1975**, *17*, 87–94.

[51] Pulay, P. *Journal of Computational Chemistry* **1982**, *3*, 556–560.

[52] Kerker, G. P. *Physical Review B* **1981**, *23*, 3082–3084.

[53] Martins, J. L.; Cohen, M. L. *Physical Review B* **1988**, *37*, 6134–6138.

[54] Teter, M. P.; Payne, M. C.; Allan, D. C. *Physical Review B* **1989**, *40*, 12255–12263.

[55] Kresse, G.; Furthmüller, J. *Physical Review B* **1996**, *54*, 11169–11186.

[56] Runge, E.; Gross, E. K. U. *Physical Review Letters* **1984**, *52*, 997–1000.

[57] CASIDA, M. E. In *Recent Advances in Density Functional Methods*; WORLD SCIENTIFIC: 1995, pp 155–192.

[58] Stratmann, R. E.; Scuseria, G. E.; Frisch, M. J. *The Journal of Chemical Physics* **1998**, *109*, 8218–8224.

[59] Petersilka, M.; Gossmann, U. J.; Gross, E. K. U. *Physical Review Letters* **1996**, *76*, 1212–1215.

[60] Adler, S. L. *Physical Review* **1962**, *126*, 413–420.

[61] Yabana, K.; Bertsch, G. F. *International Journal of Quantum Chemistry* **1999**, *75*, 55–66.

[62] Perdew, J. P.; Zunger, A. *Physical Review B* **1981**, *23*, 5048–5079.

[63] Crank, J.; Nicolson, P. *Mathematical Proceedings of the Cambridge Philosophical Society* **1947**, *43*, 50–67.

[64] Schrödinger, E. *Physical Review* **1926**, *28*, 1049–1070.

[65] Born, M.; Oppenheimer, R. *Annalen der Physik* **1927**, *389*, 457–484.

[66] Hohenberg, P.; Kohn, W. *Physical Review* **1964**, *136*, B864–B871.

[67] Coppens, P., *X-Ray Charge Densities and Chemical Bonding (International Union of Crystallography Texts on Crystallography)*; International Union of Crystallography: 1997.

[68] Zuo, J. M.; Spence, J. C. H.; O'Keeffe, M. *Physical Review Letters* **1988**, *61*, 353–356.

[69] Zuo, J. M.; Blaha, P.; Schwarz, K. *Journal of Physics: Condensed Matter* **1997**, *9*, 7541–7561.

[70] Thomas, L. H. *Mathematical Proceedings of the Cambridge Philosophical Society* **1927**, *23*, 542–548.

[71] Fermi, E. *Rend. Accad. Naz. Lincei* **1927**, *6*, 32.

[72] Fermi, E. *Zeitschrift for Physik* **1928**, *48*, 73–79.

[73] Kohn, W.; Sham, L. J. *Physical Review* **1965**, *140*, A1133–A1138.

[74] Perdew, J. P.; Zunger, A. *Physical Review B* **1981**, *23*, 5048–5079.

[75] Perdew, J. P.; Wang, Y. *Physical Review B* **1992**, *45*, 13244–13249.

[76] Becke, A. D. *Physical Review A* **1988**, *38*, 3098–3100.

[77] Lee, C.; Yang, W.; Parr, R. G. *Physical Review B* **1988**, *37*, 785–789.

[78] Perdew, J. P.; Chevary, J. A.; Vosko, S. H.; Jackson, K. A.; Pederson, M. R.; Singh, D. J.; Fiolhais, C. *Physical Review B* **1992**, *46*, 6671–6687.

[79] Perdew, J. P.; Burke, K.; Ernzerhof, M. *Physical Review Letters* **1996**, *77*, 3865–3868.

[80] Perdew, J. P.; Kurth, S.; Zupan, A.; Blaha, P. *Physical Review Letters* **1999**, *82*, 2544–2547.

[81] Tao, J.; Perdew, J. P.; Staroverov, V. N.; Scuseria, G. E. *Physical Review Letters* **2003**, *91*, DOI: 10.1103/physrevlett.91.146401.

[82] Zhao, Y.; Truhlar, D. G. *The Journal of Chemical Physics* **2006**, *125*, 194101.

[83] Becke, A. D. *The Journal of Chemical Physics* **1993**, *98*, 1372–1377.

[84] Kim, K.; Jordan, K. D. *The Journal of Physical Chemistry* **1994**, *98*, 10089–10094.

[85] Stephens, P. J.; Devlin, F. J.; Chabalowski, C. F.; Frisch, M. J. *The Journal of Physical Chemistry* **1994**, *98*, 11623–11627.

[86] Vosko, S. H.; Wilk, L.; Nusair, M. *Canadian Journal of Physics* **1980**, *58*, 1200–1211.

[87] Gross, E.; Kohn, W. In *Density Functional Theory of Many-Fermion Systems*, Löwdin, P.-O., Ed.; Advances in Quantum Chemistry, Vol. 21; Academic Press: 1990, pp 255–291.

[88] Ghosh, S. K.; Dhara, A. K. *Physical Review A* **1988**, *38*, 1149–1158.

[89] Gross, E. K. U.; Dobson, J. F.; Petersilka, M. In *Density Functional Theory II: Relativistic and Time Dependent Extensions*, Nalewajski, R. F., Ed.; Springer Berlin Heidelberg: Berlin, Heidelberg, 1996, pp 81–172.

[90] *Density Functional Theory*; Gross, E. K. U., Dreizler, R. M., Eds.; Springer US: 1995.

[91] Van Leeuwen, R. *Physical Review Letters* **1998**, *80*, 1280–1283.

[92] Van leeuwen, R. *International Journal of Modern Physics B* **2001**, *15*, 1969–2023.

[93] Keldysh, L. V. *Soviet Physics JETP* **1965**, *20*, 1018–1026.

[94] Ando, T. *Zeitschrift for Physik B Condensed Matter and Quanta* **1977**, *26*, 263–272.

[95] Ando, T. *Solid State Communications* **1977**, *21*, 133–136.

[96] Zangwill, A.; Soven, P. *Physical Review A* **1980**, *21*, 1561–1572.

[97] Zangwill, A.; Soven, P. *Physical Review Letters* **1980**, *45*, 204–207.

[98] Yabana, K.; Bertsch, G. F. *Physical Review B* **1996**, *54*, 4484–4487.

[99] Yabana, K.; Bertsch, G. F. *Physical Review A* **1999**, *60*, 1271–1279.

[100] Yabana, K.; Bertsch, G. F. *Physical Review A* **1999**, *60*, 3809–3814.

[101] Braun, A.; Tcherniac, J. *Berichte der deutschen chemischen Gesellschaft* **1907**, *40*, 2709–2714.

[102] Byrne, G. T.; Linstead, R. P.; Lowe, A. R. *Journal of the Chemical Society (Resumed)* **1934**, 1017.

[103] Linstead, R. P.; Lowe, A. R. *Journal of the Chemical Society (Resumed)* **1934**, 1022.

[104] Dent, C. E.; Linstead, R. P. *Journal of the Chemical Society (Resumed)* **1934**, 1027.

[105] Barrett, P. A.; Dent, C. E.; Linstead, R. P. *Journal of the Chemical Society (Resumed)* **1936**, 1719.

[106] Dent, C. E.; Linstead, R. P.; Lowe, A. R. *Journal of the Chemical Society (Resumed)* **1934**, 1033.

[107] Robertson, J. M. *Journal of the Chemical Society (Resumed)* **1935**, 615.

[108] Robertson, J. M. *Journal of the Chemical Society (Resumed)* **1936**, 1195.

[109] Robertson, J. M.; Woodward, I. *Journal of the Chemical Society (Resumed)* **1937**, 219.

[110] Linstead, R. P.; Robertson, J. M. *Journal of the Chemical Society (Resumed)* **1936**, 1736.

[111] Patent, C. L. S. **1949**, *263*, 65S.

[112] Kirin, I.; Moskalev, P.; Ivannikova, N. *Russ. J. Inorg. Chem.* **1965**, *10*, 1065.

[113] Kirin, I.; Moskalev, P.; Ivannikova, N. *Russ. J. Inorg. Chem.* **1970**, *15*, 7.

[114] Cuellar, E. A.; Marks, T. J. *Inorganic Chemistry* **1981**, *20*, 3766–3770.

[115] Geyer, M.; Plenzig, F.; Rauschnabel, J.; Hanack, M.; del Rey, B.; Sastre, A.; Torres, T. *Synthesis* **1996**, *1996*, 1139–1151.

[116] Cian, A. D.; Moussavi, M.; Fischer, J.; Weiss, R. *Inorganic Chemistry* **1985**, *24*, 3162–3167.

[117] Capobianchi, A.; Ercolani, C.; Paoletti, A. M.; Pennesi, G.; Rossi, G.; Chiesi-Villa, A.; Rizzoli, C. *Inorganic Chemistry* **1993**, *32*, 4605–4611.

[118] Wöhrle, D. *Advanced Materials* **1993**, *5*, 942–943.

[119] Sandman, D. J. *Molecular Crystals and Liquid Crystals Science and Technology. Section A. Molecular Crystals and Liquid Crystals* **2000**, *338*, 275–276.

[120] Lever, A. B. P.; Pickens, S. R.; Minor, P. C.; Licoccia, S.; Ramaswamy, B. S.; Magnell, K. *Journal of the American Chemical Society* **1981**, *103*, 6800–6806.

[121] Luck, R. L. *Materials and Manufacturing Processes* **1999**, *14*, 450–451.

[122] Tedesco, A.; Rotta, J.; Lunardi, C. *Current Organic Chemistry* **2003**, *7*, 187–196.

[123] Nunes, S.; Sguilla, F.; Tedesco, A. *Brazilian Journal of Medical and Biological Research* **2004**, *37*, 273–284.

[124] Simioni, A. R.; Rodrigues, M. M. A.; Primo, F. L.; Morais, P. C.; Tedesco, A. C. *Journal of Nanoscience and Nanotechnology* **2011**, *11*, 3604–3608.

[125] Pelisson, M. M.; Delega, A. D.; Beltrame, M.; Simioni, A. R.; Tedesco, A. C. *Photomedicine and Laser Surgery* **2006**, *24*, 581–587.

[126] Rotta, J.; Lunardi, C.; Tedesco, A. *Brazilian Journal of Medical and Biological Research* **2003**, *36*, 587–594.

[127] Huang, A. Y.; Myers, J. T.; Barkauskas, D.; Howell, S. J.; Oleinick, N. L.; McCormick, T. S.; Cooper, K. D.; Baron, E. D.; Lam, M. *Photodiagnosis and Photodynamic Therapy* **2012**, *9*, 225–231.

[128] Kessel, D.; Reiners, J. *Israel Journal of Chemistry* **2012**, *52*, 674–680.

[129] Tedesco, A.; Primo, F.; Beltrame, M. In *Reference Module in Materials Science and Materials Engineering*; Elsevier: 2016.

[130] Yang, H.; Li, R.; Xie, K. In *Nanoporous Materials III, Proceedings of the 3rdInternational Symposium on Nanoporous Materials*; Elsevier: 2002, pp 575–582.

[131] Barker, C.; Zeng, X.; Bettington, S.; Batsanov, A.; Bryce, M.; Beeby, A. *Chemistry - A European Journal* **2007**, *13*, 6710–6717.

[132] LEWIS, P. A. In *Applied Polymer Science: 21st Century*; Elsevier: 2000, pp 493–526.

[133] Gregory, P. In *Comprehensive Coordination Chemistry II*; Elsevier: 2003, pp 549–579.

[134] Waring, D. In *Comprehensive Heterocyclic Chemistry*; Elsevier: 1984, pp 317–346.

[135] De la Torre, G.; Nicolau, M.; Torres, T. In *Supramolecular Photosensitive and Electroactive Materials*; Elsevier: 2001, pp 1–111.

[136] Andrade, X. et al. *Physical Chemistry Chemical Physics* **2015**, *17*, 31371–31396.

[137] Nazareth, J. L. *Wiley Interdisciplinary Reviews: Computational Statistics* **2009**, *1*, 348–353.

[138] Varga, K.; Driscoll, J. A., *Computational Nanoscience*; Cambridge University Press: 2009.

[139] Bitzek, E.; Koskinen, P.; Gähler, F.; Moseler, M.; Gumbsch, P. *Physical Review Letters* **2006**, *97*, DOI: 10.1103/physrevlett.97.170201.

[140] Verlet, L. *Physical Review* **1967**, *159*, 98–103.

[141] Allen, F. H.; Kennard, O.; Watson, D. G.; Brammer, L.; Orpen, A. G.; Taylor, R. *Journal of the Chemical Society, Perkin Transactions 2* **1987**, S1.

[142] Scheidt, W. R.; Dow, W. *Journal of the American Chemical Society* **1977**, *99*, 1101–1104.

[143] Geiss, A.; Vahrenkamp, H. *Inorganic Chemistry* **2000**, *39*, 4029–4036.

[144] Groom, C. R.; Allen, F. H. *Angewandte Chemie International Edition* **2014**, *53*, 662–671.

[145] Takenaka, A.; Sasada, Y.; Yamamoto, K.; Tsuji, J. *Bulletin of the Chemical Society of Japan* **1977**, *50*, 3177–3181.

[146] De Graaf, W.; Harder, S.; Boersma, J.; van Koten, G.; Kanters, J. A. *Journal of Organometallic Chemistry* **1988**, *358*, 545–562.

[147] Uhlmann, C.; Swart, I.; Repp, J. *Nano Letters* **2013**, *13*, 777–780.

[148] Chen, C. J. *Physical Review B* **1990**, *42*, 8841–8857.

[149] Neuman, T.; Esteban, R.; Casanova, D.; Garcıa-Vidal, F. J.; Aizpurua, J. *Nano Letters* **2018**, *18*, 2358–2364.

[150] Jaynes, E.; Cummings, F. *Proceedings of the IEEE* **1963**, *51*, 89–109.

[151] Valiev, M.; Bylaska, E.; Govind, N.; Kowalski, K.; Straatsma, T.; Dam, H. V.; Wang, D.; Nieplocha, J.; Apra, E.; Windus, T.; de Jong, W. *Computer Physics Communications* **2010**, *181*, 1477–1489.

[152] Pivetta, M.; Patthey, F.; Stengel, M.; Baldereschi, A.; Schneider, W.-D. *Physical Review B* **2005**, *72*, DOI: 10.1103/physrevb.72.115404.

[153] Miwa, K.; Imada, H.; Kawahara, S.; Kim, Y. *Physical Review B* **2016**, *93*, DOI: 10.1103/physrevb.93.165419.

[154] Murray, C.; Dozova, N.; McCaffrey, J. G.; Shafizadeh, N.; Chin, W.; Broquier, M.; Crépin, C. *Physical Chemistry Chemical Physics* **2011**, *13*, 17543.

[155] Macfarlane, R.; Völker, S. *Chemical Physics Letters* **1980**, *69*, 151–155.

[156] Bernadotte, S.; Evers, F.; Jacob, C. R. *The Journal of Physical Chemistry C* **2013**, *117*, 1863–1878.

[157] Malola, S.; Lehtovaara, L.; Enkovaara, J.; Häkkinen, H. *ACS Nano* **2013**, *7*, 10263–10270.

[158] Guidez, E. B.; Aikens, C. M. *Nanoscale* **2012**, *4*, 4190.

[159] Baseggio, O.; Fronzoni, G.; Stener, M. *The Journal of Chemical Physics* **2015**, *143*, 024106.

[160] Baseggio, O.; Vetta, M. D.; Fronzoni, G.; Stener, M.; Sementa, L.; Fortunelli, A.; Calzolari, A. *The Journal of Physical Chemistry C* **2016**, *120*, 12773–12782.

[161] Casida, M. E. *Journal of Molecular Structure: THEOCHEM* **2009**, *914*, 3–18.

[162] Bauernschmitt, R.; Ahlrichs, R. *Chemical Physics Letters* **1996**, *256*, 454–464.

[163] Walker, B.; Saitta, A. M.; Gebauer, R.; Baroni, S. *Physical Review Letters* **2006**, *96*, DOI: 10.1103/physrevlett.96.113001.

[164] Andrade, X.; Botti, S.; Marques, M. A. L.; Rubio, A. *The Journal of Chemical Physics* **2007**, *126*, 184106.

[165] Ferguson, J.; Reeves, L. W.; Schneider, W. G. *Canadian Journal of Chemistry* **1957**, *35*, 1117–1136.

[166] Theisen, R. F.; Huang, L.; Fleetham, T.; Adams, J. B.; Li, J. *The Journal of Chemical Physics* **2015**, *142*, 094310.

[167] Edwards, L.; Gouterman, M. *Journal of Molecular Spectroscopy* **1970**, *33*, 292–310.

[168] McHugh, A. J.; Gouterman, M.; Weiss, C. *Theoretica Chimica Acta* **1972**, *24*, 346–370.

[169] Cott, T. C. V.; Rose, J. L.; Misener, G. C.; Williamson, B. E.; Schrimpf, A. E.; Boyle, M. E.; Schatz, P. N. *The Journal of Physical Chemistry* **1989**, *93*, 2999–3011.

[170] Savolainen, J.; van der Linden, D.; Dijkhuizen, N.; Herek, J. L. *Journal of Photochemistry and Photobiology A: Chemistry* **2008**, *196*, 99–105.

[171] Plows, F. L.; Jones, A. C. *Journal of Molecular Spectroscopy* **1999**, *194*, 163–170.

[172] Fischer, S. A.; Cramer, C. J.; Govind, N. *The Journal of Physical Chemistry Letters* **2016**, *7*, 1387–1391.

[173] Guo, M.; He, R.; Dai, Y.; Shen, W.; Li, M.; Zhu, C.; Lin, S. H. *The Journal of Chemical Physics* **2012**, *136*, 144313.

[174] Yabana, K.; Nakatsukasa, T.; Iwata, J.-I.; Bertsch, G. F. *physica status solidi (b)* **2006**, *243*, 1121–1138.

[175] Sander, T.; Kresse, G. *The Journal of Chemical Physics* **2017**, *146*, 064110.

[176] Hohenleutner, M.; Langer, F.; Schubert, O.; Knorr, M.; Huttner, U.; Koch, S. W.; Kira, M.; Huber, R. *Nature* **2015**, *523*, 572–575.

[177] Repisky, M.; Konecny, L.; Kadek, M.; Komorovsky, S.; Malkin, O. L.; Malkin, V. G.; Ruud, K. *Journal of Chemical Theory and Computation* **2015**, *11*, 980–991.

[178] Bruner, A.; LaMaster, D.; Lopata, K. *Journal of Chemical Theory and Computation* **2016**, *12*, 3741–3750.

[179] Hofmann, D.; Kümmel, S. *The Journal of Chemical Physics* **2012**, *137*, 064117.

[180] Townsend, E.; Bryant, G. W. *Nano Letters* **2011**, *12*, 429–434.

[181] Townsend, E.; Bryant, G. W. *Journal of Optics* **2014**, *16*, 114022.

[182] Ma, J.; Wang, Z.; Wang, L.-W. *Nature Communications* **2015**, *6*, DOI: 10.1038/ncomms10107.

[183] Li, X.; Smith, S. M.; Markevitch, A. N.; Romanov, D. A.; Levis, R. J.; Schlegel, H. B. *Phys. Chem. Chem. Phys.* **2005**, *7*, 233–239.

[184] Bende, A.; Toşa, V. *Physical Chemistry Chemical Physics* **2015**, *17*, 5861–5871.

[185] Provorse, M. R.; Habenicht, B. F.; Isborn, C. M. *Journal of Chemical Theory and Computation* **2015**, *11*, 4791–4802.

[186] Li, Y.; Ullrich, C. *Chemical Physics* **2011**, *391*, 157–163.

[187] Li, Y.; Ullrich, C. A. *Journal of Chemical Theory and Computation* **2015**, *11*, 5838–5852.

[188] Kolesov, G.; Grånäs, O.; Hoyt, R.; Vinichenko, D.; Kaxiras, E. *Journal of Chemical Theory and Computation* **2015**, *12*, 466–476.

[189] Hochbruck, M.; Lubich, C. *SIAM Journal on Numerical Analysis* **1997**, *34*, 1911–1925.

[190] O'Rourke, C.; Bowler, D. R. *The Journal of Chemical Physics* **2015**, *143*, 102801.

[191] Moler, C.; Loan, C. V. *SIAM Review* **2003**, *45*, 3–49.

[192] Castro, A.; Marques, M. A. L.; Rubio, A. *The Journal of Chemical Physics* **2004**, *121*, 3425–3433.

[193] Williams-Young, D.; Goings, J. J.; Li, X. *Journal of Chemical Theory and Computation* **2016**, *12*, 5333–5338.

[194] Hamam, K. J.; Alomari, M. I. *Applied Nanoscience* **2017**, *7*, 261–268.

[195] Timoumi, A.; Turkestani, M. K. A.; Alamri, S. N.; Alamri, H.; Ouerfelli, J.; Jamoussi, B. *Journal of Materials Science: Materials in Electronics* **2017**, *28*, 7480–7488.

[196] Andrews, D.; Curutchet, C.; Scholes, G. *Laser & Photonics Reviews* **2010**, *5*, 114–123.

[197] Engel, G. S.; Calhoun, T. R.; Read, E. L.; Ahn, T.-K.; Mančal, T.; Cheng, Y.-C.; Blankenship, R. E.; Fleming, G. R. *Nature* **2007**, *446*, 782–786.

[198] Christensson, N.; Kauffmann, H. F.; Pullerits, T.; Mančal, T. *The Journal of Physical Chemistry B* **2012**, *116*, 7449–7454.

[199] Pullerits, T.; Hess, S.; Herek, J. L.; Sundström, V. *The Journal of Physical Chemistry B* **1997**, *101*, 10560–10567.

[200] Scholes, G. D.; Fleming, G. R. *The Journal of Physical Chemistry B* **2000**, *104*, 1854–1868.

[201] Chong, M. C.; Reecht, G.; Bulou, H.; Boeglin, A.; Scheurer, F.; Mathevet, F.; Schull, G. *Physical Review Letters* **2016**, *116*, DOI: 10.1103/physrevlett.116.036802.

[202] Zhang, Y.; Luo, Y.; Zhang, Y.; Yu, Y.-J.; Kuang, Y.-M.; Zhang, L.; Meng, Q.-S.; Luo, Y.; Yang, J.-L.; Dong, Z.-C.; Hou, J. G. *Nature* **2016**, *531*, 623–627.

[203] Imada, H.; Miwa, K.; Imai-Imada, M.; Kawahara, S.; Kimura, K.; Kim, Y. *Nature* **2016**, *538*, 364–367.

[204] Hinze, G.; Métivier, R.; Nolde, F.; Müllen, K.; Basché, T. *The Journal of Chemical Physics* **2008**, *128*, 124516.

[205] Roy, R.; Hohng, S.; Ha, T. *Nature Methods* **2008**, *5*, 507–516.

[206] Chen, C. J. In *Introduction to Scanning Tunneling Microscopy*; Oxford University Press: 2007, pp 331–348.

[207] Bernath, P., *Spectra of Atoms and Molecules*; Oxford University Press, New York: 1995.

[208] Kubo, R. *Journal of the Physical Society of Japan* **1957**, *12*, 570–586.

[209] Arfken, G.; Weber, H. J., *Mathematical Methods for Physicists*; Academic, San Diego, CA 6th Ed.: 2005.

[210] Kohanoff, J., *Electronic Structure Calculations for Solids and Molecules: Theory and Computational Methods*; Cambridge University Press, Cambridge, UK, 2006.

[211] Ulrich, C., *Time-Dependent Density functional theory: Concepts and applications*; Oxford Graduate Texts; Oxford University Press, New York: 2012.

Rubén Soria Martínez

Modeling of local excitation processes in molecular nanojunctions

Résumé

L'une des application les plus remarquables de l'effet tunnel est le microscope à effet tunnel (STM) qui permet de cartographier spatialement et énergétiquement la répartition des électrons à la surface des matériaux avec une résolution nanométrique. Des avancées récentes permettent en outre d'exploiter la pointe du STM comme une source d'excitation locale des matériaux.

Le travail de thèse présenté dans ce manuscrit vise à décrire et à modéliser les phénomènes impliqués lors d'une telle excitation. Nous présentons une modélisation des spectres d'absorption de molécule de phthalocyanine reposant sur des surfaces dans le cadre de la théorie de la fonctionnelle de densité dépendante du temps (TD-DFT). Nous montrons que l'analyse spectroscopique des transitions entre l'état fondamental et les états excités de la molécule permet de caractériser son état de contrainte.

Nous mettons également en évidence une variété de spectres d'excitation selon la localisation de l'excitation de la molécule. Nous discutons la possibilité d'exploiter ce phénomène pour caractériser les transports d'énergie inter-moléculaire.

Mots-clés : spectre d'excitation, STM, TD-DFT, phthalocyanine

Résumé en anglais

One of the most remarkable applications of the tunnel effect is the Scanning Tunneling Microscope (STM), allowing to get the spatially and energetically map distribution of electrons on the surface of materials with nanometric resolution. Recent advances make it possible to exploit the tip of the STM as a source of local excitation of materials.

The work presented in this manuscript aims to describe and model the phenomena involved in such excitation process. We present a modeling of the absorption spectra of phthalocyanine molecules lying on surfaces within the framework of the time-dependent density functional theory (TD-DFT). We show that spectroscopic analysis of the transitions between the ground state and the excited states of the molecule allows to characterize the stress inside the molecule.

We also highlight a variety of excitation spectra depending on the location of the excitation of the molecule. We discuss the possibility of exploiting this phenomenon to characterize inter-molecular energy transport.

Keywords : excitation spectra, STM, TD-DFT, phthalocyanine